

**CHARACTERIZATION OF AEROSOL PARTICLES AT LOW TEMPERATURES IN A BATH GAS
COOLING CELL AND BESSEL BEAM OPTICAL TRAP**

by

Merrill Isenor

BSc, Cape Breton University, 2007

MSc, University of Manitoba, 2010

A THESIS SUBMITTED IN PARTIAL FULFILLMENT OF
THE REQUIREMENTS FOR THE DEGREE OF

DOCTOR OF PHILOSOPHY

in

THE FACULTY OF GRADUATE AND POSTDOCTORAL STUDIES

(Chemistry)

THE UNIVERSITY OF BRITISH COLUMBIA

(Vancouver)

February, 2015

© Merrill Isenor, 2015

Abstract

This thesis focuses on low temperature studies of ensembles of aerosol particles formed in a bath gas cooling cell (78 K) and of single aerosol particles trapped in a counter-propagating Bessel beam optical trap (228-260 K). Ensemble particle measurements provide average data for all particles within the ensemble. These measurements are directly applicable to the study of clouds and aerosols in the atmospheres of a variety of planets and moons. Conversely, single particle measurements offer insight into behaviours which may be dependent on a particular particle property, such as particle size. Single particle data complement that obtained from ensemble measurements.

The ensemble particle studies are performed with rapid-scan Fourier-transform infrared (FTIR) spectroscopy to determine intrinsic particle properties (size, shape, composition, and architecture) and the temporal evolution of these properties. The assignments based on infrared spectra are supported by calculations using the vibrational exciton model. In this work, several mixed water aerosol ensembles are considered: carbon dioxide-water, ammonia-water, and acetylene-water aerosols. Each of these aerosol systems have relevance to the atmospheres of planets and moons (e.g. Mars, Saturn, Jupiter, Enceladus). All three mixtures are studied under similar pressure and temperature conditions. While ammonia-water and acetylene-water are found to form molecularly mixed particles, there is no evidence of molecular mixing in carbon dioxide-water aerosol particles. Measurements are performed at low temperatures to study the freezing and evaporation of single aerosol particles. Our new experimental setup consists of a counter-propagating Bessel beam optical trap for trapping of micron and submicron sized particles down to temperatures of 223 K. The measurements in this thesis present the first freezing studies of single particles into the

submicron size range. A series of freezing studies for supercooled liquid hexadecane, dodecane, and water particles are presented here, along with preliminary evaporation experiments for supercooled hexadecane droplets. These measurements show that the low temperature trap is an attractive device to study freezing and evaporation of single particles.

Preface

Chapter 3 was published as:

M. Isenor, R. Escribano, T. C. Preston, and R. Signorell, *Icarus*, 2013, **223**, 591–601.

The research program was designed by R. Signorell. The experiments, DDA and vibrational exciton calculations, and data analysis were performed by M. Isenor. DFT calculations were performed by R. Escribano with assistance from T.C. Preston. The manuscript was prepared by M. Isenor with minor modifications by R. Signorell.

Chapter 4 has been accepted for publication:

M. Isenor and R. Signorell, *Mol. Phys.*, 2014, DOI: 10.1080/00268976.2014.981232.

The research program was designed by R. Signorell. The experiments, calculations, and data analysis were performed by M. Isenor. The manuscript was prepared by M. Isenor with minor modifications by R. Signorell.

Chapter 5 contains some work that has been previously published. A version of Section 5.3 has been published as:

J.W. Lu, M. Isenor, E. Chasovskikh, D. Stapfer, and R. Signorell, *Rev. Sci. Instrum.*, 2014, **85**, 095107.

The research program was designed by R. Signorell. The low temperature experiment was designed and built by J.W. Lu, E. Chasovskikh, D. Stapfer, and R. Signorell. Experiments and data analysis were performed by M. Isenor and J.W. Lu. The manuscript was prepared by J.W. Lu, M. Isenor and R. Signorell.

The remaining research in Chapter 5 (Section 5.2) was designed by R. Signorell. The experiments and data analysis were performed by M. Isenor with assistance from J.W. Lu.

Table of Contents

Abstract	ii
Preface	iv
Table of Contents	v
List of Tables	xii
List of Figures	xiii
List of Symbols	xxvi
List of Abbreviations	xxx
Acknowledgements	xxxii
Chapter 1: Introduction	1
1.1 Importance of aerosol studies	1
1.2 Particle ensemble and single particle measurements	4
1.3 Thesis overview.....	8
Chapter 2: Methods	11
2.1 Infrared measurements of aerosol particle ensembles	11

2.1.1	Cooling cell and infrared spectrometer	11
2.1.2	Sample preparation.....	15
2.2	Simulation of aerosol particle infrared spectra.....	16
2.2.1	Vibrational exciton calculations.....	16
2.2.2	Discrete dipole approximation	18
2.3	Optical trapping of single aerosol particles	23
2.3.1	Trapping at room temperatures	23
2.3.1.1	Optical trap.....	23
2.3.1.2	Trapping cell.....	24
2.3.1.3	Particle generation.....	26
2.3.2	Trapping at low temperatures.....	26
2.3.2.1	Low temperature trapping cell	26
2.3.2.2	Vacuum chamber	30
2.3.3	Particle characterization	31
2.3.3.1	Data acquisition.....	31
2.3.3.2	Data analysis.....	32

2.3.3.3	Errors and limitations.....	36
Chapter 3: Predicting the infrared band profiles for CO₂ cloud particles on Mars.....		38
3.1	Introduction.....	38
3.2	Methods.....	41
3.2.1	Discrete dipole approximation.....	41
3.2.2	Vibrational exciton model.....	41
3.2.3	Mixed H ₂ O/CO ₂ unit cells.....	42
3.2.4	Experimental.....	43
3.3	Overview spectra of aerosols spectra in the mid-IR.....	44
3.4	Predicted spectra for different particle types.....	46
3.4.1	Effect of particle size.....	46
3.4.1.1	Pure CO ₂ particles.....	46
3.4.1.2	H ₂ O-CO ₂ core-shell particles.....	49
3.4.2	Effect of particle shape.....	51
3.4.2.1	Pure CO ₂ particles.....	51
3.4.2.2	H ₂ O-CO ₂ core-shell particles.....	53

3.4.3	Effect of mixing.....	55
3.4.4	Effect of architecture.....	57
3.4.5	Effect of core material	59
3.5	Experimental attempts to form core-shell particles	60
3.5.1	The N ₂ O-CO ₂ system.....	61
3.5.2	The H ₂ O-CO ₂ system.....	62
3.6	Summary	64

Chapter 4: Infrared spectroscopy of solid mixed ammonia-water and acetylene-water

aerosol particles	67	
4.1	Introduction	67
4.2	Methods	70
4.2.1	Experiments	70
4.2.2	Vibrational exciton calculations.....	71
4.3	Results	72
4.3.1	Ammonia-water aerosol particles.....	73
4.3.1.1	Overview of aerosol particle IR spectra	73
4.3.1.2	Comparison to thin film spectra.....	77

4.3.1.3	Comparison to other particle spectra	79
4.3.1.4	Comparison to calculated spectra.....	80
4.3.1.5	Mixing in core-shell ammonia-water particles.....	81
4.3.2	Acetylene-water aerosol particles.....	88
4.3.2.1	Overview of aerosol particle IR spectra	88
4.3.2.2	Comparison to thin film spectra.....	92
4.3.2.3	Comparison to calculated spectra.....	93
4.3.2.4	Mixing in core-shell acetylene-water particles	94
4.4	Summary	96
Chapter 5: Optical trapping of single aerosol particles		98
5.1	Introduction	98
5.1.1	Optical trapping: trapping forces.....	98
5.1.2	Bessel beams.....	101
5.1.3	Counter-propagating Bessel beam optical trap	107
5.1.4	Advantages of the counter-propagating Bessel beam optical trap.....	110
5.2	Optical trapping at room temperature	113

5.2.1	Motivation	113
5.2.2	Sample preparation and experimental conditions	115
5.2.3	Data analysis.....	115
5.2.3.1	Sizing of aqueous particles	115
5.2.3.2	Growth factor calculations.....	117
5.2.3.3	Half-time calculations	118
5.2.4	Concentrative refractive index parameterizations	120
5.2.4.1	Glucose	120
5.2.4.2	Fructose	123
5.2.4.3	Raffinose.....	126
5.2.5	RH-induced effects on single aqueous carbohydrate particles	129
5.2.5.1	Glucose	129
5.2.5.2	Fructose	141
5.2.5.3	Raffinose.....	144
5.2.6	Conclusions for room temperature trapping experiments.....	148
5.3	Optical trapping at low temperatures.....	149

5.3.1	Motivation	149
5.3.2	Data analysis.....	150
5.3.3	Freezing studies.....	151
5.3.3.1	Hexadecane.....	151
5.3.3.2	Dodecane.....	162
5.3.3.3	Water	165
5.3.4	Particle evaporation.....	166
5.3.5	Conclusions for low temperature trapping experiments	171
5.4	Summary of single particle measurements.....	172
Chapter 6: Conclusions		175
6.1	Summary	175
6.2	Outlook.....	177
References.....		179

List of Tables

Table 4.1: Infrared band assignments for pure and mixed NH_3 and H_2O aerosol particles formed in the cooling cell (see Figure 4.1).....	75
Table 4.2: Infrared band assignments for pure and mixed C_2H_2 and H_2O aerosol particles formed in the cooling cell (see Figure 4.7).....	91

List of Figures

Figure 1.1: Bar chart for radiative forcing (RF) of important anthropogenic compounds, agents, and mechanisms for the period 1750-2011. Well mixed greenhouse gases (WMGHG) refers to those gases with atmospheric lifetimes that are long enough to allow for near homogenous mixing in the troposphere. Reprinted from IPCC Fifth Assessment Report: Climate Change 2013, The Physical Science Basis. ⁴	3
Figure 1.2: An example of the freezing kinetics for an ensemble of ethane aerosol particles analyzed with IR spectroscopy. The evolution in the region of the CH ₃ rocking vibration is shown for a) supercooled liquid droplets, b) an intermediate state consisting of a mixture of spectra of supercooled liquid particles and crystalline particles, and c) crystalline particles. Black squares represent the fraction of unfrozen particles (P_u) in the ensemble as a function of time. Reprinted from <i>Annu. Rev. Phys. Chem.</i> , 2009, 60 , 127-146. Copyright 2009 by Annual Reviews.....	6
Figure 2.1: Illustration of the bath gas cooling cell.....	12
Figure 2.2: The different valve pulse sample injection methods for the cooling cell. a) Injection of a one-component sample or a premixed sample through a single valve, b) simultaneous injection of two separate gas samples, and c) sequential injection of two separate gas samples with a delay time between the start of each valve opening pulse, Δt	13
Figure 2.3: Illustration of an example of the passage of infrared light through White optics. ⁹⁸ The numbers in the illustration outline the path that the light takes within the optics (eight passes).....	15
Figure 2.4: a) An example particle (cube) and b) the approximation of the particle by an array of 1000 point dipoles.	19

Figure 2.5: Illustration of the optical trapping setup at room temperature (CW = continuous wave, RH = relative humidity, PBS = polarization beam splitter).....24

Figure 2.6: The room temperature optical trapping cell. The dimensions of the cell are 1.5 cm × 1.5 cm × 1.5 cm.....25

Figure 2.7: Illustration of the optical trapping setup for the low temperature trapping experiments (CW = continuous wave, PBS = polarization beam splitter).....27

Figure 2.8: The copper cell and vacuum chamber used in the low temperature trapping experiments. The vacuum chamber has been lightened to facilitate viewing of the copper cell. The copper cell is placed on an insulating platform and attached to a breadboard. The vacuum chamber is also attached to the breadboard, which is secured to the laser table. Reprinted with permission from *Review of Scientific Instruments*, 2014, **85**, 095107. Copyright 2014, AIP Publishing LLC.....28

Figure 2.9: A cross-sectional view of the copper trapping cell. Reprinted with permission from *Review of Scientific Instruments*, 2014, **85**, 095107. Copyright 2014, AIP Publishing LLC.....29

Figure 2.10: a) Image of the perpendicularly polarized light scattered from a liquid hexadecane particle, b) the errors associated with Mie fits over the input size range (radius, r) of 1700-2500 nm, c) comparison between the experimental phase function and the best fit according to Mie theory ($r = 2116$ nm), and d) comparison between the experimental phase function and the second best fit according to Mie theory ($r = 2057$ nm).....33

Figure 2.11: Mie scattering polar plot for 532 nm light scattered by a hypothetical particle with $r = 1.4$ μm and $n = 1.445$. The scattering intensities are plotted on a logarithmic scale with respect to the scattering angle, θ_{sc}34

Figure 2.12: a) Scattering phase functions (perpendicularly polarized 532 nm light) calculated for hypothetical particles with $n = 1.445$ over the same angular range as for data collected in the current work. The particles range in size from $r = 100$ nm to $r = 400$ nm. The phase functions were scaled to the same maximum and the ordinates are the scattering intensities in arbitrary units.

b) Scattering phase functions calculated for 400 nm particles with different values for n . The phase functions are plotted on the same scale, in arbitrary units.37

Figure 3.1: Experimental IR extinction spectra of aerosol particles generated in our bath gas cooling cell (78 K). Overview spectra are provided for a) pure CO₂ aerosols, b) pure H₂O aerosols, and c) mixed CO₂/H₂O aerosols.....45

Figure 3.2: Calculated IR extinction spectra for pure CO₂ particles of different size. All particles are truncated cubes and the particle size (as indicated by the arrow) is given for each spectrum. The ordinates are the extinctions in arbitrary units.....47

Figure 3.3: Calculated IR extinction spectra for pure CO₂ particles with sizes above 1000 nm (see Figure 3.2 for sizes below 1000 nm). Note the different wavenumber scale compared to Figure 3.2. The spectra show pronounced scattering features such as the sloping baseline and the dispersion shape of the absorption peaks. The ordinates are the extinctions in arbitrary units.....48

Figure 3.4: Calculated IR extinction spectra for 100 nm and 1000 nm (particle width, as indicated by arrow) H₂O-CO₂ core-shell truncated cubic particles. The thickness of the CO₂ shell (s) is indicated for each spectrum along with the number ratio of H₂O to CO₂ in each particle (ratio of the number of molecules calculated from the volume of the core and shell and the densities of H₂O and CO₂). The ordinates are the extinctions in arbitrary units..... 50

Figure 3.5: Calculated IR extinction spectra for pure CO₂ particles of different shape, each with approximately the same volume. Particle dimensions are all within 10-100 nm. Spectra were calculate for a) a sphere, b) a bipyramid, c) a truncated cube, d) a cube, and e-h) elongated particles with axis ratios e) 1 × 1 × 1.5, f) 1 × 1 × 2, g) 1 × 1 × 4, and h) 1 × 1 × 7. The ordinates are the extinctions in arbitrary units.....53

Figure 3.6: Calculated IR extinction spectra for 100 nm truncated cubic and bipyramidal H₂O-CO₂ core-shell particles. The thickness of the CO₂ shell is indicated for each spectrum along with the ratio of H₂O to CO₂ (as described for Figure 3.4). The ordinates are the extinctions in arbitrary units.....54

Figure 3.7: Calculated IR extinction spectra for 7.8 nm H₂O-CO₂ core-shell particles with a mixed interface layer. Spectra on the left have a very thin pure CO₂ shell, while the thickness of the CO₂ shell for spectra on the right is similar to the thickness of the mixed interface layer. The H₂O:CO₂ mixing ratio of the intermediate layer is indicated for each spectrum. The ordinates are the extinctions in arbitrary units.....57

Figure 3.8: Calculated IR extinction spectra for different CO₂ architectures. a) Pure CO₂, b) complete CO₂ shell surrounding a H₂O core, and c) partial engulfing of H₂O by CO₂ (average for an ensemble of CO₂ patch shapes and sizes). The ordinates are the extinctions in arbitrary units.....58

Figure 3.9: Calculated IR extinction spectra for core-shell particles (bipyramids) consisting of a CO₂ shell and different core materials: a) H₂O core, b) FeO core, and c) Fe₃O₄ core. For all particles, the ratio of the core width to the shell thickness is 1:0.13. The ordinates are the extinctions in arbitrary units.....60

Figure 3.10: Experimental IR extinction spectra of a) pure CO₂ aerosols, b) molecularly mixed N₂O/CO₂ aerosols formed by simultaneous injection of CO₂ and N₂O, and c) N₂O-CO₂ core-shell particles formed by sequential injection of N₂O followed by CO₂. Calculated spectrum for d) N₂O-CO₂ core-shell particle (same N₂O:CO₂ ratio as in panel (c)). The calculated spectrum was convoluted with an 8 cm⁻¹ Voigt profile.62

Figure 3.11: Experimental IR extinction spectra of a) pure CO₂ aerosols, b) simultaneous injection of CO₂ and H₂O, and c) sequential injection of H₂O followed by CO₂. We think that particles with an H₂O core that is partially engulfed by CO₂ patches of various shapes and sizes provide a reasonable explanation for the both the simultaneous and sequential injections.64

Figure 4.1: Overview infrared aerosol particle spectra for a) pure NH₃, b) pure H₂O, c) a sum spectrum (addition of spectrum (a) and spectrum (b)) d) particles formed after injection of a premixed H₂O/NH₃ sample, and e) particles formed after simultaneous injection of NH₃ and H₂O samples. Insets in (c), (d), and (e) show an expanded view of the ammonia ν₂ band and the dangling-OH stretch region. The ratio of H₂O:NH₃ is approximately 2:1 in (c), (d), and (e).74

Figure 4.2: Comparison of NH₃-H₂O aerosol particle spectra to thin film spectra. a & b) Molecularly mixed H₂O-NH₃ particles formed at 78 K after simultaneous injection of the sample gases, c) H₂O-NH₃ thin film measurement at 90 K, d) monohydrate thin film measurement at 95 K, e) hemihydrate thin film measurement at 95K. Insets show an expanded view of the umbrella region. Thin film measurements were taken from the work of Hudson et al.^{150,176} All spectra are scaled to the same maximum for ease of comparison.78

Figure 4.3: Comparison of experimental spectra and calculated spectra for a) pure crystalline ammonia aerosol particles and b) mixed amorphous ammonia-water aerosol particles.81

Figure 4.4: Temporal evolution in the region of the ammonia umbrella mode after sequential injection of the sample gases. The injection orders were: a) H₂O then NH₃ and b) NH₃ then H₂O. All other injection conditions remained the same for both experiments. The ratio of H₂O:NH₃ is approximately 2:1. Examples of fitting results used to create the plots in Figure 4.6 are shown for the spectra recorded at 101 s (grey traces).84

Figure 4.5: As for Figure 4.4, but with a ratio of H₂O:NH₃ of approximately 5:1.85

Figure 4.6: Fraction of molecularly mixed NH₃ as a function of time for particles formed by sequential injection. The ratio of H₂O:NH₃ is approximately a) 2:1 and b) 5:1. The corresponding spectra are shown in Figure 4.4 and Figure 4.5, respectively. Sample fits are depicted in Figure 4.4 (grey traces) for spectra recorded 101 s after injection.87

Figure 4.7: Overview infrared aerosol particle spectra for a) pure C₂H₂, b) pure H₂O, c) a sum spectrum (addition of spectrum (a) and spectrum (b)), and d) particles formed after simultaneous injection of C₂H₂ and H₂O samples. The ratio H₂O:C₂H₂ is approximately 3:1 in (c) and (d). e) An H₂O-C₂H₂ (5:1) thin film measurement at 20 K. The thin film spectrum was taken from the work of Hudson et al.^{164,176} Insets show an expanded view of the region for the C₂H₂ ν_2 mode and the dangling-OH stretch region.90

Figure 4.8: Comparison of experimental spectra and calculated spectra for a) pure polycrystalline acetylene particles and b) mixed amorphous acetylene-water aerosol particles. The calculated spectra were taken from the work of Preston et al.²¹ For the experimental acetylene-water spectrum, we subtracted a pure water spectrum to remove the major contributions from the broad water libration band.....94

Figure 4.9: Temporal evolution of spectra in the region of the C_2H_2 ν_5 mode after sequential injection of the sample gases (H_2O then C_2H_2). The ratio of $H_2O:C_2H_2$ is approximately 3:1.....96

Figure 5.1: Ray optics diagrams for a) the lateral gradient force, b) the axial gradient force, and c) the scattering force involved in optical trapping.99

Figure 5.2: a) A cross-sectional view of a zeroth-order Bessel beam created using an axicon and b) a simulated image showing a close up view of the Bessel beam core and several rings to illustrate the core radius, r_0 102

Figure 5.3: The formation of a Bessel beam from an incident Gaussian beam using an axicon illustrated as a) a ray tracing diagram and b) plane waves. 103

Figure 5.4: a) The longitudinal wavevector, kz , and b) radial wavevector, kr , for a Bessel beam described in terms of plane waves propagating along a cone. 104

Figure 5.5: Diagram showing the opening angle, γ , and apex angle, τ , of an axicon..... 105

Figure 5.6: A Bessel beam illustrated as plane waves that encounters an obstacle. The Bessel beam reforms at a distance z_{min} after the obstacle..... 107

Figure 5.7: Reformation of the Bessel beam in the trapping cell after initial formation using an axicon. Note that this illustration does not show the second (counter-propagating) Bessel beam. 109

Figure 5.8: Five particles simultaneously trapped in a CPBB optical trap, demonstrating optical binding. 109

Figure 5.9: A first-order exponential decay according to Equation (5.16)..... 119

Figure 5.10: Refractive index data as a function of the mass fraction of solute (MFS) for aqueous glucose solutions. The concentrative data were taken from the CRC Handbook of Chemistry and Physics.²¹⁷ The crystalline glucose RI value was taken from the work of Cao et al.²¹⁸ 120

Figure 5.11: Concentration as a function of the mass fraction of solute (MFS) for aqueous glucose solutions. The concentrative data were taken from the CRC Handbook of Chemistry and Physics.²¹⁷ 122

Figure 5.12: Density as a function of mass fraction of solute (MFS) for aqueous glucose solutions. The concentrative data were taken from the CRC Handbook of Chemistry and Physics.²¹⁷ 123

Figure 5.13: Water activity as a function of mass fraction of solute (MFS) for aqueous fructose solutions. The concentrative data were taken from the work of Correa et al.,²²⁰ Lerici et al.,²²¹ and Gharsallaoui et al.²²² 123

Figure 5.14: Concentration as a function of the mass fraction of solute (MFS) for aqueous fructose solutions. The concentrative data were taken from the CRC Handbook of Chemistry and Physics.²¹⁷ 125

Figure 5.15: Density as a function of mass fraction of solute (MFS) for aqueous fructose solutions. The concentrative data were taken from the CRC Handbook of Chemistry and Physics.²¹⁷ 125

Figure 5.16: Refractive index data as a function of the mass fraction of solute (MFS) for aqueous raffinose solutions. The concentrative data were taken from the work of Lienhard et al.²²³ 127

Figure 5.17: Concentration as a function of the mass fraction of solute (MFS) for aqueous raffinose solutions. The concentrative data were taken from Lienhard et al.²²³ 128

Figure 5.18: Density as a function of mass fraction of solute (MFS) for aqueous raffinose solutions. The concentrative data were taken from the work of Lienhard et al.²²³ 129

Figure 5.19: Light scattering data for a glucose particle during one experiment where RH was decreased from 70% to 0% (in steps of 10%). a) The scattering image, b) experimental phase function and best Mie fit, and c) error for the possible sizes for the glucose particle at RH 70%. d) The scattering image, e) experimental phase function and best Mie fit, and c) error for the possible sizes for the same glucose particle at RH 0%. 132

Figure 5.20: a) The decrease of particle radius and change in RH with respect to time for a glucose particle with initial size $r = 949$ nm. The particle was equilibrated at RH 70% for 2 hours. Note, due to a computer error, RH data was not recorded for the change to RH 0%. b) The experimental and theoretical growth factors for the particle in panel (a). c & d) The calculated half-times for the change in particle radius with respect to RH (c) and the response of each probe to the change in RH (d) for the data in panel (a). 134

Figure 5.21: a) The decrease of particle radius and change in RH with respect to time for a glucose particle with initial size $r = 1937$ nm. The particle was equilibrated at RH 70% for 2 hours. b) The experimental and theoretical growth factors for the particle in panel (a). c & d) The calculated half-times for the change in particle radius with respect to RH (c) and the response of each probe to the change in RH (d) for the data in panel (a). 135

Figure 5.22: Experimental (GF_{BB}) and theoretical (GF_{TH}) diameter growth factors for aqueous NaCl particles as a function of RH. Uncertainty for the RH values is $\pm 3.5\%$ and uncertainty in the values of GF_{BB} is one standard deviation of the average of 50 data points taken at a certain RH (note the latter is of similar magnitude to the symbol size and thus difficult to see). The theoretical hygroscopic growth curve has been derived from the Clegg parameterization²²⁶ and the Clegg and Wexler solution density.²²⁷ Reproduced from *Phys. Chem. Chem. Phys.*, 2014, **16**, 9819–9830 with permission of the PCCP Owner Societies. <http://dx.doi.org/10.1039/C3CP54233E>..... 137

Figure 5.23: a) The decrease of particle radius and change in RH with respect to time for a fructose particle with initial size $r = 2994$ nm. The particle was equilibrated at RH 70% for 2 hours. b) The experimental and theoretical growth factors for the particle in panel (a). c & d) The calculated half-times for the change in particle radius with respect to RH (c) and the response of each probe to the change in RH (d) for the data in panel (a). Note, the particle had moved off of camera after the RH change to 10%. As a result, there are no calculated values for the GF_{dia} at RH 10% or for $t_{1/2}(r)$ for the change from 20% to 10%..... 143

Figure 5.24: Light scattering data for a raffinose particle during one experiment where RH was decreased from 70% to 20% (in steps of 10%). a) The scattering image, b) phase function and Mie fit, and c) error for the possible sizes for the glucose particle at RH 60%. d) The scattering image, e) phase function and Mie fit, and c) error for the possible sizes for the same glucose particle at RH 20%..... 145

Figure 5.25: a) The change of particle radius and change in RH with respect to time for a raffinose particle. Note, the phase functions for this particle did not begin to be recorded until RH 60%. The particle equilibrated at RH 70% for 2 hours, but the initial particle radius at this RH is not known.

b) The experimental and theoretical growth factors for the particle in panel (a). c & d) The calculated half-times for the change in particle radius with respect to RH (c) and the response of each probe to the change in RH (d) for the data in panel (a). 146

Figure 5.26: Image of the scattering phase functions for two supercooled liquid hexadecane droplets that were simultaneously trapped in the low temperature cell at 287.4 K. 153

Figure 5.27: Image of the scattering phase functions for two hexadecane particles simultaneously trapped at 287.5 K in the CPBB optical trap. The particle on the left is frozen, while the particle on the right is a supercooled liquid droplet. Reprinted with permission from *Review of Scientific Instruments*, 2014, **85**, 095107. Copyright 2014, AIP Publishing LLC..... 154

Figure 5.28: Homogeneous freezing times for supercooled hexadecane particles ($r = 800\text{-}5500$ nm) between 286-288 K. Reprinted with permission from *Review of Scientific Instruments*, 2014, **85**, 095107. Copyright 2014, AIP Publishing LLC. 155

Figure 5.29: A large ($r = 5042$ nm) supercooled hexadecane particle at 287.5 K a) before and b) after freezing. A small ($r = 924$ nm) supercooled hexadecane particle at 286.9 K c) before and d) after freezing. Reprinted with permission from *Review of Scientific Instruments*, 2014, **85**, 095107. Copyright 2014, AIP Publishing LLC..... 157

Figure 5.30: The integrated scattering intensity with respect to time for the particles in Figure 5.29. a) The scattering intensity for the large particle (panels (a) and (b) in Figure 5.29) and b) the scattering intensity for the small particle (panels (c) and (d) in Figure 5.29). Note, the large ($r = 5042$ nm) particle was lost from the trap shortly after freezing, thus there are not very many intensity points on the plot in panel (a) after the time of freezing..... 157

Figure 5.31: Individual frames (sequentially from frame 1-8) from a video of a stable supercooled hexadecane particle (frames 1-3) that homogeneously freezes (frame 4), becomes unstable (frames 5-6), and then falls from the trapping position in frame 7. The video was recorded at a rate of approximately 18 frames per second, and each frame was recorded 0.054 s apart..... 159

Figure 5.32: Individual frames (sequentially from frame 1-8) from a video of a stable supercooled hexadecane particle (frames 1-3) that freezes by contact (collision) with a second hexadecane particle. The arrows in frames 3 & 4 point toward the second particle. The frozen particle becomes unstable and is lost from the trapping position in frames 6-7. The video was recorded at a rate of approximately 19 frames per second, and each frame was recorded 0.052 s apart..... 160

Figure 5.33: A cycled hexadecane particle. a) Melting of the frozen particle (note the particle moved off camera between these two frames) and b) subsequent freezing of the same particle (two adjacent frames from the video)..... 161

Figure 5.34: Plot of the freezing and melting times for one hexadecane particle that was cycled between the solid and liquid state. The plot indicates the particle size at the time of each phase change. Note, the particle could not be sized for the freezing event which occurred at $t = 3658$ s due to corruption of the video file that was recorded at that time..... 162

Figure 5.35: A dodecane particle ($r = 4180$ nm) before a) and after b) homogeneous freezing at 252.6 K. c) The integrated scattering intensity for this particle is plotted with respect to time. Reprinted with permission from *Review of Scientific Instruments*, 2014, **85**, 095107. Copyright 2014, AIP Publishing LLC..... 164

Figure 5.36: Plot of the freezing and melting times for one dodecane particle that was cycled between the solid and liquid state. The plot indicates the particle size at the time of each phase change. 165

Figure 5.37: Sizes for five hexadecane particles plotted with respect to time. Particles were trapped at 287.5 K. Each particle is represented by a different shape/colour data point. 168

Figure 5.38: Data for hexadecane evaporation experiments plotted as squared particle radius as a function of time. The data points (colour and shape) correspond to those for the particles in Figure 5.37..... 170

List of Symbols

a_{eff}	Effective radius
a_w	Water activity
b	Bessel beam order
B	Cauchy coefficient
c	Speed of light
C	Cauchy coefficient
C_{abs}	Absorbance cross section
C_{ext}	Extinction cross section
C_{scat}	Scattering cross section
d	Particle diameter
d_s	Interdipole spacing
D	Error difference
D_{drop}	Diffusion coefficient in a spherical droplet
D_v	Vapour diffusion coefficient
$\mathbf{E}_{ext,j}$	Instantaneous electric field
$\mathbf{E}_{inc,j}$	Incident electric field
F_{grad}	Gradient force
F_{scat}	Scattering force

GF_{dia}	Diameter growth factor
GF_{mass}	Mass growth factor
\hat{H}	Vibrational Hamiltonian
\hat{H}_0	Vibrational Hamiltonian for uncoupled molecules
\hat{H}_{DD}	Vibrational Hamiltonian of the pairwise dipole-dipole couplings
\hat{H}_{DID}	Vibrational Hamiltonian of the pairwise dipole-induced dipole couplings
J_b	Bessel function
J_s	Surface freezing rate constant
J_v	Volume freezing rate constant
\vec{k}	Wavevector
\vec{k}_r	Radial wavevector
\vec{k}_z	Longitudinal wavevector
k_0	Wavevector in vacuo
k_t	Rate constant
m	Mixed layer thickness
M	Molecular weight
\bar{n}	Real part of the complex refractive index
n^*	Complex refractive index
N	Number of point dipoles

N_{RI}	Ratio of the refractive index of the particle to the refractive index of the medium
p	Vapour pressure
P	Probability a droplet is unfrozen
\mathbf{P}_j	Instantaneous polarization
Q_{ext}	Extinction efficiency
r	Radius
r_0	Bessel beam core radius
r_{obs}	Obstacle radius
R	Gas constant
R_{ij}	Intermolecular distance
RH_g	Glass transition relative humidity
s	Shell thickness
S	Particle surface area
S_e	Function introduced in Equation (5.35)
t	Time
$t_{1/2}$	Half-time
T	Temperature
T_g	Glass transition temperature
V	Volume
w_0	Gaussian beam diameter

z_{max}	Bessel beam propagation distance
z_{min}	Bessel beam core reformation distance
Z_r	Rayleigh range
α	Polarizability tensor
γ	Axicon opening angle
δ_{ij}	Kronecker's delta
ϵ	Complex dielectric function
ϵ'	Real part of the complex dielectric function
ϵ''	Imaginary part of the complex dielectric function
η	Dynamic viscosity
θ	Cone opening angle
θ_{sc}	Scattering angle
κ	Imaginary part of the complex refractive index
λ	Wavelength
μ_i	Dipole moment vector
ν	Normal vibrational mode
ρ	Density
τ	Axicon apex angle
ω	Frequency

List of Abbreviations

C_2H_2	Acetylene
CO_2	Carbon Dioxide
CPBB	Counter-Propagating Bessel Beam
CW	Continuous Wave
D_2O	Deuterium
DDA	Discrete Dipole Approximation
DFT	Density Functional Theory
EDB	Electrodynamic Balance
FeO	Iron (II) Oxide
Fe_3O_4	Magnetite
FTIR	Fourier Transform Infrared
GF	Growth Factor
H_2O	Water
He	Helium
IPCC	Intergovernmental Panel on Climate Change
IR	Infrared
MFS	Mass Fraction of Solute
N_2	Nitrogen

N ₂ O	Nitrous Oxide
NaCl	Sodium Chloride
NH ₃	Ammonia
PBS	Polarizing Beam Splitter
PC	Personal Computer
QBB	Quadruple Bessel Beam
RI	Refractive Index
RF	Radiative Forcing
RH	Relative Humidity
SOA	Secondary Organic Aerosol

Acknowledgements

I would first like to thank my supervisor, Prof. Ruth Signorell, for her guidance and support during my time in her group. I am grateful for the opportunity to visit the group at ETH Zürich to complete the low temperature single particle measurements for my thesis. I am thankful to the staff members at ETH Zürich who helped to organize my visit to the university, especially Frau Ruth Schüpbach for finding accommodations for me during my stay.

I would like to thank all the members of the Signorell group for their assistance and friendship over the past few years, with special thanks to the following people: Dr. Kerry Knox, for many helpful and interesting discussions on a variety of topics, assistance with experiments, and for being very, very generous with her time; Dr. Jessica Lu for assistance with experiments and data analysis, many Skype conversations, and for providing extremely helpful feedback on drafts of my thesis; Dr. Kathrin Lang for help with experiments; Drs. Thomas Preston and George Firanescu for help with calculations; and Anita Restivo for assistance with experiments, data analysis, and other random tasks.

I would like to acknowledge technical assistance from the mechanical and electrical shops at both UBC and ETH.

Many thanks to Prof. Keng Chou for providing me with a work space at UBC during the latter part of my studies.

Finally, I would like to thank my family and friends for their continuous encouragement. I would especially like to thank my boyfriend, Graeme, for his constant support.

Chapter 1: Introduction

This thesis focuses on the characterization of aerosol particles at low temperatures with the goal to study aerosol particles under conditions that mimic those in different planetary and lunar atmospheres. Both ensemble particle measurements (in a bath gas cooling cell) and single particle measurements (in a Bessel beam optical trap) will be presented. These two types of experiments provide complementary information about aerosol particles. This chapter discusses the motivation for studying aerosol particles and contrasts the ensemble and single particle techniques.

1.1 Importance of aerosol studies

Aerosols are a dispersion of liquid droplets or solid particles in a gaseous medium. They are prevalent in the Earth's atmosphere as well as in the atmospheres of many planets and moons in our solar system. In order to understand their effects in these atmospheres, a detailed understanding of their physical, chemical, and optical properties is required. Laboratory measurements of aerosol particles can provide information about these properties as well as help to predict the types of particles that may be present in various atmospheres.

Aerosols play a role in the radiative balance of the Earth. They are similarly also important in the atmospheres of many planets and moons in our solar system. Aerosol effects fall into two main categories: direct and indirect.¹ The direct effect includes the scattering and absorption of light by

aerosols. Both scattering and absorption are controlled by intrinsic particle properties (e.g. size, shape, composition, architecture).^{2,3} The indirect effect of aerosol particles relates to their ability to act as cloud condensation nuclei, affecting the size and number concentration of cloud particles as well as the lifetime of clouds. The size (diameter, d) of atmospheric aerosol particles spans several orders of magnitude. Nucleation mode aerosol particles are those with $d < 0.1 \mu\text{m}$, particles in the size range $0.1 \mu\text{m} < d < 2.5 \mu\text{m}$ are termed accumulation mode particles, and coarse mode aerosol particles are defined as those with $d > 2.5 \mu\text{m}$.¹

There are still many uncertainties that remain in the study of atmospheric aerosol particles. The graph in Figure 1.1 illustrates just one example of why a better understanding of aerosol particles is required. Figure 1.1 shows the radiative forcing (RF) of the Earth's climate taken from the most recent report by the Intergovernmental Panel on Climate Change (IPCC).⁴ (In the IPCC report, the RF is defined as "the net change in the energy balance of the Earth system due to some imposed perturbation."⁴) One of the striking features of this graph is the size of the error bars associated with aerosol-radiation interactions and aerosol-cloud interactions. The error associated with aerosol effects is related to a lack of knowledge concerning the abundances and properties of aerosol particles, as well as their variation with respect to time and space. The uncertainty in the aerosol effects is a major contributor to the net anthropogenic RF uncertainty. Similar issues concerning aerosol particles also limit our knowledge of processes in other planetary and lunar atmospheres. This makes it clear that a better understanding of aerosol properties (physical, chemical, and optical) is required to begin to lower the magnitude of the error associated with aerosol effects. The study of aerosol particles at low temperatures in the laboratory can lead to a better general understanding of their physical properties. This knowledge can in turn be applied to atmospheric studies to better quantify aerosol impacts.

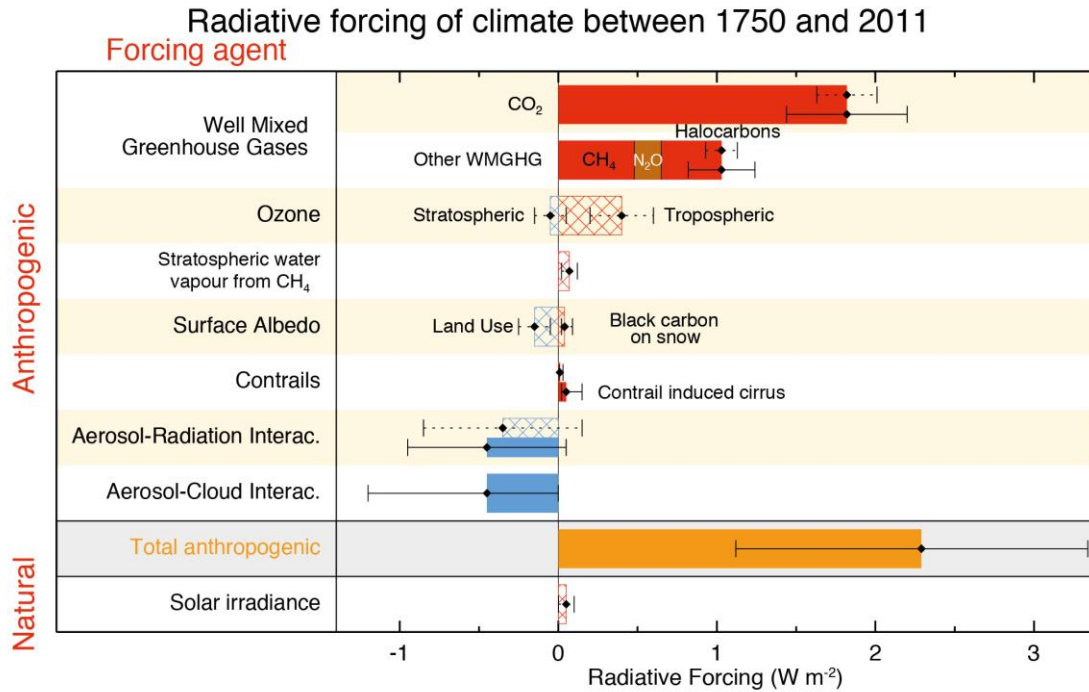


Figure 1.1: Bar chart for radiative forcing (RF) of important anthropogenic compounds, agents, and mechanisms for the period 1750-2011. Well mixed greenhouse gases (WMGHG) refers to those gases with atmospheric lifetimes that are long enough to allow for near homogenous mixing in the troposphere. Reprinted from IPCC Fifth Assessment Report: Climate Change 2013, The Physical Science Basis.⁴

This thesis focuses on the study of aerosol particles at low temperatures ($T = 78-287 \text{ K}$). Such studies can provide information about particle phase transitions as well as the shape, structure, and architecture of particles in the solid phase. The low temperature studies are relevant to atmospheric conditions. The atmospheres of other planets and moons are often studied by remote sensing methods or by instruments on orbiters. Proper interpretation of the aerosol data requires an understanding of the types of particles that may be present in these atmospheres. The aerosol ensembles in different atmospheres (e.g. clouds) are likely composed of particles of different sizes

and with different morphologies, architectures, and compositions. It is difficult to directly analyze each of these properties, which leads to the major limitations in our current understanding of aerosols.^{5,6} For example, particle size affects particle lifetimes in the atmosphere. Both ensemble particle measurements and single particle measurements in the laboratory can be used to gain an understanding of aerosol particle properties as well as temporal changes that may occur under specified conditions.

1.2 Particle ensemble and single particle measurements

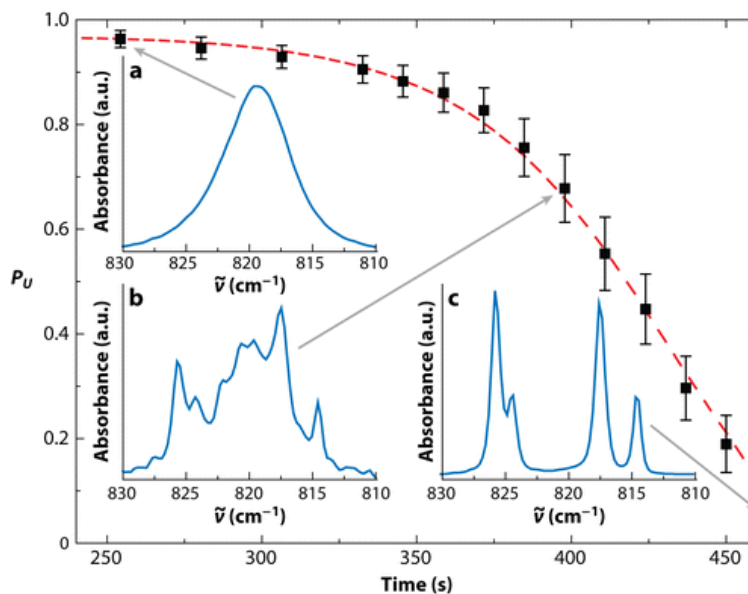
In this section, the example of freezing of supercooled liquid aerosol droplets will be used to illustrate how ensemble particle measurements and single particle measurements complement one another. Both types of experiments are required to gain a complete understanding of aerosol properties and each can provide different information about particles. In this work, single particle experiments refer to studies of unsupported single particles where there is no contact between the particle and any surfaces. Different single particle techniques will be discussed and compared in Chapter 5 (Section 5.1.4).

Freezing of supercooled liquid aerosol particles is initiated by a process known as nucleation.⁷ Classical nucleation theory describes the rate by which a critically-sized cluster (nucleus) of the new phase (in this case, the solid phase) is formed.¹ The rate for formation of the nucleus can be quite slow, but once formed, freezing proceeds very rapidly. Nucleation processes can be described as being homogeneous or heterogeneous. Homogeneous freezing refers to the freezing of a homogeneous liquid aerosol particle initiated solely within the particle (i.e. without any external stimulus) while heterogeneous freezing refers to the freezing of a droplet under an external

stimulus, such as a collision between two particles (contact freezing) or the freezing due to the presence of another solid particle immersed in the liquid droplet (immersion freezing).⁸

In an ensemble of aerosol particles, the properties of the individual particles will typically vary, i.e. there will be a certain distribution of particle sizes and possibly particle shapes within the ensemble. Depending on the composition of the ensemble (pure vs. mixed), there may also be variation in the particle architecture and extent of mixing within the ensemble. As a result, ensemble measurements give information about the average properties of the entire system. Aerosol ensemble measurements are useful to mimic an atmospheric environment (e.g. temperature and pressure conditions) and can be used, for example, to study the possible influence of trace atmospheric components on the freezing rates of aerosol particles.⁸ Aerosols present in the atmosphere are typically distributions of different particles, meaning that ensemble measurements in the laboratory can provide valuable information on the average properties of atmospheric aerosols.

Figure 1.2 shows an example of IR measurements for freezing in an ensemble of ethane particles reprinted from the work of Sigurbjörnsson et al.³ The IR spectra contain information about the average state for all particles in the ensemble and this information can be used to study the freezing kinetics for the ethane particles in terms of the fraction of unfrozen particles with respect to time. Within the aerosol ensemble, individual particles will freeze at different times. As the measurement progresses, the appearance of the CH₃ rocking band gradually changes from being broad and unstructured for the supercooled liquid droplets (panel (a)) to the structured profile for the crystalline particles (panel (c)). Intermediate spectra (e.g. panel (b)) can be analyzed to determine the fraction of unfrozen particles and this data can then be fit to study the kinetics of the freezing process for the ensemble.



 Sigurbjörnsson ÓF, et al. 2009.
Annu. Rev. Phys. Chem. 60:127–46

Figure 1.2: An example of the freezing kinetics for an ensemble of ethane aerosol particles analyzed with IR spectroscopy. The evolution in the region of the CH₃ rocking vibration is shown for a) supercooled liquid droplets, b) an intermediate state consisting of a mixture of spectra of supercooled liquid particles and crystalline particles, and c) crystalline particles. Black squares represent the fraction of unfrozen particles (P_u) in the ensemble as a function of time. Reprinted from *Annu. Rev. Phys. Chem.*, 2009, **60**, 127-146. Copyright 2009 by Annual Reviews.

As mentioned above, aerosol ensembles are complex systems. For an ensemble of particles, it may be difficult to study homogenous freezing rates since there may be contributions from heterogeneous freezing due to collisions between the particles. These contributions are difficult to quantify. Furthermore, it is very difficult to accurately determine the size distribution of a droplet ensemble. Uncertainties in the size distribution can make it hard to determine accurate freezing rate constants. In contrast, the study of single particles can be used to probe a more detailed relationship between particle properties and particle behaviour. For example, single particle

measurements can be used to determine freezing rates for particles for which the conditions are well specified (e.g. well known size determined from light scattering). The mechanism of the freezing process is also better known in single particle studies compared with ensemble measurements. The freezing process would also be known to be either homogeneous or heterogeneous. However, particle freezing is a statistical event. A large number of single particles are needed to gain sufficient data for the derivation of particle freezing rates from single particle measurements. Conversely, the study of freezing of a particle ensemble provides a freezing rate that already encompasses the number of particles required for statistical purposes. There are also limitations to the size of particles that can be studied using suspended single particle techniques. The lower limit of particles that can be confined within an optical trap is on the order of a few hundred nanometers in radius (with the use of a Bessel beam optical trap). As a result, studies for particles ranging in size from approximately 1-100 nm must still rely on measurements of particle ensembles.⁹

It is clear that both ensemble and single particle measurements are useful to gain a better understanding of aerosol particle properties. The choice between ensemble or single particle measurements depends upon the exact aerosol behaviour that is of interest. In many cases, it would be beneficial to study aerosol particles using both ensemble and single particle techniques to gain a complete picture of their behaviour. One goal of the present thesis was to set up a low temperature single particle trapping cell that allows us to perform studies complementary to the ensemble investigations in the existing bath gas cooling cell. The low temperature single particle trap is operational and first test measurements have been performed. Suggestions for future complementary investigations with the trap and the cooling cell are discussed in Chapter 6.

1.3 Thesis overview

This thesis focuses on the study of the physical properties of aerosol particles at low temperatures.

This work contains experiments for both aerosol particle ensembles and single aerosol particles.

Simulations of particle infrared (IR) spectra are performed for comparison to ensemble spectra and the single particle measurements required a new trapping cell to be designed, built, and tested.

IR spectroscopy is a useful tool to study aerosol particle ensembles in situ, as it can provide information about both the molecular composition of particles and intrinsic particle properties, such as size, shape, and architecture.^{3,10,11} However, there is only a limited amount of knowledge concerning aerosol particle properties at low temperatures. Much of this knowledge has come from previous research within the Signorell group.^{3,8-37} Similar mid-IR studies of aerosol particles at low temperatures were also provided by the work of Miller,³⁸⁻⁴⁷ Gough,⁴⁸⁻⁵² Ewing,^{53,54} Devlin,⁵⁵⁻⁶⁹ and Bauerecker.⁷⁰⁻⁷⁷ Previous work from within the Signorell group has clarified that the relationship between the IR spectra of aerosol particles and intrinsic particle properties is due to vibrational exciton couplings^{3,10-21,78,79} (refer also to Section 2.2.1).

Chapter 3 and Chapter 4 discuss the results for measurements of binary mixed water aerosol particle ensembles at 78 K. These aerosol particles are formed in a bath gas cooling cell and analyzed in the aerosol phase with rapid-scan Fourier transform infrared (FTIR) spectroscopy. The interpretation of the IR spectra is obtained from comparison to calculated spectra. A detailed description of the bath gas cooling cell and the calculations are presented in Chapter 2 (Section 2.1 and Section 2.2, respectively).

Chapter 3 focuses on the prediction of IR spectra for possible carbon dioxide cloud particles in the Martian atmosphere using the vibrational exciton model and the discrete dipole approximation. Pure carbon dioxide particles formed in the bath gas cooling cell were previously characterized in the Signorell group.^{3,10,11,14,16,24} The formation of water-carbon dioxide core-shell particles in the cooling cell is considered in this chapter to determine if water particles could potentially act as carbon dioxide cloud condensation nuclei in the Martian atmosphere.⁸⁰⁻⁸⁵ The data presented in this chapter may be useful for interpreting atmospheric spectra from future orbiter missions to Mars.

Chapter 4 focuses on ammonia-water aerosol particles and acetylene-water aerosol particles formed in the bath gas cooling cell under similar conditions to the particles studied in Chapter 3. Ammonia-water and acetylene-water aerosols are two other aerosol systems with astrophysical relevance. Ammonia and water are both present in the atmospheres of Jupiter, Saturn, Uranus, and Neptune⁸⁶⁻⁸⁸ while acetylene and ammonia have been detected in the water plumes on Enceladus (one of Saturn's moons).⁸⁹⁻⁹¹

As outlined in Section 1.2, ensemble particle measurements provide data about particle properties that are averaged for the entire system. In order to study, for example, size dependent effects, single particles can be considered. The counter-propagating Bessel beam (CPBB) optical trap used in the current work allows for trapping of both micron and submicron sized particles. While there are a large number of studies that have focused on single particles using optical trapping techniques (e.g. optical tweezing) or other particle trapping methods (see Section 5.1.4 for a further discussion of several single particle techniques), the majority of these studies focus on particles on the order of microns to tens of microns in radius. There are very few studies of single submicron particles. Previous studies of single submicron particles (at room temperature) in the

CPBB optical trap were conducted in the Reid group,⁹²⁻⁹⁶ (the last reference is in collaboration with the Signorell group). No studies have considered submicron particles at low temperatures.

Particles ranging in size (radius, r) from $r = 0.1-1 \mu\text{m}$ represent particles with some of the longest lifetimes in Earth's atmosphere,⁹⁷ and thus it is also important to properly characterize submicron particles.

Chapter 5 presents single aerosol particle studies performed in an optical trap, with the goal of stably trapping micron and submicron particles at low temperatures. Section 5.2 demonstrates trapping of single particles at room temperature to examine RH-induced glassy aerosol formation for aqueous carbohydrate particles (glucose, fructose, raffinose). This section demonstrates that the CPBB optical trap is an attractive method for studying single micron and submicron sized particles over many hours and under ambient conditions. Section 5.3 seeks to extend the capabilities of the CPBB optical trap to a low temperature environment. To this end, a cold trapping cell was designed and constructed and the first freezing experiments for supercooled hexadecane, dodecane, and water are presented here. These substances were chosen based on their melting points in order to show that trapping is stable at different temperatures down 228 K. The low temperature experiments in this thesis represent the first reported freezing experiments for single particles in the submicron size range. The setup and design of the room temperature and low temperature trapping experiments are presented in Chapter 2 (Section 2.3).

Finally, Chapter 6 outlines future goals for complementary ensemble particle and single particle studies at low temperatures. Updates and improvements to the current CPBB low temperature setup are discussed to extend the temperature range for single particle measurements to temperatures as low as 78 K.

Chapter 2: Methods

2.1 Infrared measurements of aerosol particle ensembles

2.1.1 Cooling cell and infrared spectrometer

Ensembles of aerosol particles were formed in a bath gas cooling cell^{8,10,14,35} and characterized by infrared (IR) extinction (absorption + scattering) spectroscopy. The cooling cell is a custom design and allows for the temporal study of aerosol ensembles at low temperatures (4 K-320 K). The specific experimental details for the ensemble measurements in Chapter 3 and Chapter 4 are provided in each chapter. Here, the general design of the cooling cell is presented.

An illustration of the cooling cell is provided in Figure 2.1, including the transfer optics, which connect the spectrometer with the cell and the detector unit. The actual cooling cell (cell volume = 11.3 L, cell diameter = 14.5 cm, cell length = 68.5 cm) in which aerosol particles are formed is surrounded by a second cylinder that contains the liquid N₂ cooling agent. (Note that liquid He can also be used as the cooling agent. The cell can be heated to reach temperatures between 4-320 K in combination with either the liquid N₂ or liquid He cooling agents. However, in this work, only the liquid N₂ cooling agent was used without any heating.) An outer vacuum cylinder protects the cell against heat transfer from the surroundings. The cell is filled with a bath

gas (He or N₂) to the desired pressure (typically a few mbar to 2 bar). Aerosols are formed in the cell by injection of room temperature gases (~ 292 K) into the cold cell. Typically, mixtures of a sample gas in He or N₂ are used. This process leads to supersaturation of the sample gas and thus nucleation and particle formation. The particles remain suspended within the cell (i.e. in the aerosol phase) and their IR extinction spectra can be measured for up to about two hours after injection.

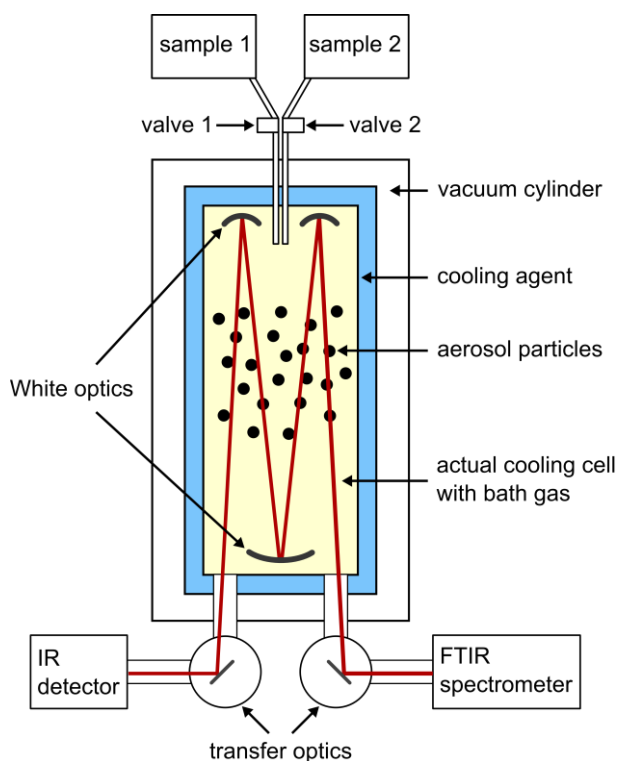


Figure 2.1: Illustration of the bath gas cooling cell.

Sample gas injection occurs via two separate inlets each using a magnetic solenoid valve (Bürkert) (see “valve 1” and “valve 2” in Figure 2.1). This design allows for several different sample injection methods for experiments with two sample gases. (1) Injection of a premixed sample: sample gas 1

and sample gas 2 are first premixed and then injected through the same sample gas inlet (for example, “sample 1” in Figure 2.1). (2) Simultaneous injection of each sample: sample gas 1 and sample gas 2 are injected through different sample gas inlets (i.e. using “sample 1” and “sample 2”, respectively) at the same time. (3) Sequential injection of each sample: sample gas 1 and sample gas 2 are injected through different sample gas inlets (i.e. using “sample 1” and “sample 2”, respectively) with a time delay between the two valve opening pulses. The opening schemes for the valves for these different injection methods are illustrated in Figure 2.2. The applications of the different injection methods will be outlined in Chapter 3 and Chapter 4.

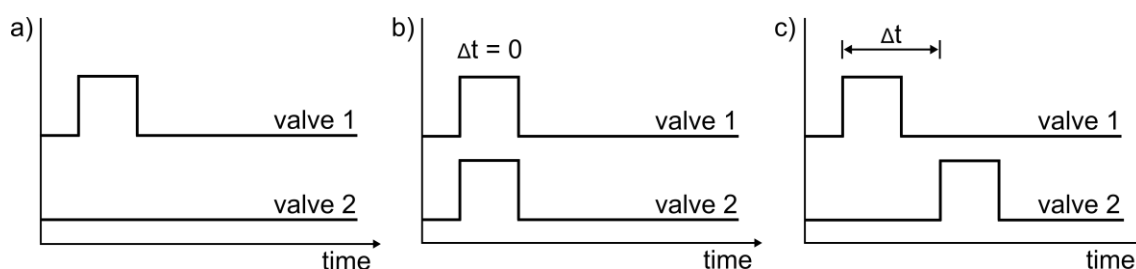


Figure 2.2: The different valve pulse sample injection methods for the cooling cell. a) Injection of a one-component sample or a premixed sample through a single valve, b) simultaneous injection of two separate gas samples, and c) sequential injection of two separate gas samples with a delay time between the start of each valve opening pulse, Δt .

After injection, IR extinction spectra of the suspended particles are measured as a function of time using a Bruker IFS S66v/S rapid-scan FTIR spectrometer. The spectrometer makes use of a Globar light source and the extinction spectra are recorded with a liquid N₂-cooled mercury-cadmium-telluride detector (InfraRed Associates). The IR light travels from the spectrometer to the cooling cell and then to the detector via transfer optics, as shown in Figure 2.1. Spectra were recorded from 500-8000 cm⁻¹ at a spectral resolution of 0.5 cm⁻¹ (time resolution is approximately 380 ms per

scan). A background spectrum (average of 50 scans) was recorded immediately before sample gas injection. Aerosol particle spectra were typically recorded over a time frame of anywhere from 30-120 minutes after injection. Immediately after injection, spectra consisting of single scans are recorded at the highest possible time resolution to observe any rapid changes that may occur in aerosols. As time passes, the particles gradually move out of the path of the beam and the signal intensity decreases. Thus, a greater number of scans are averaged as the measurement progresses. Additionally, the spacing between successive spectra is increased later in the measurement since rapid changes in particle structure, phase, etc. are more likely to occur towards the start of the experiment.

The cell makes use of White optics,⁹⁸ which allow for the IR light to make multiple passes through the cell. The pathlength can be adjusted from four to thirty-two passes to optimize the signal intensity of the sample (this corresponds to pathlengths of ~3.5 m and ~21 m, respectively). In the current work, the cell was set to 8 and 12 passes (Chapter 3) or 32 passes (Chapter 4). Figure 2.3 shows an illustration of the White optics setup.⁹⁸ It consists of three concave mirrors—two placed at one end of the cell (mirrors A' and A'') and one placed at the opposite end (mirror B). Mirror B is centered at the midpoint between mirrors A' and A''. Adjusting the tilt of mirror A' changes the number of times the light passes through the cell. In Figure 2.3, the light makes eight passes through the cell: it enters the cell at point 1, reflects at points 2-8, and exits the cell at point 9.

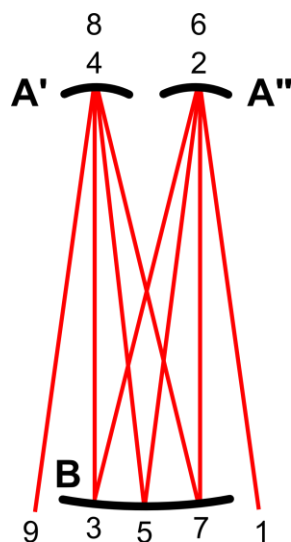


Figure 2.3: Illustration of an example of the passage of infrared light through White optics.⁹⁸ The numbers in the illustration outline the path that the light takes within the optics (eight passes).

2.1.2 Sample preparation

The specific details for sample gas preparations (e.g. concentration of the sample gas in He and sample gas pressure) will be outlined for the respective experiments in Chapter 3 and Chapter 4. A brief description of sample preparation methods is provided in this section. High purity gas samples were prepared in 2 L or 4 L stainless steel cylinders (Swagelok). Gases were prepared to the desired concentration (typically 200-1200 ppm sample gas) by dilution in He (i.e. the same gas used as the bath gas). The cylinders were typically prepared to a total pressure of approximately 8 bar; however, typical sample gas pressures used in experiments (i.e. in sections labelled “sample 1” and “sample 2” in Figure 2.1) can range from 100 mbar to 2 bar. Preparing a large amount of sample gas in a cylinder following this method ensured the use of the same sample gas concentration over multiple experiments. After preparing a cylinder, it was left to sit overnight to ensure mixing of the gases before conducting experiments.

2.2 Simulation of aerosol particle infrared spectra

The interpretation of aerosol IR extinction spectra in this work is done based on comparisons of experimental band shapes to calculated spectra in order to confirm observations. In this thesis, the methods used to simulate particle IR spectra are the vibrational exciton model^{3,10,11,78} (used in Chapter 3 and Chapter 4) and the discrete dipole approximation⁹⁹⁻¹⁰¹ (used in Chapter 3).

2.2.1 Vibrational exciton calculations

Vibrational exciton calculations were used to model the IR extinction spectra for particles less than 10 nm. This is a quantum mechanical method to calculate the IR band shapes for aerosol particles containing up to tens of thousands of molecules.^{3,11,17,78} The vibrational exciton method provides molecular insight into the origin of the IR band profiles of aerosols. For vibrational transitions with large transition dipole moments ($> 0.1-0.2$ D), the band shapes of particle IR extinction spectra are highly dependent on the transition dipole couplings (exciton couplings) across all the molecules within the particle. This dependence allows for the reduction of the calculation to include only this dominant contribution, greatly reducing the computational cost. In the case of strong dipole-dipole couplings in an aerosol particle, the molecular vibrational eigenstates lose their degeneracy, which leads to broad and strongly structured infrared band profiles. This structure depends characteristically on particle properties (size, shape, architecture). In turn, IR spectra can be used to determine particle size, shape, and architecture. This method was applied to all particles below 10 nm because it has been previously shown that the coupling needs to be considered for all molecules within the particle over this dimension.⁷⁸ The dipole interaction between two molecules, i and j , within a particle is proportional to R_{ij}^{-3} , where R_{ij} is the distance between molecule i and molecule j .

In the exciton model,¹¹ the vibrational Hamiltonian, \hat{H} , is given by:

$$\hat{H} = \hat{H}_0 + \hat{H}_{DD} + \hat{H}_{DID} \quad (2.1)$$

where \hat{H}_0 is the vibrational Hamiltonian of the uncoupled molecules and \hat{H}_{DD} and \hat{H}_{DID} are the Hamiltonians of the pairwise dipole-dipole couplings and dipole-induced dipole couplings, respectively. \hat{H}_{DD} and \hat{H}_{DID} can be calculated from:

$$\hat{H}_{DD} = -\frac{1}{2} \sum_{i,j} \mu_i^* \lambda_{ij} \mu_j \quad (2.2)$$

$$\hat{H}_{DID} = -\frac{1}{2} \sum_k \left(\alpha_k \sum_i \lambda_{ki} \mu_i \right)^* \left(\sum_j \lambda_{kj} \mu_j \right) \quad (2.3)$$

where μ_i is the dipole moment vector and α_i is the molecular polarizability tensor for each molecule, i (* is used to denote the transpose). The scaled projection matrix, λ_{ij} is calculated by:

$$\lambda_{ij} = \frac{(1 - \delta_{ij})}{4\pi\epsilon_0 R_{ij}^3} (3e_{ij}e_{ji} - 1) \quad (2.4)$$

where δ_{ij} is Kronecker's delta, R_{ij} is the distance from molecule i to molecule j , and e_{ij} is a unit vector from the centre of mass of molecule i to the centre of mass of molecule j .

\hat{H} can then be written as:

$$\hat{H} = \hat{H}_0 + \sum_{i,j} \mu_i^* A_{ij} \mu_j \quad (2.5)$$

with

$$A_{ij} = -\frac{1}{2} \left(\lambda_{ij} + \sum_k \lambda_{ik} \alpha_k \lambda_{jk} \right) \quad (2.6)$$

To solve the Schrödinger equation with the Hamiltonian given in Equation (2.5), a time-dependent approach is used in which the IR absorption spectra are calculated directly from the dipole auto correlation function.

The vibrational exciton method can be applied to particles of various shapes due to the molecular nature of the calculation. The input parameters for the calculations are the transition wavenumber for the vibration, the molecular transition dipole moment, and the molecular polarizability tensor, which are taken from independent measurements. The specific parameters used in this work (e.g. transition dipole moment, molecular structure) are provided in Chapter 3 and Chapter 4.

2.2.2 Discrete dipole approximation

For particles greater than ~ 10 nm (and up to ~ 100 nm), the IR spectral bandshapes are no longer dependent on particle size (the effective range of the dipole couplings is ~ 10 nm).⁷⁸ Above this size, classical methods, such as the discrete dipole approximation (DDA)⁹⁹ can yield accurate results in less time than would be required using the vibrational exciton model for the same sized particle. The major disadvantage of the DDA is that it requires the frequency-dependent complex refractive index (RI) as input. This data must be obtained from independent measurements (or calculations). As a result, the accuracy of the DDA is highly dependent on the quality of the RI data. The DDA method for calculating the absorption and scattering of light by dielectric particles of arbitrary shape was first proposed by Purcell and Pennypacker.⁹⁹ The method was further extended by Draine and coworkers.¹⁰⁰⁻¹⁰⁶ In the current work, the DDA calculations were performed using the DDSCAT 6.1 program.¹⁰¹

The DDA provides an approximate solution for the scattering of light by both spherical and non-spherical dielectric particles. The approximation in this method refers to the fact that the target particles are approximated by a cubic array of N equally spaced point dipoles (with interdipole spacing, d_s). Each of the polarizable points acquires a dipole moment in response to the incident electric field and also due to the other dipoles in the array (the method is sometimes referred to as the “coupled dipole approximation” for this reason). Figure 2.4 illustrates the representation of a particle by point dipoles. The properties of the bulk are applied to each point (from the complex refractive index). A simple cubic shape is illustrated in this figure; however, more complex shapes are possible, such as truncated cubes, elongated particles, pyramids, etc.

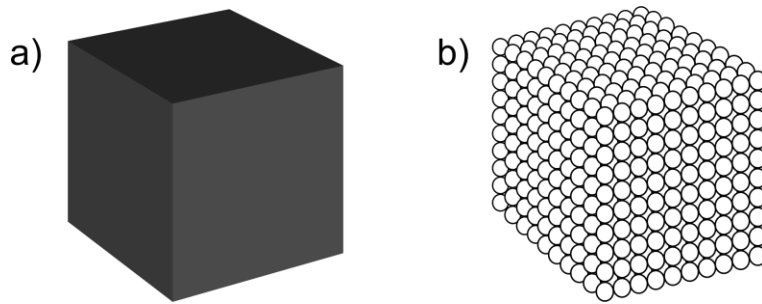


Figure 2.4: a) An example particle (cube) and b) the approximation of the particle by an array of 1000 point dipoles.

Each of the point dipoles represents the polarizability of a sub-volume of the particle. The instantaneous polarization, \mathbf{P}_j , of an individual dipole, j , can be calculated by:¹⁰²

$$\mathbf{P}_j = \alpha_j \mathbf{E}_{ext,j} \quad (2.7)$$

where α_j is the polarizability tensor and $\mathbf{E}_{ext,j}$ is the instantaneous electric field at point j from the incident radiation and the other $N-1$ dipoles. The polarizability at each point is calculated based on

input complex refractive index, n^* , or complex dielectric function, ϵ . Either data set can be supplied since the two are interrelated by:

$$(n^*)^2 = \epsilon \quad (2.8)$$

where:

$$n^* = n + i\kappa \quad (2.9)$$

$$\epsilon = \epsilon' + i\epsilon'' \quad (2.10)$$

with n and κ as the real and imaginary parts of n^* , respectively, ϵ' and ϵ'' are the real and imaginary parts of ϵ , respectively, and i is the complex number.

The Lattice Dispersion Relation¹⁰³ is used to determine the polarizability at each point:

$$\alpha_j = \frac{\alpha_j^{(0)}}{1 + \left(\frac{\alpha_j^{(0)}}{d_s^3}\right) (b_1 + (n^*)^2 b_2 + (n^*)^2 b_3 S)(k_0 d_s)^2} \quad (2.11)$$

where k_0 is the wave vector in vacuo ($k_0 \equiv \omega/c$, ω is frequency and c is the speed of light) and with coefficients¹⁰³ $b_1 = -1.8915316$, $b_2 = 0.1648469$, and $b_3 = -1.7700004$. The term $\alpha_j^{(0)}$ is calculated from:

$$\alpha_j^{(0)} \equiv \frac{3d_s^3}{4\pi} \left(\frac{(n_j^*)^2 - 1}{(n_j^*)^2 + 2} \right) \quad (2.12)$$

where n_j^* is the complex refractive index for point j . The value of S depends on the direction of propagation, \mathbf{a} , and polarization state $\mathbf{e}^{(0)}$ according to:

$$S \equiv \sum_j (\mathbf{a}_j \mathbf{e}_j^{(0)})^2 \quad (2.13)$$

Determination of \mathbf{P}_j then allows for the calculation of the extinction (C_{ext}), absorption (C_{abs}), and scattering (C_{scat}) cross sections. These three cross sections are related by:

$$C_{ext} \equiv C_{abs} + C_{scat} \quad (2.14)$$

In the current work, the extinction spectra are of interest. The extinction cross section can be calculated over the desired wavelength range according to:¹⁰²

$$C_{ext} = \frac{4\pi k_\lambda}{|\mathbf{E}_{inc}|^2} \sum_{j=1}^N \text{Im}(\mathbf{E}_{inc,j}^* \cdot \mathbf{P}_j) \quad (2.15)$$

where $\mathbf{E}_{inc,j}$ is the incident electric field at position j , and \mathbf{E}_{inc} is calculated according to:

$$\mathbf{E}_{inc} = \sum_{j=1}^N \mathbf{E}_{inc,j} \quad (2.16)$$

The value k_λ in Equation (2.15) relates to the wavelength, λ , of the incident light via:

$$k_\lambda = \frac{2\pi}{\lambda} \quad (2.17)$$

The extinction efficiency factor, Q_{ext} , can then be calculated with respect to λ by:

$$Q_{ext} \equiv \frac{C_{ext}}{\pi a_{eff}^2} \quad (2.18)$$

The DDA yields accurate results provided that two main criteria are met:¹⁰⁴ (1) the interdipole separation, d_s , should be much smaller than the wavelength of light, λ , and (2) d_s should be much smaller than the dimensions of the particle and accurately describe the particle geometry. The value of d_s is considered to be adequate provided the following inequality is satisfied:

$$|n^*|d_s k_\lambda < 1 \quad (2.19)$$

The latter condition can also be considered in terms of a particle effective radius, a_{eff} , which denotes the radius of a sphere with a volume, V , equal to that of the particle of interest:

$$a_{eff} \equiv \sqrt[3]{\left(\frac{3V}{4\pi}\right)} \quad (2.20)$$

The number of dipoles is then sufficient provided that the following condition is satisfied:

$$N > \left(\frac{4\pi}{3}\right) |n^*|^3 (k_\lambda a_{eff})^3 \quad (2.21)$$

Note that the volume of the particle is related to the number of point dipoles and the dipole spacing by:¹⁰¹

$$V = N d_s^3 \quad (2.22)$$

The calculations in the current work were typically done for particle shapes approximated by anywhere from about 2×10^4 to 2×10^5 point dipoles. In general, the calculated cross sections can

be considered to be accurate provided $N > 1 \times 10^4$.¹⁰¹ Other parameters (e.g. particle size, shape, architecture, etc.) used for the calculations in Chapter 3 will be provided within that chapter.

2.3 Optical trapping of single aerosol particles

This section describes the design of the experimental optical trapping setups at both room temperature and at low temperatures down to 223 K. A more complete description of optical trapping in general, of Bessel beams and their formation, and of the counter-propagating Bessel beam (CPBB) optical trap and its advantages will be provided in Section 5.1.

There are many similarities between the setup for the room temperature and the setup for low temperature experiments. The design of the room temperature experiments is presented first, followed by the additional equipment required to carry out experiments in a (low) temperature-controlled environment.

2.3.1 Trapping at room temperatures

2.3.1.1 Optical trap

Figure 2.5 details the setup for the CPBB optical trap at room temperature. This setup is the same as that used in the work of Lu et al.⁹⁶ and similar to the setup used by Carruthers et al.⁹⁴ A 532 nm continuous wave laser (Laser Quantum, Opus 3, typical laser power 1900 mW) was expanded by telescope from 2 mm to approximately 4 mm (beam radius). The expanded Gaussian beam then passed through a plano convex axicon with a 176° apex angle (Altechna) to form the Bessel beam. The resulting Bessel beam had a core radius of 2 μm (8 mW core power in the trapping region). A polarization beam splitter (PBS) cube splits the Bessel beam into two orthogonally polarized arms.

These two beam arms overlap within the cell (see Section 2.3.1.2) to form the “trapping region” where single aerosol particles are trapped. The forces that determine this trapping region (gradient and scattering forces) will be discussed in Section 5.1.1. A more detailed discussion of Bessel beams, their formation and the CPBB optical trap will be provided in Section 5.1.2 and Section 5.1.3, respectively.

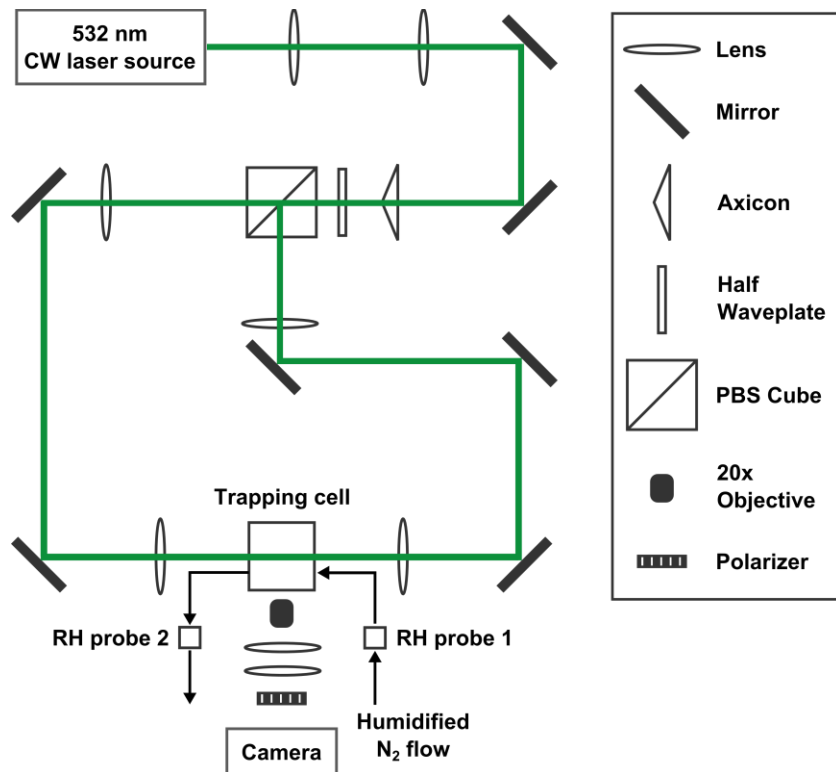


Figure 2.5: Illustration of the optical trapping setup at room temperature (CW = continuous wave, RH = relative humidity, PBS = polarization beam splitter).

2.3.1.2 Trapping cell

A scheme of the room temperature trapping cell is shown in Figure 2.6. The cell has a volume of $\sim 3.4 \text{ cm}^3$ and was constructed in the in-house machine shop (UBC) with BK7 windows. A pair of

mass flow controllers (Bronkhorst EL-Flow, Series F-201CV) was used to control the humidity within the cell by controlling the relative flow rates of dry, high-purity N_2 and N_2 passed through a bubbler. The maximum flow rate is 50 mL/min for each of the mass flow controllers. Two humidity probes (Honeywell, HIH-4602-A/C) located before and after the cell along the path for the N_2 flow measured the temperature and relative humidity (RH) before and after the cell (approximately 5 cm from the cell). Each probe has an accuracy of $RH \pm 3.5\%$ at 293 K. The average of the two RH probe readings was taken to be the RH within the cell. The RH within the cell varied from $\sim 70\%$ to 0% during experiments. All measurements in Section 5.2 were performed at room temperature (typically 292 K). The temperature fluctuation within the cell during experiments was typically ± 0.5 K. Particles remained trapped in the cell under a constant N_2 flow for up to 32 hours.

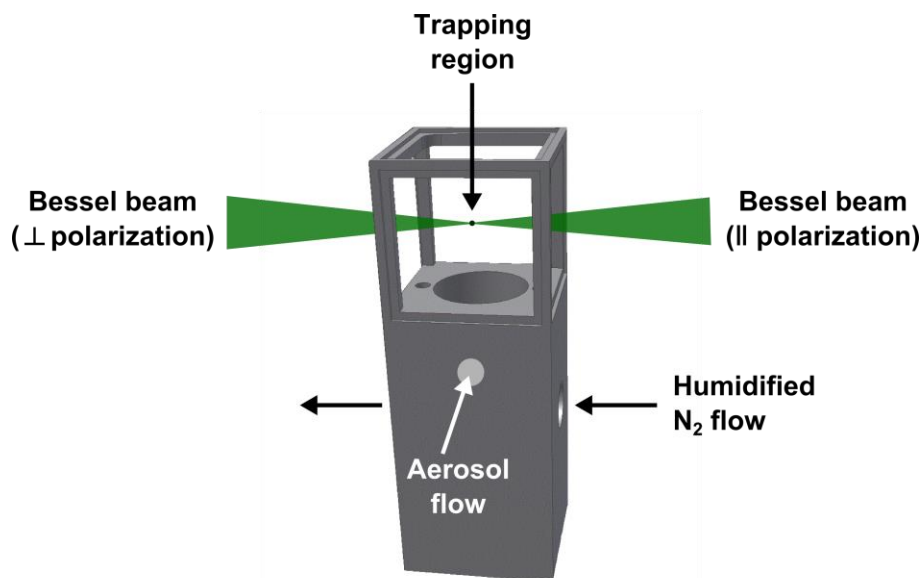


Figure 2.6: The room temperature optical trapping cell. The dimensions of the cell are $1.5 \text{ cm} \times 1.5 \text{ cm} \times 1.5 \text{ cm}$.

2.3.1.3 Particle generation

Aerosols were generated at room temperature using a medical nebulizer (Pari, PARI Boy SX). The aerosols enter the room temperature cell from below the trapping beams (perpendicular to the Bessel beam plane) by placing the nebulizer next to the hole for aerosol flow (labelled in Figure 2.6). Individual particles from the cloud of generated aerosols are captured in the trapping region within the cell. Particles generated by the nebulizer range in size from nanometers to several microns in radius, with a median particle radius of 1.75 μm .

2.3.2 Trapping at low temperatures

2.3.2.1 Low temperature trapping cell

The optical setup for the low temperature trapping cell is similar to what is described for the room temperature trap in Section 2.3.1.1. Figure 2.7 shows a diagram for the low temperature trap setup. The only difference between this figure and Figure 2.5 is in the trapping region. The particles are trapped within a cell that allows for temperature control (Figure 2.8). The body of the cell was made from oxygen-free high thermal conductivity copper and was machined at the ETH machine shop. Stainless steel tubes are attached to the main body of the cell and are connected to a closed-cycle refrigerated circulator (Lauda, Proline RP 1290). The cell is cooled by the flow of an oil-based coolant (Atelier für Metallbau, Wärmeträger Fluid WTF 190) through the stainless steel tubes and through the cell body.

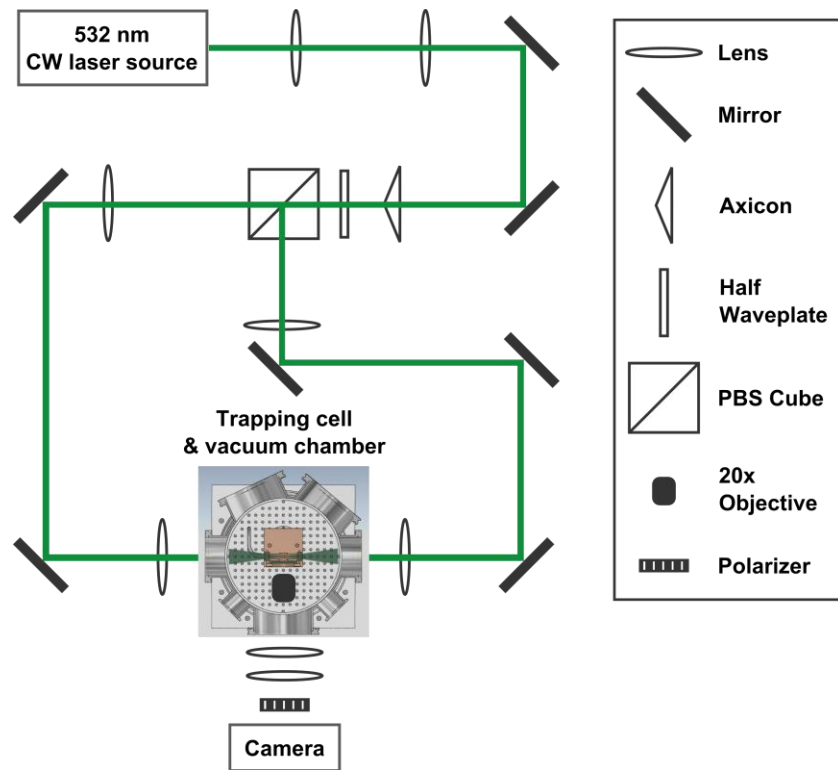


Figure 2.7: Illustration of the optical trapping setup for the low temperature trapping experiments (CW = continuous wave, PBS = polarization beam splitter).

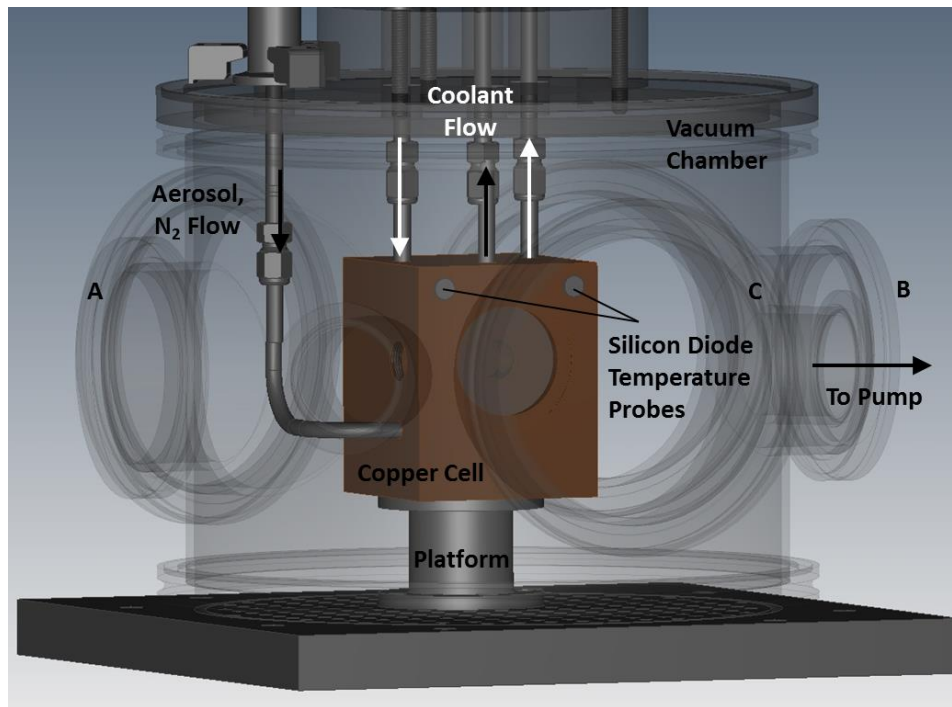


Figure 2.8: The copper cell and vacuum chamber used in the low temperature trapping experiments. The vacuum chamber has been lightened to facilitate viewing of the copper cell. The copper cell is placed on an insulating platform and attached to a breadboard. The vacuum chamber is also attached to the breadboard, which is secured to the laser table. Reprinted with permission from *Review of Scientific Instruments*, 2014, **85**, 095107. Copyright 2014, AIP Publishing LLC.

The temperature of the copper cell is measured by two silicon diode temperature sensors (Lakeshore, DT-670 Series) that are positioned at the top corners on the outer surface of the cell. During the experiments, the difference in the temperature readings of each probe is 0.03 K and there is an absolute uncertainty for each sensor of ± 0.025 K. The difference between the temperature at the surface of the cell and the temperature in the trapping region is approximately ± 0.5 K; however, the periodic fluctuation of the temperature in the trapping region appears to be accurately represented by the silicon diode probes at the cell surface. Note this method for

measuring the temperature was used for the preliminary freezing experiments that are presented in this work and will be updated for future experiments to gain a more accurate reading of the temperature in the trapping region of the cell. These updates will be discussed in Section 5.3.5.

Figure 2.9 shows a cross-section of the copper trapping cell. The central trapping region of the cell has a volume of 0.6 cm^3 . On either side of the trapping region are the arms for passage of the Bessel beams, creating a total volume of 1.6 cm^3 . Each of the Bessel beams pass through a BK7 window (Edmund Optics), each 15 mm in diameter (3 nm thickness) with a 532 nm coating (to minimize scattered light). These windows separate the inside of the cell from the surrounding vacuum.

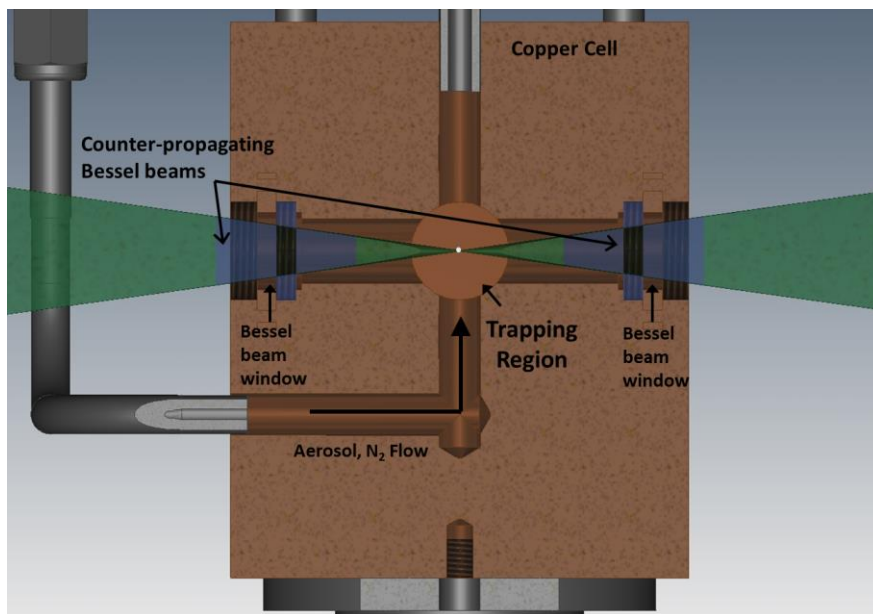


Figure 2.9: A cross-sectional view of the copper trapping cell. Reprinted with permission from *Review of Scientific Instruments*, 2014, **85**, 095107. Copyright 2014, AIP Publishing LLC.

Aerosol particles enter into the cell via a stainless steel tube after being generated by a medical nebulizer (same method as for room temperature experiments, see Section 2.3.1.3). This same tube

is used for the flow of high purity N₂ (dry or humidified) into the cell. The aerosols and N₂ flow enter the cell perpendicular to the plane of the Bessel beams from an entry point directly below the trapping region (see Figure 2.9).

A N₂ flow is typically used during experiments at a flow rate of 0.25-10 mL/min using a pair of mass flow controllers (Bronkhorst, EL-FLOW Mass Flow Meters, Series F-201CV). A high flow rate (4-10 mL/min) is used initially to remove excess particles from the cell, leaving behind only the optically trapped particle. Once the excess particles are removed from the cell, the flow is decreased to 0.25-0.5 mL/min for the remainder of the experiment. For certain experiments, the N₂ flows through copper tubing immersed in a chiller (Fisher Scientific, Isotemp 3016) set at 273-286 K before entering the cell. There is a stainless steel tube directly above the trapping region that is open to the atmosphere to allow for the flow of N₂ through the trapping region of the copper cell. The pressure inside the cell remains at approximately 1 atm during experiments with this constant N₂ flow.

2.3.2.2 Vacuum chamber

A vacuum chamber was required to provide thermal insulation between the cold copper trapping cell and the lab environment. The copper cell sits at the centre of this chamber. An illustration of the chamber surrounding the copper trapping cell is provided in Figure 2.8. The vacuum chamber was custom designed from a standard chamber from Hositrad Vacuum Technology with a diameter of 24 cm and volume of $7.2 \times 10^3 \text{ cm}^3$. The Bessel beam arms pass through Flanges A and B and Flange C allows for collection of the elastically scattered light. Each of these flanges contains 50 mm diameter (5 mm thickness) BK7 windows (UQG Optics). A turbomolecular pump (Pfeiffer Vacuum)

is connected to the chamber as labelled in Figure 2.8. The pressure in the chamber is on the order of 10^{-5} - 10^{-6} mbar during experiments (for cell temperatures of 226-330 K).

2.3.3 Particle characterization

For both the room temperature trapping experiments and the low temperature trapping experiments, elastic light scattering by the trapping laser is used for particle characterization. From the scattered light, the particle size and the onset of freezing (see Section 5.3.3) were determined. Particle sizing was performed based on the scattering patterns for the elastically scattered light from particles. In general, data was collected in the same manner for both the room temperature setup (Section 2.3.1) and the low temperature cell setup (Section 2.3.2). Unless noted, the description of the data acquisition methods (Section 2.3.3.1) applies to both the room temperature and the low temperature cell trapping experiments. The methods for data analysis and the associated errors (Section 2.3.3.2 and Section 2.3.3.3) apply to both experiments.

2.3.3.1 Data acquisition

During experiments, the perpendicularly polarized elastically scattered light from particles is collected for analysis. This is the light scattered by the particle from the trapping Bessel beam (i.e. 532 nm) collected around a scattering angle, $\theta_{sc} = 90^\circ$ relative to the forward scattering direction. (In the case of the low temperature trap, the scattered light exits the copper cell through a 50 mm diameter (3 mm thickness) BK7 window.) The light is collected and focused using a 20 \times objective (Mitutoyo, Plan Apo Infinity-Corrected Objective, working distance = 20.0 mm, numerical aperture = 0.42). The objective has a theoretical angular range of 49.6° ; however, room temperature experiments using dodecane particles have found that the actual collection range is approximately 46° centered at $\theta_{sc} = 90^\circ \pm 3^\circ$.⁹⁶ (For the low temperature trap, the objective is

located within the vacuum chamber (see Figure 2.7) on an XYZ Gothic-arch bearing translational stage (Newport, #9061-XYZ-PPN-M) with Picomotor actuators (Newport, #8302). This allows for translational movement of the objective within the vacuum chamber during experiments. The scattered light then exits the vacuum chamber through a BK7 window at Flange C (see Figure 2.8.) The scattered light passes through a series of lenses and a polarizer and the perpendicularly scattered light is recorded with a CMOS camera (Thorlabs, DCC1645C, 1280×1024 pixels).

2.3.3.2 Data analysis

Particle sizing was performed using the images of elastically scattered light (perpendicularly polarized) collected around 90° relative to the forward scattering direction and in the scattering plane. The angular range for data collection was approximately 66° - 114° . Figure 2.10(a) shows an example of a collected scattering image from a single hexadecane particle in the liquid phase. The scattering image is integrated to obtain a phase function plot of intensity vs. scattering angle (see Figure 2.10(c), experimental phase function). This phase function is then fit according to Mie theory to determine the particle size.

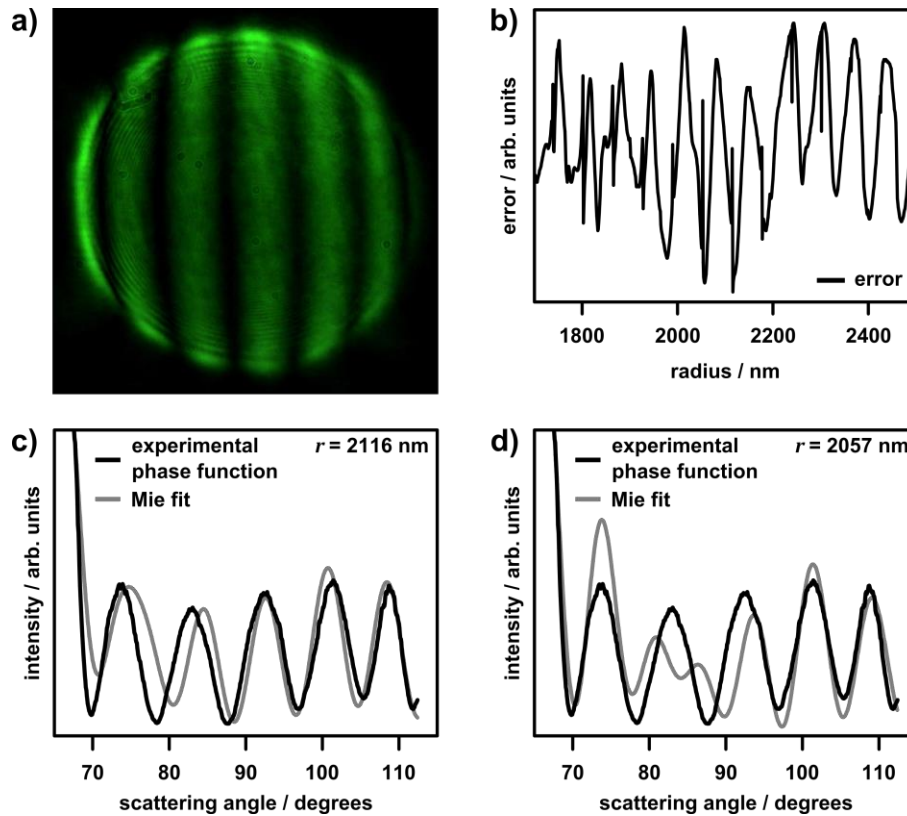


Figure 2.10: a) Image of the perpendicularly polarized light scattered from a liquid hexadecane particle, b) the errors associated with Mie fits over the input size range (radius, r) of 1700-2500 nm, c) comparison between the experimental phase function and the best fit according to Mie theory ($r = 2116$ nm), and d) comparison between the experimental phase function and the second best fit according to Mie theory ($r = 2057$ nm).

Mie theory describes the scattering of light by a small, homogeneous sphere by providing a solution to Maxwell's equations for the scattering of the electromagnetic radiation.² This scattering is known to be strongly dependent on both the size and the RI of the sphere over a given angular range. Thus, if an experimental scattering pattern for a homogeneous sphere is known over a specified angular range, along with the RI of the material, Mie theory can be used to determine the size (in this work, the particle radius, r) of the sphere.

Figure 2.11 shows the scattering patterns for 532 nm light (parallel and perpendicular polarizations) scattered by a hypothetical sphere, with $r = 1.4 \mu\text{m}$ and real part of the complex RI $n = 1.445$. The scattering patterns over 360° were calculated from Mie theory as implemented in the MiePlot software.¹⁰⁷

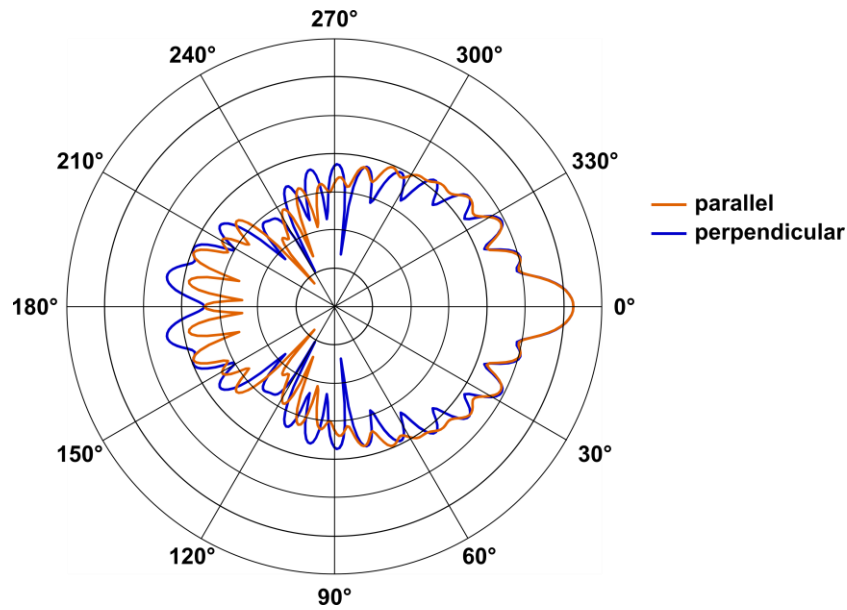


Figure 2.11: Mie scattering polar plot for 532 nm light scattered by a hypothetical particle with $r = 1.4 \mu\text{m}$ and $n = 1.445$. The scattering intensities are plotted on a logarithmic scale with respect to the scattering angle, θ_{sc} .

The Mie fits to the experimental data are performed using a custom program designed within the LabVIEW software.⁹⁴ In order to determine the size of particles according to Mie theory, several parameters are required to be input into the calculation: the RI, the scattering angles, and the laser polarization. Mie scattering phase functions are then calculated over a chosen size range to determine the best fit to the experimental data. An error is calculated for each of the sizes over the input size range as an error difference, D , according to:

$$D = \sum_a (I_{a,pf} - I_{a,Mie})^2 \quad (2.23)$$

where the intensity profiles for the experimental and calculated (Mie theory) phase functions are represented by $I_{a,pf}$ and $I_{a,Mie}$, respectively, for the total number of phase functions, a .⁹⁴ The best fit is determined to be the one with the lowest value for D . The best fit is typically also confirmed by visual comparison of the experimental phase function to the calculated fit. A variety of input size ranges can be tried until the best fit to the experimental data is found. The program also allows for a variation of the centre value for the scattering angles while keeping the total angular range constant. Typically, the central value ($\theta_{sc} = 90^\circ$) is allowed to vary by $\pm 3^\circ$ (see Section 2.3.3.1) while keeping the total angular range constant at 46° to 48° .

The plot in Figure 2.10(c) shows the comparison between an experimental phase function and the corresponding best fit from Mie theory. Figure 2.10(b) shows a plot of the error over the size range from $r = 1700$ nm to $r = 2500$ nm. The size found to have the lowest error was $r = 2116$ nm. Visual comparison of the experimental phase function and the calculated Mie fit (Figure 2.10(c)) shows that the fit appears to be quite reasonable. The errors associated with the fitting method (and the error for each size result) will be discussed in Section 2.3.3.3.

Sizing for both the room temperature experiments and the low temperature cell experiments were performed according to the above method. However, this sizing method can only be used for spherical particles, and thus is primarily applicable to liquid particles. The phase functions for solid particles with a crystalline structure (i.e. non-spherical) will be discussed in Section 5.3 with respect to the freezing experiments.

2.3.3.3 Errors and limitations

There are errors inherent to the sizing methods described in Section 2.3.3.2 and thus an error associated with the sizing results for particles. As well, there are limitations over which size range the current method is accurate (with the current experimental setup). This section will discuss the source of these errors and limitations and how they affect the quoted particle sizes in this work.

From the error plot in Figure 2.10(b), it is clear that there are two size results that have similar values of D : $r = 2116$ nm and $r = 2057$ nm. The difference in the D values for these sizes is only ~ 0.006 . The Mie fit calculated for $r = 2116$ nm and $r = 2057$ nm are each shown in Figure 2.10(c) and Figure 2.10(d), respectively. The fit at 2116 nm looks to be a better match to the experimental phase function, and thus this is taken to be the sizing result for this particle. In general, the separation between two local error minima can be up to 150 nm. As a result, the sizing results for particles in this work will carry a general error of ± 150 nm.

There are, of course, other errors associated with the sizes calculated for particles. One possible error is in the value of the RI used in the calculation. RI data for all the substances studied in this work are known, but may not be available at the desired wavelength. When the RI for a specified substance is not available at 532 nm and the appropriate temperature, the value can be estimated from literature values at other wavelengths and temperatures assuming a Cauchy relationship¹⁰⁸ for the RI variation with respect to wavelength (refer to Section 5.3.3, Equation (5.31)). The effect of a small difference in the input RI of a substance has been tested (e.g. using a value at a different wavelength or temperature), and typically the difference in the sizing results is within ± 150 nm.

It is clear from the scattering plot in Figure 2.11 that accurate knowledge of the scattering angle range is important for accurate Mie fitting results. However, as for the error associated with the RI

value, changes to the scattering angles tend to have an effect on sizing results that is within ± 150 nm. The method for adjusting the scattering angles during the fitting process was discussed in Section 2.3.3.2.

The current method for sizing particles can only be used to size particles greater than approximately $r = 300$ - 400 nm. This limitation is related to both the scattering wavelength (532 nm) and the $20\times$ objective that are used in the current experiments (the objective controls the angular range of scattered light that is collected) as well as the RI, n , for the substance. Figure 2.12(a) shows calculated scattering phase functions for hypothetical particles of different sizes ($n = 1.445$) over an angular range of 66° - 114° . Over this angular range, it is clear that for particles below about 300 nm, there is very little structure in the phase function that can be used for fitting. The effect of different values for n is shown in Figure 2.12(b) for 400 nm particles.

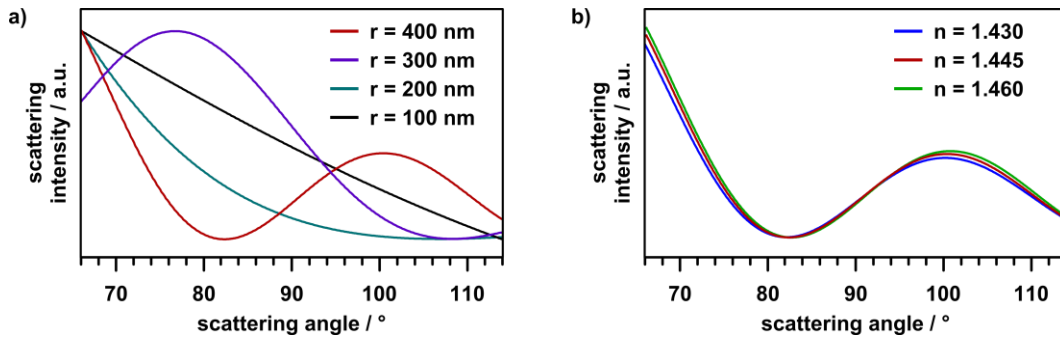


Figure 2.12: a) Scattering phase functions (perpendicularly polarized 532 nm light) calculated for hypothetical particles with $n = 1.445$ over the same angular range as for data collected in the current work. The particles range in size from $r = 100$ nm to $r = 400$ nm. The phase functions were scaled to the same maximum and the ordinates are the scattering intensities in arbitrary units. b) Scattering phase functions calculated for 400 nm particles with different values for n . The phase functions are plotted on the same scale, in arbitrary units.

Chapter 3: Predicting the infrared band profiles for CO₂ cloud particles on Mars*

This chapter focuses on ensemble measurements of carbon dioxide-water aerosols formed in the bath gas cooling cell. Spectra were compared to calculated spectra for a variety of possible CO₂ particles that may be present in the Martian atmosphere. Calculations were performed using both the discrete dipole approximation and the vibrational exciton model. The goal of this work was to provide spectra that may be useful for comparison to data obtained for cloud particles in the Martian atmosphere from future orbiter missions.

3.1 Introduction

The formation of CO₂ clouds on Mars and the properties of these cloud particles is an area of active study. The Martian atmosphere is primarily composed of CO₂ gas (about 95% by volume).¹⁰⁹ Generally, condensation of a planet's major atmospheric constituent is not a common occurrence, and thus the microphysics of such processes, including the formation of CO₂ aerosols on Mars, are

*Reprinted from *Icarus*, 223, M. Isenor, R. Escibano, T.C. Preston, R. Signorell, Predicting the infrared band profiles for CO₂ cloud particles on Mars, pp. 591-601, Copyright 2013, with permission from Elsevier.

currently not well understood.^{80,81,110-112} In addition, CO₂ clouds likely impact the Martian climate, but to study these effects, a greater knowledge of cloud particle properties is required.^{80,81,113-115}

Despite data from numerous missions to Mars, the properties of CO₂ cloud particles (e.g. size, shape) are currently not well known. A thorough summary of Martian mesospheric CO₂ cloud observations was compiled by González-Galindo et al.¹¹² Several size estimates (effective radii) have been proposed for CO₂ cloud particles, including < 100 nm,¹¹⁶ 0.5-2 μm,¹¹⁵ 0.1-0.3 μm,¹¹⁷ 1-2 μm,¹¹⁰ 1-3 μm,¹¹⁸ and 0.1 or 1.5 μm.¹¹⁹ CO₂ particle size estimates have always been derived from Mie theory, which assumes spherical particles. While there are no direct observations of particle morphologies in the Martian atmosphere, CO₂ cloud particles are expected to be cubic or octahedral based on the cubic crystal structure of CO₂.^{110,120} Laboratory studies of CO₂ deposition, either onto a bulk CO₂ ice surface¹²¹ or a cold specimen substrate at Martian surface pressures,¹²² resulted in formation of predominantly bipyramidal particles. Previous work in our group studying CO₂ aerosols in a bath gas cooling cell resulted in particles with mainly truncated cubic morphologies.^{24,123} Although the condensation of CO₂ in the Martian atmosphere is not fully understood, it is generally accepted that homogeneous CO₂ nucleation is less likely due to the extremely high supersaturations that would be required.⁸⁰⁻⁸⁵ Thus, CO₂ cloud formation likely occurs via heterogeneous nucleation, with possible substrates including water, dust, and/or water-coated dust.^{80-85,124,125}

The analysis of infrared (IR) spectra of Martian CO₂ clouds from any future orbiter missions to Mars requires an understanding of how particle properties relate to spectra. We intend for the spectra presented in this paper to act as a guide for the analysis of future occultation spectra (extinction spectra) of CO₂ clouds in the Martian atmosphere. For that purpose, we model IR extinction (absorption + scattering) spectra for possible CO₂ cloud particles in the region of the ν_3

antisymmetric stretching vibration ($\sim 2345 \text{ cm}^{-1}$ or $\sim 4.3 \text{ }\mu\text{m}$). The CO_2 antisymmetric stretching motion was previously used as a marker for CO_2 , for example, on several of Saturn's satellites¹²⁶ as well as on Mars.^{110,118} The shape of this absorption band is highly sensitive to particle properties^{3,10,12,14,16,24,78} and thus can provide insight into the physical characteristics of CO_2 cloud particles. We focus mainly on pure CO_2 particles, H_2O - CO_2 core-shell particles (a H_2O particle completely surrounded by a CO_2 ice layer of even thickness), and H_2O - CO_2 particles where CO_2 forms patches on H_2O cores rather than a complete shell. We consider the effect that particle size, shape, and architecture have on the shape of the CO_2 ν_3 band. As well, we examine the effect of molecular mixing in the interface region of H_2O - CO_2 core-shell particles and we consider CO_2 particles with a dust core in place of the water core. These calculated extinction spectra can then be compared to IR spectra of CO_2 clouds in the Martian atmosphere and give insight into which particle properties can be discerned on the basis of IR band shapes. Because the suggested cloud densities on Mars are very low we do not consider multiple scattering in our calculations.

There exist numerous experimental studies of $\text{H}_2\text{O}/\text{CO}_2$ thin films in the IR.¹²⁷⁻¹³⁸ Many have found that molecular mixing can occur between H_2O and CO_2 , but this is highly dependent on sample temperature. Most of these studies were not performed with relevance to Mars. Experimental studies of $\text{H}_2\text{O}/\text{CO}_2$ aerosols with Fourier transform IR spectroscopy (FTIR) are limited^{55,66,70} and none have reported formation of H_2O - CO_2 particles with a core-shell architecture. Both Devlin et al.⁶⁶ and Taraschewski et al.⁷⁰ concluded that CO_2 may form patches on the surface of H_2O particles in their experiments. However, a thorough analysis of spectral features was not performed in either study. We have chosen to experimentally investigate the potential formation of H_2O - CO_2 core-shell aerosols in our bath gas cooling cell more carefully and compare our results to calculated spectra to support our conclusions.

3.2 Methods

3.2.1 Discrete dipole approximation

The discrete dipole approximation (DDA), as implemented in DDSCAT 6.1,¹⁰⁰⁻¹⁰³ was used to model IR extinction spectra of possible CO₂ cloud particles. A detailed description of this theory can be found in Section 2.2.2. DDA can be applied to dielectric particles of arbitrary geometry (approximated by a cubic array of equally-spaced point dipoles) with sizes similar to or smaller than the wavelength of incident light.⁹⁹ The light-particle interaction is described within the frame of classical electrodynamics and the complex refractive index (RI) of the bulk is used for the particle's optical properties.

DDA was used to model the CO₂ ν₃ band to examine the effects of size, shape, architecture, and core material for particles ranging in size from 10 nm to 1 μm. The bulk RI data used as input in this work are for H₂O ice (cubic, 150 K),¹³⁹ CO₂ ice,¹⁴⁰ FeO,¹⁴¹ and Fe₃O₄ (magnetite).¹⁴² The applicability of DDA is limited by the availability of RI data and such data is rarely available for molecularly mixed substances. Additionally, the IR spectral features of particles less than 10 nm cannot be accurately reproduced using DDA. Thus, to consider each of these cases, exciton calculations were performed as outlined below.

3.2.2 Vibrational exciton model

The vibrational exciton model is described in detail elsewhere^{3,10,11,78} and in Section 2.2.1. Briefly, it is a quantum mechanical model to calculate IR spectra of molecular nanoparticles. It was previously shown that resonant transition dipole coupling (exciton coupling) leads to highly structured IR band shapes that are strongly dependent on particle size, shape, architecture, and

composition for vibrational bands with large transition dipole moments (> 0.1 Debye).^{3,10-12,15-17,19,20,24,78,79} In the exciton model, the calculation of IR absorption is reduced to this dominant interaction and the prediction of spectra for large molecular aggregates (tens of thousands of molecules) is tractable.

Calculations were performed for CO₂ particles ranging from 1-10 nm (i.e. the size range where DDA is no longer valid) for the ν_3 band of CO₂ (transition dipole = 0.32 Debye). All calculations were convoluted with a 4 cm⁻¹ Voigt profile, unless otherwise noted. This accounts for additional broadening effects such as coupling to phonons. Note that these couplings have no significant influence on the band structure arising from the exciton coupling. The vibrational exciton model is a molecular approach which does not require RI data as input, and thus it is possible to analyze molecularly mixed systems. In core-shell particles, exciton calculations were used to investigate the influence of a molecularly mixed H₂O/CO₂ interface layer between the H₂O core and CO₂ shell. Generation of these mixed CO₂/H₂O interface structures is outlined below.

3.2.3 Mixed H₂O/CO₂ unit cells

To simulate spectra of H₂O-CO₂ core-shell particles with a molecularly mixed interface, mixed H₂O/CO₂ unit cell structures were required. A 32-molecule amorphous water cell was used as an initial structure and H₂O molecules were replaced by CO₂ molecules to create mixed cells with H₂O:CO₂ ratios of 28:4, 24:8, 20:12, 16:16, 12:20, 8:24, and 4:28. Density functional theory (DFT), as implemented in SIESTA,^{143,144} was used to perform a relaxation of the geometry for each of the mixed cells to minimize unfavourable interactions between the molecules. These relaxed geometries were used to create the structures to model H₂O/CO₂ mixing in vibrational exciton calculations of core-shell particles.

3.2.4 Experimental

Aerosol particles were generated in a bath-gas cooling cell, which is described in detail elsewhere^{10,14,22} and in Section 2.1.1. Briefly, the cell was cooled to 78 K with liquid nitrogen and then filled with helium bath gas. Before use, the helium bath gas (Praxair, 99.999%) was further purified by flowing through a liquid nitrogen trap to remove trace amounts of water. Injection of dilute, room temperature gases into the cold cell leads to supersaturation and aerosol particle formation. Particles, in the aerosol phase, were analyzed in situ with a Bruker IFS66v/S rapid-scan FTIR spectrometer (~ 380 ms per scan at 0.5 cm^{-1} spectral resolution), typically over a period of about 30 minutes.

Previous work in our group established the formation of N_2O - CO_2 core-shell particles in the cooling cell.¹⁶ These conditions were applied to the $\text{H}_2\text{O}/\text{CO}_2$ system with the goal to clarify whether H_2O - CO_2 core-shell particles can form at all under optimized conditions. CO_2 (Praxair, 99.998%) and N_2O (Praxair) were each prepared to ~ 200 ppm in He while H_2O (UltraPure, Cayman Chemical) was either ~ 200 ppm or ~ 640 ppm in He. Sample gases (room temperature, total pressure of 2 bars) were each injected into the cold cell (500 mbar He) by opening two separate magnetic valves. The pulse opening times for each valve ranged from 300 to 1000 ms. With these valves, it is possible to introduce a delay (typically 1000-2000 ms) between pulses (referred to as “sequential injection”), in order to coat the core particles with the shell component. If no delay is used between the two pulses, we use the term “simultaneous injection”.

3.3 Overview spectra of aerosols spectra in the mid-IR

Experimental spectra of solid CO₂, H₂O, and CO₂/H₂O aerosols are presented in Figure 3.1 to provide an overview of the extinction for each of these aerosols in the mid-IR at 78 K. We use units of wavenumber (cm⁻¹) to describe IR radiation, but also include an axis of corresponding wavelength (μm) in this figure to facilitate conversion between the two units. A spectrum of pure CO₂ aerosols is shown in Figure 3.1(a). The ν₂ band at ~ 670 cm⁻¹ is the doubly-degenerate bending mode and the ν₃ band at ~ 2360 cm⁻¹ is the antisymmetric stretching mode. Also present in the spectrum are combination bands at 3600 cm⁻¹ and 3708 cm⁻¹ and the ¹³CO₂ ν₃ band at 2283 cm⁻¹ that results from the natural abundance of ¹³CO₂ in the sample. A spectrum of pure H₂O aerosols is shown in Figure 3.1(b). The broad libration (lattice vibration) is visible from ~ 600-1000 cm⁻¹, the low intensity ν₂ band is the bending mode, and the broad band from ~ 3000-3600 cm⁻¹ results from the ν₁ and ν₃ modes, which are the symmetric and antisymmetric stretching modes, respectively. A very small peak is present at ~ 3678 cm⁻¹ and is the result of the “dangling OH” stretching motion (free OH at the surface of the particles and not involved in hydrogen bonding⁵⁶). Finally, a spectrum of CO₂/H₂O aerosols (formed by injection of a mixed H₂O/CO₂ sample) is shown in Figure 3.1(c).

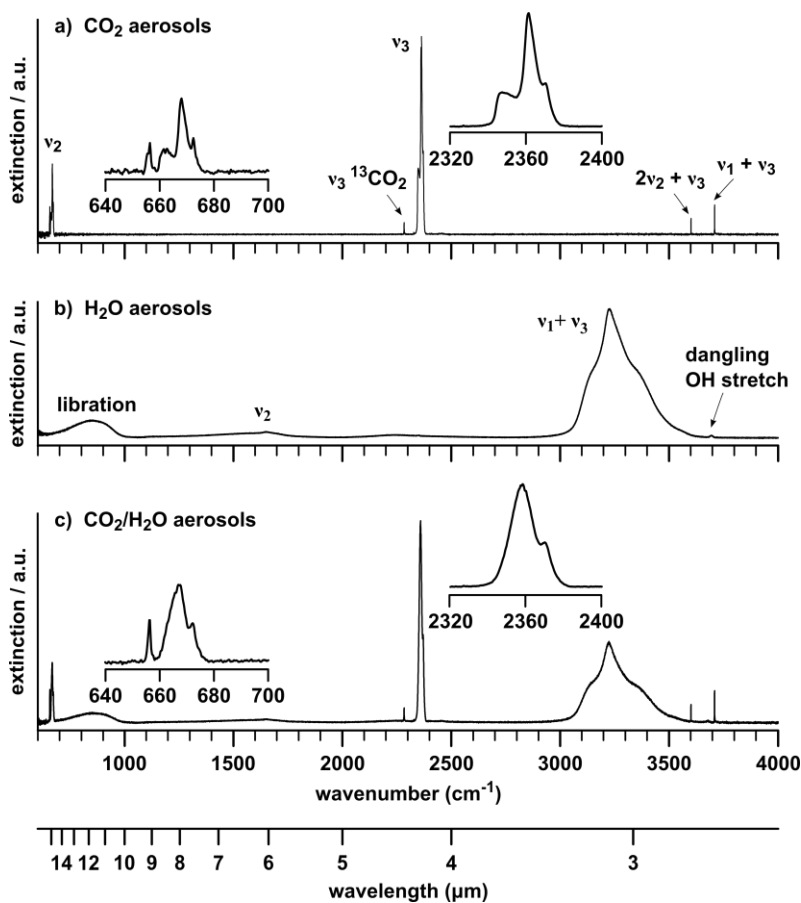


Figure 3.1: Experimental IR extinction spectra of aerosol particles generated in our bath gas cooling cell (78 K). Overview spectra are provided for a) pure CO₂ aerosols, b) pure H₂O aerosols, and c) mixed CO₂/H₂O aerosols.

In this paper, we focus on the CO₂ v_3 band. This band is highly sensitive to particle size, shape, architecture, and structure^{3,10,12,14,16,24,78} and can provide insight into these properties. This sensitivity becomes evident in the comparison of Figure 3.1(a) and (c). There is a distinct change in the shape of the CO₂ v_3 band with and without the presence of H₂O (see insets). The CO₂ v_2 band exhibits qualitatively similar features to that of the v_3 band, seen in the insets in both Figure 3.1(a) and (c). However, the v_2 band is split into two components. The v_2 band has previously been used,

for example, to study CO₂ around stellar objects.¹⁴⁵ We do not discuss the ν_2 band in this paper; our results for the ν_3 band can be applied to the ν_2 band, while keeping in mind this splitting. The OH stretching band for H₂O remains essentially unchanged in all calculations and experimental spectra, and thus will not be discussed.

3.4 Predicted spectra for different particle types

3.4.1 Effect of particle size

We have considered a variety of particle sizes in view of the uncertainty of CO₂ cloud aerosol sizes on Mars. In all cases, the particle size refers to the width of particles (e.g. edge length of a cube) and is illustrated in many of the figures for clarity. The effect of particle size is examined for both pure CO₂ particles and H₂O-CO₂ core-shell particles. In this section, we focus only on particles with the same dimensions in all directions (e.g. cubes). Elongated particles will be considered in Section 3.4.2 when discussing shape effects.

3.4.1.1 Pure CO₂ particles

Calculated spectra for pure CO₂ particles ranging in size from 1 nm to 1 μ m are displayed in Figure 3.2. All spectra are for truncated cubes and the dimensions of each are indicated within the figure. The spectra for particles < 10 nm were calculated with the exciton model, while those for particles > 10 nm were calculated using DDA. For the smallest particles, there are dramatic changes in the profiles of the ν_3 band as a function of particle size. This is a result of the particle dimension being smaller than or similar to the effective range of dipole-coupling,^{3,78} an effect that cannot be reproduced by classical models, such as DDA. Particles in the range of 10 to 100 nm are larger than the effective range of dipole-coupling and spectra are no longer highly dependent on particle size.

Thus, no differences are seen in the spectrum of the 10 nm particle compared with the 50 nm and 100 nm particles. Above 100 nm, the particle size approaches the wavelength of light, and elastic light scattering becomes important (for example, evident from a sloping baseline³). In the spectra for particles ≥ 500 nm, an additional broad shoulder at 2340 cm^{-1} becomes visible due to the excitation of the lowest transverse electric mode of the particle and for increasingly larger particles also due to higher normal modes of the particle.² The intensity of this shoulder increases as the particle size increases. The spectra of even larger particles (see Figure 3.3) are dominated by scattering features such as the sloping baseline and the dispersion shape of the absorption peak.

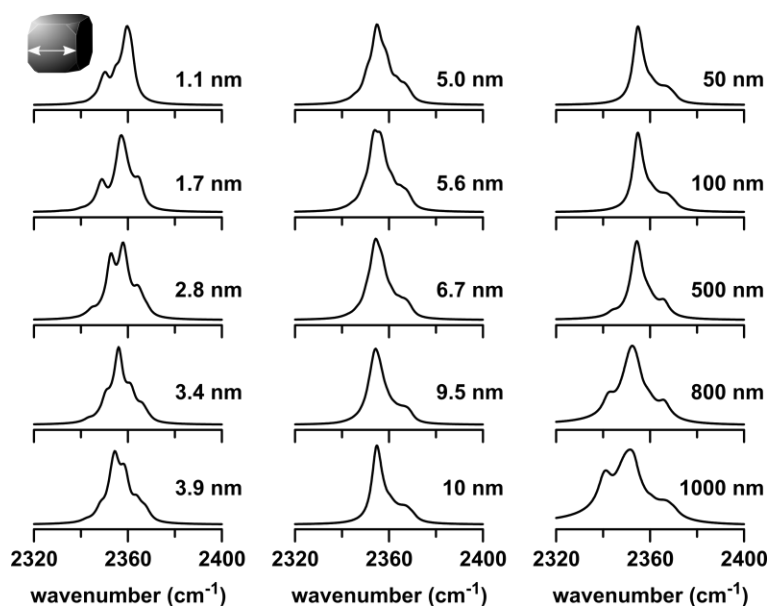


Figure 3.2: Calculated IR extinction spectra for pure CO_2 particles of different size. All particles are truncated cubes and the particle size (as indicated by the arrow) is given for each spectrum. The ordinates are the extinctions in arbitrary units.

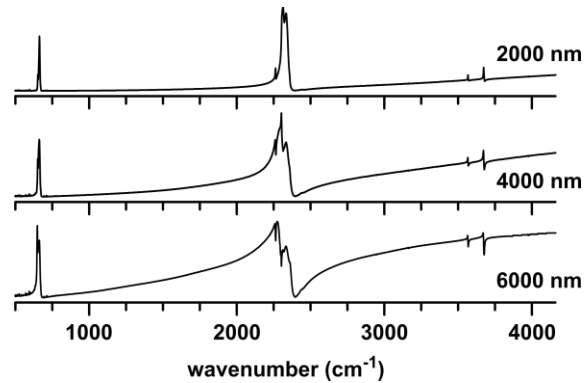


Figure 3.3: Calculated IR extinction spectra for pure CO₂ particles with sizes above 1000 nm (see Figure 3.2 for sizes below 1000 nm). Note the different wavenumber scale compared to Figure 3.2. The spectra show pronounced scattering features such as the sloping baseline and the dispersion shape of the absorption peaks. The ordinates are the extinctions in arbitrary units.

Although it is currently not clear if nanometer-sized particles below 6 nm are relevant to the Martian clouds, we have added corresponding simulations for completeness. If they are relevant, IR band shapes might be used to estimate the size of such small particles with a precision of 1-2 nm based on the strong correlation between band structure and particle size. However, this structure blurs for a distribution of sizes and the information on the size distribution tends to be lost.²⁴ In the size range between 6-100 nm, accurate sizing with nanometer precision based purely on IR extinction spectra would not be possible, even for monodisperse particles. In this regime, the band profile is size-independent (in contrast to particles < 6 nm and > 100 nm). Hence, IR spectra would only allow one to assign the size to lie within this broad regime (and since IR band profiles in the 6-100 nm size range are size-independent, this is an ideal region for us to probe the effect of particle shape only, as detailed in Section 3.4.2). Furthermore, typical features from elastic scattering (sloping baselines) and the presence of shoulders, such as the one at 2340 cm⁻¹, could be

used to assign particle size as being greater than 100 nm. The amount of scattering in IR spectra typically provides a reasonable guess of the particle size distribution for sizes above 100 nm.³

3.4.1.2 H₂O-CO₂ core-shell particles

We also considered the effect of particle size and core/shell ratio for H₂O-CO₂ core-shell particles. Spectra for 100 and 1000 nm core-shell particles (truncated cubes) are contrasted in Figure 3.4. The general trends with increasing particle size are similar to those described above for pure CO₂ particles. For 1000 nm core-shell particles, a shoulder at 2340 cm⁻¹ is present, which is not yet seen for any of the 100 nm core-shell particles. Similar calculations were performed for 10 nm particles; as expected, spectra are qualitatively the same as those for 100 nm particles and are not shown. For core-shell particles, the CO₂ ν_3 band splits into the characteristic doublet of a shell architecture.^{3,10} A detailed explanation for this splitting is provided in a recent publication from our group.¹²³ The effect of CO₂ shell thickness (indicated for each spectrum) is also included in Figure 3.4. As the shell thickness increases, the separation between the two maxima decreases and the spectrum approaches that of the pure CO₂ particle (bottom traces). The separation between the two maxima depends on the core-to-shell ratio and not on the overall shell thickness. This can be seen in Figure 3.4 (e.g. 100 nm particle with $s = 12$ nm versus 1000 nm particle with $s = 120$ nm).

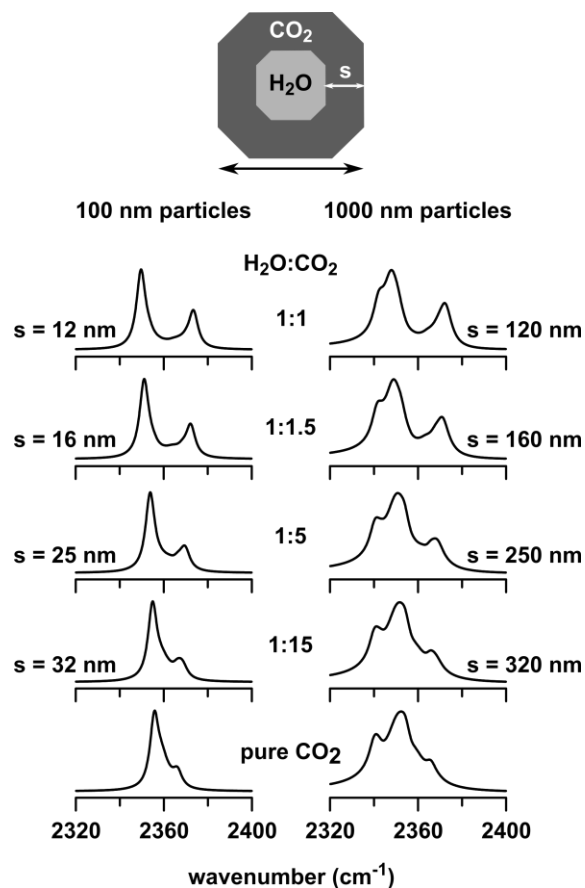


Figure 3.4: Calculated IR extinction spectra for 100 nm and 1000 nm (particle width, as indicated by arrow) H₂O-CO₂ core-shell truncated cubic particles. The thickness of the CO₂ shell (*s*) is indicated for each spectrum along with the number ratio of H₂O to CO₂ in each particle (ratio of the number of molecules calculated from the volume of the core and shell and the densities of H₂O and CO₂). The ordinates are the extinctions in arbitrary units.

The presence of core-shell particles is clearly recognizable in the spectra by the doublet structure which can be used to assign this type of architecture. The assignment of particle size has been discussed for pure CO₂ particles and can be transferred to core-shell particles. Since the separation between the two peaks of the doublet structure is dependent on the core-to-shell ratio, it could be

used to determine the ratio of H₂O to CO₂ in the particles or the approximate shell thickness if the total particle size is known.

3.4.2 Effect of particle shape

To examine the effect of shape alone, excluding other phenomenon, particles within the size range of 10-100 nm must be considered.^{3,10} In this range, the particles size does not influence the IR band profiles (refer to Figure 3.2) and thus will not interfere with shape effects.

The shape of CO₂ cloud particles on Mars is not currently known, although cubic and bipyramidal morphologies are likely.^{110,120} Previous work in our group has found that IR spectra of CO₂ particles formed in our cooling cell are a close match to calculated spectra for truncated cubes.^{24,123} In contrast, laboratory experiments involving deposition of CO₂ onto a bulk CO₂ ice surface¹²¹ or cold specimen substrate¹²² have resulted in the formation of mainly bipyramidal particles. Therefore, for this work, our main focus is on truncated cubes and bipyramids as possible particle morphologies.

3.4.2.1 Pure CO₂ particles

The effect of particle shape on the ν_3 band for pure CO₂ particles is shown in Figure 3.5. Spectra were calculated for several particle morphologies: spheres, bipyramids, truncated cubes, cubes, and various elongated particles. All particles considered in Figure 3.5 have similar volumes and particle dimensions are all within the 10-100 nm range. These calculations show the important relationship between particle shape and corresponding band profile. The spherical particle is characterized by a broad, unstructured, and symmetric band. However, since spherical CO₂ particles are unlikely (pure CO₂ particles are crystalline), this morphology has not been considered

further. The band shape for the bipyramidal particle is similar to that of the sphere, except that the band is less symmetric, with a slight shoulder near 2365 cm^{-1} . The truncated cube and cube both have very similar spectra, each with a clear shoulder present at 2365 cm^{-1} . Since all the aforementioned particles have similar axis ratios, similar, but non-identical, band profiles are found. The band profile for elongated particles, however, is pronouncedly different.¹² Calculated spectra for elongated particles with axis ratios of $1\times 1\times 1.5$, $1\times 1\times 2$, $1\times 1\times 4$, and $1\times 1\times 7$ are also shown in Figure 3.5. As the particles become more elongated, an additional maximum becomes more pronounced and increasingly red-shifted in spectra. The origin of this maximum is due to the elongated nature of these particles.¹² This feature is potentially useful to distinguish between elongated CO_2 particles and those with similar axis ratios. Care must be taken not to confuse the peak associated with particle elongation with the shoulder at 2340 cm^{-1} that is prominent for particles $\geq 500\text{ nm}$. In the case of the latter, the effects of elastic scattering would also be visible in spectra.³

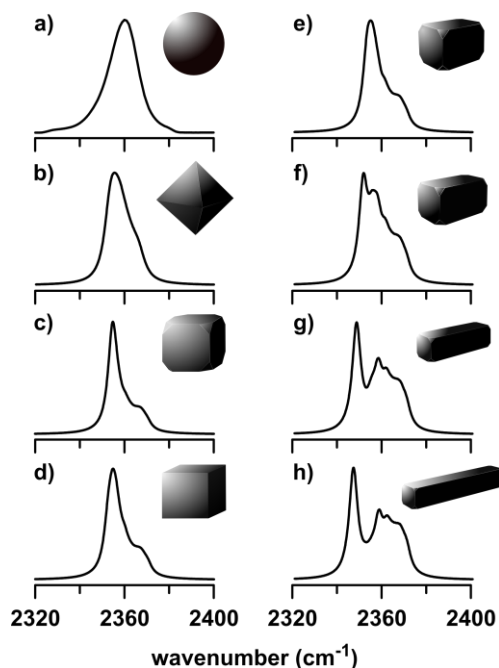


Figure 3.5: Calculated IR extinction spectra for pure CO₂ particles of different shape, each with approximately the same volume. Particle dimensions are all within 10-100 nm. Spectra were calculate for a) a sphere, b) a bipyramid, c) a truncated cube, d) a cube, and e-h) elongated particles with axis ratios e) 1 × 1 × 1.5, f) 1 × 1 × 2, g) 1 × 1 × 4, and h) 1 × 1 × 7. The ordinates are the extinctions in arbitrary units.

3.4.2.2 H₂O-CO₂ core-shell particles

We confine our analysis of shape effects for core-shell particles to bipyramids and truncated cubes. Calculated spectra of 100 nm core-shell particles for each of these morphologies are shown in Figure 3.6. Spectra are presented in a manner analogous to Figure 3.4—the thickness of the CO₂ shell is indicated for each spectrum, as is the molecular ratio of H₂O to CO₂. For both particle morphologies, the predominant feature in the spectra is the splitting of the ν_3 band. The size effects for truncated cubic core-shell particles (discussed in Section 3.4.1.2) also apply to the bipyramidal

core-shell particles. Since the spectra for cubic and bipyramidal core-shell particles are quite similar, assessment of particle shape is difficult for the core-shell architectures.

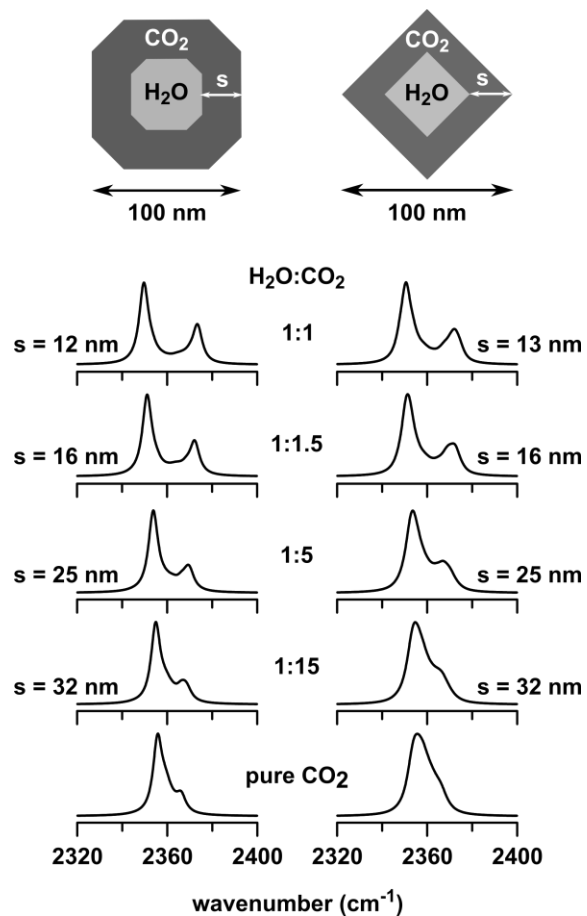


Figure 3.6: Calculated IR extinction spectra for 100 nm truncated cubic and bipyramidal H₂O-CO₂ core-shell particles. The thickness of the CO₂ shell is indicated for each spectrum along with the ratio of H₂O to CO₂ (as described for Figure 3.4). The ordinates are the extinctions in arbitrary units.

3.4.3 Effect of mixing

There are many studies of H₂O/CO₂ thin films that consider molecular mixing of H₂O and CO₂ with respect to sample preparation, temperature changes, and water ice phase (amorphous vs. crystalline).¹²⁷⁻¹³⁸ However, most studies are not performed under Martian conditions, so it is difficult to comment on whether mixing could occur for CO₂ nucleation onto H₂O in the Martian atmosphere. Here, we consider the effect that molecular mixing between H₂O and CO₂ could have on the spectra of CO₂ cloud particles. We consider the extent of molecular mixing with respect to both the thickness of the mixed interface layer and the degree of mixing (ratio of H₂O to CO₂ in the interface layer) for H₂O-CO₂ core-shell particles. Since only minimal differences exist in the spectra of truncated cubic vs. bipyramidal core-shell particles (refer to Figure 3.6), we focus only on truncated cubic core-shell particles in this section.

Calculated spectra for particles with a H₂O core, a molecularly mixed H₂O/CO₂ interface layer (m), and a CO₂ shell (s) are shown in Figure 3.7. The size of the H₂O core is the same for each particle (3.1 nm width), as is the total particle size (7.8 nm width). For each of the particles, the ratio of H₂O to CO₂ in the interface layer was varied, and is indicated for each spectrum. The spectra in the left column were calculated for a mixed interface layer that is thick compared with the CO₂ shell ($m > s$). Spectra in the right column were calculated for a particle where the mixed interface layer and the CO₂ shell are of similar thickness ($m \approx s$). For $m > s$, the ν_3 band is broadened and the shape of the band is highly dependent on the H₂O:CO₂ mixing ratio. However, for the particle with $m \approx s$, the ν_3 band takes on the familiar shape of the CO₂ shell structure, with only minimal dependence on the mixing ratio in the interface layer. Similar results as for $m \approx s$ are found for particles with $m < s$. The same calculations were repeated for other H₂O core sizes with the total particle size remaining

at 7.8 nm (not shown) as well as for different total particle sizes (not shown). The dependence of the ν_3 band on the $m:s$ ratio is analogous to that shown in Figure 3.7. Thus, the effect of mixing between H₂O and CO₂ would only be apparent in the spectra of particles with $m > s$. In such cases, the bands no longer have the splitting expected for core-shell particles (Figure 3.4 and Figure 3.6) and are highly dependent on the degree of mixing (H₂O:CO₂). For all particles with $m \leq s$, the band resembles that for a CO₂ shell with only minimal dependence on the H₂O:CO₂ mixing ratio.

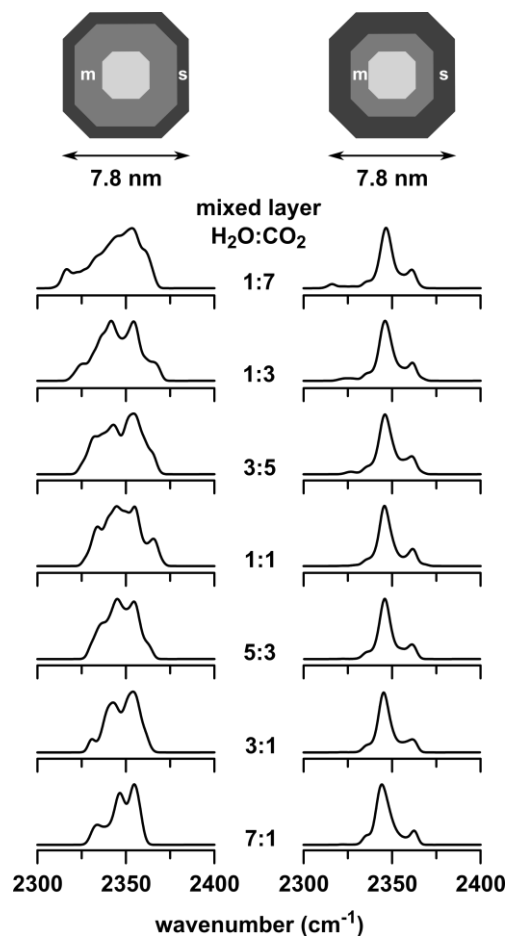


Figure 3.7: Calculated IR extinction spectra for 7.8 nm H₂O-CO₂ core-shell particles with a mixed interface layer. Spectra on the left have a very thin pure CO₂ shell, while the thickness of the CO₂ shell for spectra on the right is similar to the thickness of the mixed interface layer. The H₂O:CO₂ mixing ratio of the intermediate layer is indicated for each spectrum. The ordinates are the extinctions in arbitrary units.

3.4.4 Effect of architecture

If CO₂ nucleates onto H₂O particles, CO₂ might form patches on H₂O rather than a complete shell (see sketch in Figure 3.8(c)). Such architectures were suggested in previous studies of H₂O/CO₂ aerosols.^{66,70} In this case, we would expect the CO₂ ν₃ band to resemble more closely the spectrum

of an ensemble of pure CO₂ particles with different sizes and shapes (corresponding to a variation in the size and shape of the CO₂ patches) than that of a shell structure. Figure 3.8(c) shows a simulated spectrum for partial engulfing of H₂O by CO₂, which confirms this expectation. This spectrum was obtained by averaging over the spectra of a distribution of CO₂ patches with different sizes and shapes. A comparison with the spectrum of a pure CO₂ particle (truncated cube) and a H₂O-CO₂ core-shell particle is also displayed in Figure 3.8. The distribution in the size and shape of the CO₂ patches leads to a broadening of the ν_3 band and a loss of distinct structures in the band profile. The broader the distribution of size and shape of the patches, the more pronounced is the broadening and loss of structure.

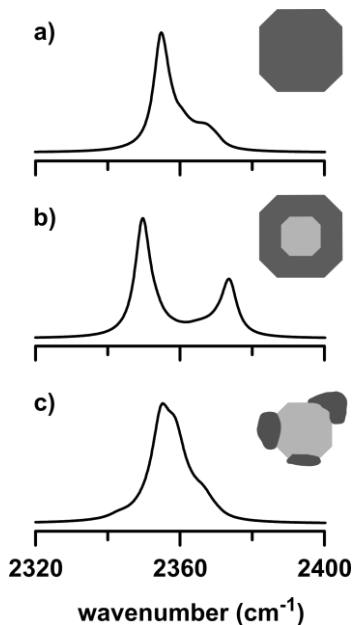


Figure 3.8: Calculated IR extinction spectra for different CO₂ architectures. a) Pure CO₂, b) complete CO₂ shell surrounding a H₂O core, and c) partial engulfing of H₂O by CO₂ (average for an ensemble of CO₂ patch shapes and sizes). The ordinates are the extinctions in arbitrary units.

3.4.5 Effect of core material

So far, we have focused on H₂O as the CO₂ particle core. However, dust is also suggested as a possible CO₂ cloud particle nucleus.^{80,82,84,125,146} Here, we consider the effect that the core material could have on CO₂ particle spectra. The nucleating abilities of different Martian dust particles were discussed by Gooding.¹²⁵ However, the availability of RI data in the mid-IR region for possible dust materials is limited and restricts our choices for dust cores for use in calculations. We chose FeO and Fe₃O₄ as possible dust core materials to illustrate the effect that these materials may have on spectra.

Spectra were calculated for core-shell particles, all with the same particle dimensions and core-to-shell ratios, containing either H₂O, FeO, or Fe₃O₄ as the core material. The difference in the CO₂ ν_3 band for each of the core materials is shown in Figure 3.9. The CO₂ ν_3 band of a CO₂ particle with a H₂O core is shown in Figure 3.9(a). Figure 3.9(b) shows the ν_3 band of a FeO-CO₂ core-shell particle. It is split into two bands as would be expected for the CO₂ shell architecture. While their positions are approximately the same as for the H₂O-CO₂ core-shell particles, the relative intensities of each peak are reversed. The spectrum of the Fe₃O₄-CO₂ core-shell particle is shown in Figure 3.9(c). The splitting of the ν_3 band is less pronounced, but the overall width of the band is similar to that in the FeO core spectrum. The changes in the CO₂ spectrum for each of the different core materials are a result of the different RI for each of these compounds. In this region of the spectrum, the values for the real part (n) of the complex RI for H₂O, FeO, and Fe₃O₄ are approximately 1.4, 2.6, and 3.8, respectively. Figure 3.9 demonstrates that the core material has a pronounced effect on the spectral signature of CO₂. In case a certain class of core materials dominates the CO₂ Mars clouds, IR extinction spectra should allow one to identify this class.

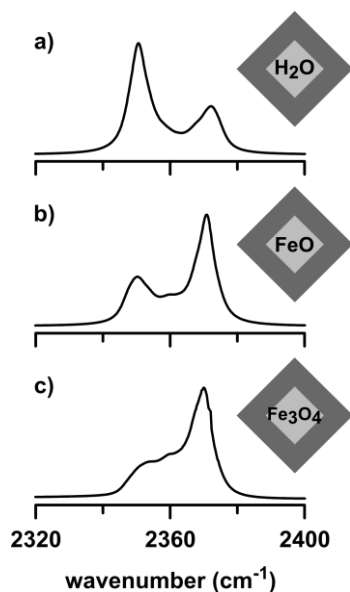


Figure 3.9: Calculated IR extinction spectra for core-shell particles (bipyramids) consisting of a CO₂ shell and different core materials: a) H₂O core, b) FeO core, and c) Fe₃O₄ core. For all particles, the ratio of the core width to the shell thickness is 1:0.13. The ordinates are the extinctions in arbitrary units.

3.5 Experimental attempts to form core-shell particles

The formation of core-shell aerosols in the cooling cell is by no means trivial and requires a specific combination of sample pressures, bath gas pressure, injection times, and injection delays to properly coat the core particles with the shell component. We have previously reported the formation of N₂O-CO₂ core-shell particles in our cooling cell at 78 K.¹⁶ Since the N₂O/CO₂ system is known to form core-shell particles under specific conditions, we began our attempts to form H₂O-CO₂ core-shell particles with the experimental conditions that led to core-shell formation for this system. To our knowledge, there exist no previous attempts to form H₂O-CO₂ core-shell aerosols in the lab.

3.5.1 The N₂O-CO₂ system

Figure 3.10(a) shows an experimental spectrum of pure CO₂ aerosols. It is the spectrum of an ensemble of particles with different shapes; i.e. mainly cubic (main peak) with some contributions from various elongated morphologies (side peaks).^{3,10,12,14,16,24,78,123} Previous measurements of pure CO₂ aerosols in the cooling cell have shown changes in the spectra with time as a result of particle elongation (e.g. see Bonnamy et al.,²⁴ Figure 2(c)). The time scale for this process depends on the exact experimental conditions (e.g. cell pressure, sample concentration) and in the current experiments, some elongation has already occurred by the time we recorded this spectrum. The simultaneous injection of N₂O and CO₂ leads to the formation of molecularly (statistically) mixed particles,¹⁶ which are characterized by the broad, unstructured band shown in Figure 3.10(b). Sequential injection of N₂O followed by CO₂, shown in Figure 3.10(c), leads to the CO₂ ν_3 band shape resembling that for the shell architecture, i.e. N₂O-CO₂ core-shell particles.¹⁶ A calculated N₂O-CO₂ core-shell spectrum is provided in Figure 3.10(d). The ratio of N₂O:CO₂ used for the calculation is the same as that in the experimental spectrum (determined from integration of bands) and is equal to 1:1.2. There is excellent agreement between the splitting of the ν_3 band in both the experimental spectrum in trace (c) and the calculated spectrum in trace (d), which clearly proves the formation of N₂O-CO₂ core-shell particles.

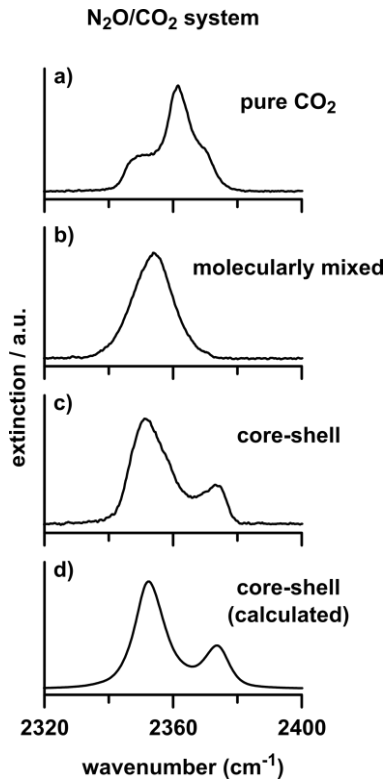


Figure 3.10: Experimental IR extinction spectra of a) pure CO₂ aerosols, b) molecularly mixed N₂O/CO₂ aerosols formed by simultaneous injection of CO₂ and N₂O, and c) N₂O-CO₂ core-shell particles formed by sequential injection of N₂O followed by CO₂. Calculated spectrum for d) N₂O-CO₂ core-shell particle (same N₂O:CO₂ ratio as in panel (c)). The calculated spectrum was convoluted with an 8 cm⁻¹ Voigt profile.

3.5.2 The H₂O-CO₂ system

The experimental conditions used to form N₂O-CO₂ core-shell particles were applied to the H₂O/CO₂ system with the goal of forming H₂O-CO₂ core-shell particles. It is important to note here that we are not able to replicate conditions in the Martian atmosphere in the cooling cell. Our cell pressure of 500 mbar is much higher than even the surface pressure on Mars and 78 K is colder than any temperatures recorded on Mars. These experiments are relevant to whether H₂O-CO₂ core-shell

particles form under the conditions in our cell, but the results cannot be used to directly confirm or refute the possibility of their formation on Mars.

Experimental spectra of pure CO₂ aerosols, aerosols formed by simultaneous injection of H₂O and CO₂, and those formed by sequential injection of H₂O followed by CO₂ are displayed in Figure 3.11(a), (b), and (c), respectively. It is interesting to note that unlike for the N₂O/CO₂ system (Figure 3.10(b) and (c), respectively), there is no difference in the band profile of the ν_3 band for simultaneous injection (Figure 3.11(b)) versus sequential injection (Figure 3.11(c)) of the two gases. While the CO₂ ν_3 band does take on a different structure compared with the pure CO₂ aerosols (trace (a)) in the presence of H₂O (traces (b) and (c)), neither spectrum has the characteristic splitting for a CO₂ shell architecture. We also tried additional measurements with the H₂O/CO₂ system under a variety of other pressure and injection conditions (not shown). None of these other measurements showed the splitting of the CO₂ ν_3 band expected for a shell architecture. The architecture of the H₂O/CO₂ particles that are formed in the cooling cell is independent of the formation conditions (simultaneous vs. sequential) and is not that of a complete CO₂ shell. The architecture could be that of partial engulfing of H₂O by CO₂ patches of various sizes and shapes as previously suggested.^{66,70} The comparison of our experimental H₂O/CO₂ spectra with the calculated spectrum for an ensemble of patch architectures (refer to Figure 3.8(c)) shows indeed a similar broad and unstructured ν_3 band. Thus, the formation of H₂O particles partially engulfed by CO₂ seems a reasonable explanation for the experimental observations in our cooling cell. Furthermore, it clearly shows that even under optimized conditions, perfect H₂O-CO₂ core-shell particles cannot be formed in our cooling cell.

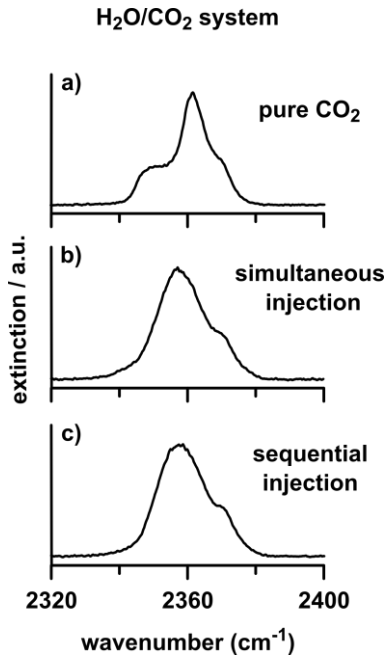


Figure 3.11: Experimental IR extinction spectra of a) pure CO₂ aerosols, b) simultaneous injection of CO₂ and H₂O, and c) sequential injection of H₂O followed by CO₂. We think that particles with an H₂O core that is partially engulfed by CO₂ patches of various shapes and sizes provide a reasonable explanation for the both the simultaneous and sequential injections.

3.6 Summary

Based on the calculated extinction spectra of various types of pure and mixed CO₂ aerosol particles, it is possible to make the following general statements concerning the identification of CO₂ clouds on Mars through mid-IR extinction spectra. Should the Martian CO₂ cloud particles cover a wide range of different particle properties, one expects broad and unstructured bands in the regions of the antisymmetric stretching vibration and the bending vibration of CO₂. In this case, specific statements on the distributions of shape, architecture, mixing, etc. would be questionable, but statements about approximate particle size and composition would still be possible. If particles

with sizes above ~ 100 nm are present, the spectra will exhibit increasingly slanted baselines towards higher wavenumbers. An approximate size distribution can be obtained in this case from the modelling of the spectra (in particular of the slanted baseline^{3,22}). In the absence of slanted baselines in the mid-IR region, one can at least say that the particle sizes must be smaller than about 100 nm. The composition of the clouds can of course be estimated from the ratio of CO₂, H₂O, and possibly from mineral dust bands. However, no statements are possible on the composition of the particles themselves.

If the conditions in the Martian atmosphere favour the formation of particles with more uniform properties, the IR extinction spectra provide at least a guide to narrow down the properties of CO₂ cloud particles and help to evaluate results from complementary data. In this case, the following more specific statements on shape, composition, architecture, and mixing could be possible.

Regarding the particle size, the same statements hold as above. Particle shapes can be characterized by their aspect ratio. With near unit axis ratios, such as cubes, the antisymmetric stretching band of CO₂ has a rather narrow, slightly structured profile with a pronounced maximum. For particles with different axis ratios, such as elongated particles, this band profile becomes broader, is more structured, and can show several components. In this way the two classes of particle shapes could be differentiated. Finally, the IR spectra could help identify special particle architectures. Core-shell particles consisting of an H₂O or a mineral dust core and a CO₂ shell can be distinguished from other architectures by the characteristic splitting of the antisymmetric stretching band of CO₂ into two components. The pronounced dependence of the intensity ratio of the two components on the core material provides characteristic information on the latter. For the H₂O-CO₂ core-shell particles (or particles that consist of a H₂O coated mineral dust core and a CO₂ shell), a molecularly mixed interface layer might be conceivable. If the

thickness of this interface layer is larger than the thickness of the pure CO₂ shell, the antisymmetric stretching band becomes increasingly broader with increasing thickness of the interface. If the thickness of this interface layer is smaller than the thickness of the pure CO₂ shell, the presence of this interface layer is not noticeable in the spectra.

Our present experimental and modelling results, together with previous experimental observations^{66,70} of H₂O/CO₂ particle formation in collisional cooling cells hint at another variant of particle architecture. Instead of perfect H₂O-CO₂ core-shell particles, H₂O particles are engulfed by patches of CO₂ with different shapes and sizes. The antisymmetric CO₂ stretching band of such particles is broad and unstructured and could probably not be distinguished from particles with a thick molecularly mixed H₂O/CO₂ interface or from the case where Martian particles simply cover a broad range of different particle properties. However, it is important to note that our experiments are not performed under Martian conditions and thus might not be representative of the Martian CO₂ cloud particles. Therefore, our laboratory experiments do not rule out the formation of core-shell particles in the atmosphere of Mars.

Chapter 4: Infrared spectroscopy of solid mixed ammonia-water and acetylene-water aerosol particles[†]

This chapter focuses on ensemble measurements for mixed water aerosol particles formed in a bath gas cooling cell. The spectra for ammonia-water and acetylene-water aerosol particles are compared to calculated spectra (using the vibrational exciton model) and thin film measurements to confirm assignments of particle properties.

4.1 Introduction

There is considerable interest in the composition of the atmospheres of planets and moons in our solar system with mixed aerosols as important components. The infrared (IR) spectra of aerosol particles can be sensitive to intrinsic particle properties, such as particle size, shape, architecture, and structure.^{3,123,147} This makes IR spectroscopy a useful method to study the properties of aerosol

[†] This chapter is accepted for publication: M. Isenor and R. Signorell, *Mol. Phys.*, 2014, DOI: 10.1080/00268976.2014.981232.

particles, for example, by monitoring temporal changes of band shapes, which can arise from changes in the particle morphology or internal structure (e.g. mixing and demixing in multi-component particles).

In the current work, we present time-dependent Fourier transform infrared (FTIR) extinction (absorption + scattering) spectra for solid ammonia-water and acetylene-water aerosol particles formed in a bath gas cooling cell at 78 K. Both of these types of mixed particles may be important throughout our solar system. Recent analysis of near-IR spectra collected during Saturn's Great Storm of 2010-2011 has found evidence of multi component aerosol particles partially composed of ammonia and water ice.⁸⁶ Both water ice and ammonia ice clouds exist in the atmospheres of Jupiter, Uranus, and Neptune.^{87,88} Additionally, the analysis of the water plumes on Enceladus has found small amounts of ammonia and acetylene.^{89,90}

Water ice is a major component of many astrophysical ices. As a result, thin films of a variety of water ice mixtures have been widely examined in the IR,^{148,149} including ammonia-water^{61,148-162} and acetylene-water^{149,163-165} thin films. The IR spectra of aerosol particles may vary greatly from those of the bulk mixtures due to the size and shape of particles^{2,3,123,147} and these differences must be considered when analyzing the spectra of aerosol particles. As well, experiments in the particle phase are required to determine possible particle architectures (e.g. core-shell particles) as these properties cannot be determined from thin film measurements.

We have previously studied other binary mixed aerosol particles containing water, ammonia, or acetylene that may be relevant for astrophysical studies, such as acetylene-carbon dioxide particles,^{32,33} ammonia-acetylene particles,³⁴ and water-carbon dioxide particles¹⁶⁶ (refer to Chapter 3 for discussion of the water-carbon dioxide particles). While all these experiments were

performed under similar conditions, each of the binary mixed aerosol systems was found to have different shapes, architectures, and internal structures. These different particle properties can have a dramatic effect on the band shapes in the IR spectra. Acetylene and carbon dioxide were found to immediately form metastable co-crystalline aerosol particles that decomposed to pure acetylene and pure carbon dioxide with time.^{32,33} In contrast, acetylene formed a co-crystal with ammonia via solid state diffusion after the initial formation of core-shell particles.³⁴ The study of water-carbon dioxide aerosol particles showed no evidence of molecular mixing. A plausible structure for water-carbon dioxide particles is that of solid water particles partially engulfed by patches of solid carbon dioxide.¹⁶⁶ These examples demonstrate that the exact architecture and structure for aerosol particles is highly dependent on the types of molecules present and their specific intermolecular interactions.

In the current work, we first present our study of solid ammonia-water aerosol particles (Section 4.3.1) followed by the results for the acetylene-water aerosol particles (Section 4.3.2). We focus the majority of our analysis on the ammonia-water particles since we observe similar results for both ammonia-water and acetylene-water particles. Additionally, there appears to be greater astrophysical interest in ammonia-water mixtures. We compare our particle spectra to literature spectra of thin film mixtures and to calculated extinction spectra using the vibrational exciton model to confirm our interpretations of the IR spectra.

4.2 Methods

4.2.1 Experiments

All experiments were performed in a bath gas cooling cell. A complete description of the experimental setup can be found elsewhere³⁵ and in Section 2.1.1. The cell was cooled to 78 K with liquid nitrogen and filled with 500 mbar of helium. Ammonia-water and acetylene-water aerosol particles were generated by injecting room temperature sample gases (ammonia: 200 or 400 ppm, acetylene: 220 ppm, water: 640-1200 ppm, all in helium; total sample pressure: 2 bar) into the cell by opening two separate magnetic valves. The injection of dilute room temperature gases into the cold cell leads to supersaturation and aerosol particle formation. Valve opening times were typically 900 ms. We use the term ‘premixed injection’ if the two gases are first premixed and then injected into the cell through a single valve. Both valves are used in order to inject the two different sample gases. To inject one gas after the other, a delay can be introduced between the opening times of each valve. The delay time between opening the first valve and opening the second valve was typically 1000 ms. We refer to this type of injection as ‘sequential injection’ throughout the paper. If both valves are opened at the same time (i.e. no delay), we use the phrase ‘simultaneous injection’. (Note that in the present study, we find the same results for both the premixed and simultaneous injection methods.)

A Bruker IFS66v/S rapid-scan FTIR spectrometer (~ 380 ms per scan at 0.5 cm^{-1} spectral resolution) was used to collect spectra of the aerosol particles suspended in the cell for a time period of 30-120 minutes after injection. Immediately after injection, we collect spectra that consist of only a single scan to achieve the best time resolution for spectra. As the measurement

time progresses and particles begin to move out of the path of the IR beam, we average multiple scans to improve the signal-to-noise ratio in the spectra.

4.2.2 Vibrational exciton calculations

The vibrational exciton model was used to calculate band shapes in IR extinction spectra for the ammonia and acetylene aerosol particles. A detailed description of this model can be found elsewhere^{3,10,11,14,78} and in Section 2.2.1. Briefly, it is a quantum mechanical model to calculate the IR extinction spectra for molecular nanoparticles. It has been previously shown that for vibrations with a transition dipole moment greater than 0.1 D, the dominant contribution to the IR band shape is resonant dipole coupling (exciton coupling).^{3,10-12,14-17,19,20,24,78,79} This coupling lifts the degeneracy of the uncoupled molecular vibrational states and leads to vibrational eigenfunctions that are delocalized over the particle. The result is highly structured band shapes that depend strongly on intrinsic particle properties (size, shape, architecture, and composition). In the exciton model, the vibrational Hamiltonian is essentially reduced to this dominant contribution which reduces the computational cost required to calculate spectra and allows for the calculation of spectra for particles containing tens of thousands of molecules.

The input parameters required for the calculations are the transition dipole moment, the molecular vibrational frequency, and the molecular structure. Calculations were performed for pure crystalline (cubic structure) and amorphous ammonia particles for the ammonia ν_2 band. The amorphous structure was used as a proxy for the molecularly mixed water-ammonia particles since in both cases, the ammonia molecules are disordered within the particles. The vibrational frequency for the ammonia ν_2 band was set to 1060 cm^{-1} for the pure crystalline particles and the transition dipole moment was set to 0.21 D.¹⁵ The vibrational frequency for the amorphous

ammonia particles was shifted by 40 cm^{-1} to 1100 cm^{-1} corresponding to the shift calculated for the ammonia monomer and the ammonia-water 1:1 complex.¹⁶⁷ Octahedral particles were chosen for the crystalline ammonia calculations based on the experimental observations of ammonia particle morphology by Pope et al.¹⁶⁸ Spherical particles were used for the amorphous ammonia particles since this is the most likely shape for an amorphous structure. It is noteworthy that spectra of amorphous particles are largely insensitive to the particle shape.

The calculated acetylene spectra were taken from previous work in our group.²¹ The calculations performed for the acetylene ν_5 band (transition dipole = 0.28 D) for pure polycrystalline particles were derived from an orthorhombic crystal structure. (Note that we found pure acetylene particles to be stable in a polycrystalline form rather than in the crystalline form.) The amorphous acetylene structure taken from the work of Preston et al.²¹ is used to approximate the mixed acetylene-water particles. Non-crystalline particles are most likely to be spherical, thus spherical particles were used in the calculations for both the polycrystalline and the amorphous acetylene particles. The input frequency for the pure acetylene particle was 772 cm^{-1} . This value was shifted to 793 cm^{-1} for the amorphous particle calculation based on the observed experimental frequency for the 1:1 acetylene-water complex.¹⁶⁹

4.3 Results

The size of aerosol particles formed in the cooling cell depends on the exact experimental conditions (e.g. temperature and pressure of the bath gas in the cell and the concentration of sample gases injected into the cell).^{12,14,15,17,22} The size of aerosol particles can be estimated from their IR spectra and a detailed summary of the effects of particle size on IR spectra can be found in the paper by Sigurbjörnsson et al.³ We estimate that the particles studied in this work are on the

order of 10 to 100 nm in diameter. The lack of elastic scattering in any of our spectra (which would be visible as a sloping baseline and dispersive band shapes, e.g. Figures 2 & 3 in Isenor et al.,¹⁶⁶ refer to Figure 3.2 and Figure 3.3 in this thesis) provides an upper limit of 100 nm for the particle diameters. Below 10 nm, the band profiles are highly dependent on the particle size, while between 10 and 100 nm, the spectra are essentially independent of the size.³ We have injected different sample gas concentrations into the cell (while keeping the bath gas temperature and pressure constant) without any marked differences in the band profiles in spectra. Thus, we estimate a lower limit to the particle diameter in general of 10 nm.

4.3.1 Ammonia-water aerosol particles

4.3.1.1 Overview of aerosol particle IR spectra

Experimental infrared spectra of pure solid ammonia and water aerosol particles (traces (a) and (b), respectively) and mixed ammonia-water aerosol particles (traces (d) and (e)) are presented in Figure 4.1. This figure provides an overview of the extinction for each type of particles in the mid-IR range at 78 K. A series of spectra were collected over a period of 30 minutes after sample injection. No changes were observed in any of the spectra during this time. Table 4.1 provides a summary of the band positions determined at the band maxima for the pure and mixed ammonia and water particle spectra shown in Figure 4.1.

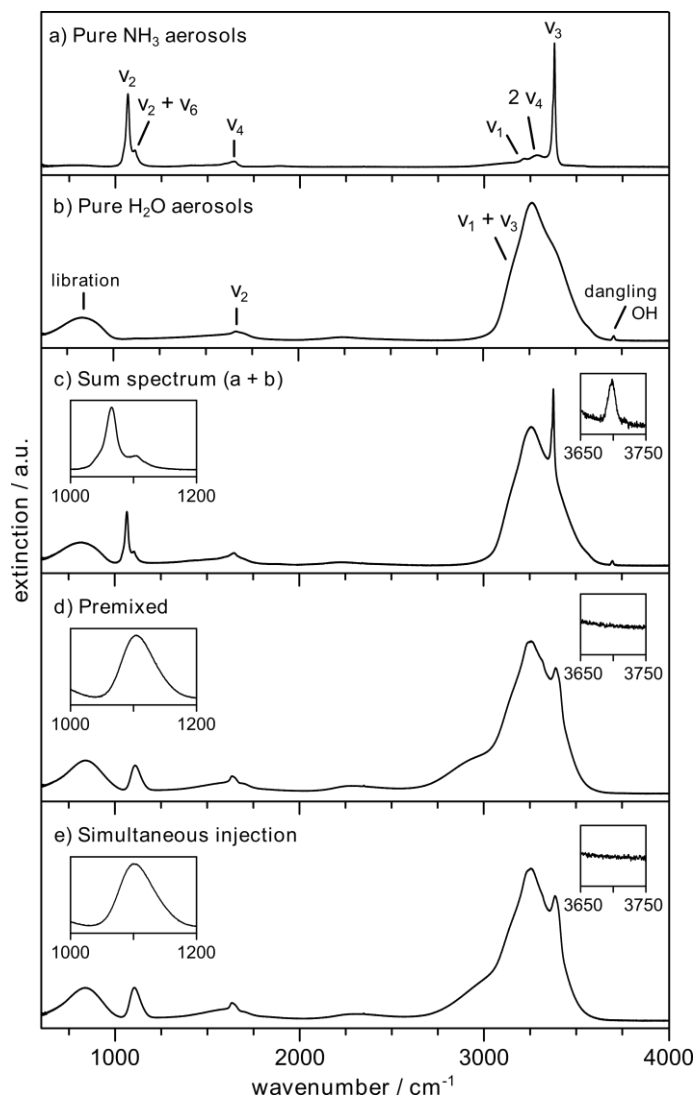


Figure 4.1: Overview infrared aerosol particle spectra for a) pure NH_3 , b) pure H_2O , c) a sum spectrum (addition of spectrum (a) and spectrum (b)) d) particles formed after injection of a premixed $\text{H}_2\text{O}/\text{NH}_3$ sample, and e) particles formed after simultaneous injection of NH_3 and H_2O samples. Insets in (c), (d), and (e) show an expanded view of the ammonia ν_2 band and the dangling-OH stretch region. The ratio of $\text{H}_2\text{O}:\text{NH}_3$ is approximately 2:1 in (c), (d), and (e).

Table 4.1: Infrared band assignments for pure and mixed NH₃ and H₂O aerosol particles formed in the cooling cell (see Figure 4.1).

	Band	Position (cm ⁻¹)	
		Pure	Mixed*
NH ₃	v ₂	1066	1100 [§]
	v ₂ + v ₆	1104	[§]
	v ₄	1642	1631 [†]
	v ₁	3213	[†]
	2 v ₄	3287	[†]
	v ₃	3378	3383 [†]
H ₂ O	libration	814	833
	v ₂	1650	1631 [†]
	v ₁ + v ₃	3257	3253 [†]
	dangling-OH	3698	-

*Taken from spectra recorded after simultaneous injection of the sample gases

[§]NH₃ v₂ and v₂ + v₆ overlap

[†]H₂O and NH₃ overlap in this region

The spectrum of pure ammonia ice aerosol particles is depicted in Figure 4.1(a). Solid ammonia aerosol particles have a cubic structure based on comparison to IR spectra from previous aerosol studies^{15,34} and thin films of crystalline ammonia.¹⁷⁰ We focus the majority of our analysis on the v₂ bending mode at 1066 cm⁻¹, which is often referred to as the ‘umbrella’ motion. This band is sensitive to the size, shape, structure, and architecture of particles.^{15,40} The other bands in the pure ammonia spectrum are the v₄ band at 1642 cm⁻¹ (a bending motion), the v₁ and v₃ stretching modes at 3213 cm⁻¹ and 3378 cm⁻¹, respectively, and the v₂ + v₆ combination band (v₆ is a lattice vibration¹⁷¹). A spectrum of pure water ice particles is shown in trace (b). The shape of the OH stretching band suggests that the water particles are likely amorphous.¹⁷² The broad band from 600-1000 cm⁻¹ is the libration mode (lattice vibration), the v₂ band at 1650 cm⁻¹ is the bending mode, and the broad band from 3000-3600 cm⁻¹ is the region of the v₁ and v₃ stretching modes. The

small peak at 3698 cm^{-1} is referred to as the 'dangling-OH' band. It results from free OH at the surface of the particles not involved in hydrogen bonding.⁵⁶ A sum spectrum of the pure ammonia spectrum (trace (a)) and pure water spectrum (trace (b)) is shown in trace (c). The ratio of $\text{H}_2\text{O}:\text{NH}_3$ is roughly 2:1. The sum spectrum demonstrates which features would be expected for an ensemble that consists of pure ammonia and pure water particles; i.e. with no mixing of the two substances on a molecular level.

Figure 4.1(d) and (e) both show spectra for mixed ammonia-water particles, i.e. with mixing of the two substances on a molecular level. The ratio $\text{H}_2\text{O}:\text{NH}_3$ is approximately 2:1 for both experiments. This ratio was calculated using the integrated band intensities of the spectra along with the band strengths determined at 10 K for thin films of water and ammonia (taken from the work of d'Hendecourt and Allamandola¹⁴⁸). The spectrum in Figure 4.1(d) was recorded immediately after injection of a premixed ammonia/water gas sample (premixed injection) while the spectrum in Figure 4.1(e) was recorded immediately after simultaneous injection of each of the pure gas samples. These two spectra are almost identical. There are, however, pronounced differences between the sum spectrum (trace (c)) and these two mixed spectra. The most notable difference occurs in the region of the ammonia umbrella mode (see insets), which is broadened and its position is shifted from 1066 cm^{-1} to 1100 cm^{-1} for the mixed particles. Other changes in the spectra of the mixed particles include a broadening at the base of the OH stretch region (down to $\sim 2600\text{ cm}^{-1}$), a broadening and shift of the NH stretch band, and the loss of the dangling-OH band (see insets). In the following Sections 4.3.1.2 and 4.3.1.3 we provide evidence that the mixed particles (traces (d) and (e)) are amorphous with ammonia and water mixed on a molecular level.

4.3.1.2 Comparison to thin film spectra

Ammonia and water can form non-stoichiometric molecularly mixed solids or one of the possible hydrate structures: the hemi-hydrate ($2\text{NH}_3\text{-H}_2\text{O}$),¹⁷³ the monohydrate ($\text{NH}_3\text{-H}_2\text{O}$),¹⁷⁴ and the dihydrate ($\text{NH}_3\text{-}2\text{H}_2\text{O}$).¹⁷⁵ The distinction between the non-stoichiometric ices and the hydrates relates to the hydrogen bonding in the solids, which is ordered in the case of the latter.

Co-deposition of ammonia and water gases around 78 K will typically form amorphous mixed films. The hydrates may then be formed by annealing the amorphous films, provided that the film has the appropriate stoichiometry.¹⁵⁰⁻¹⁵³ IR spectra exist for thin films of various ammonia-water mixtures,^{148-150,154,155} as well as for the hemihydrate,^{61,150-152,156-160} the monohydrate,^{150,153,156-158,161,162} and the dihydrate.¹⁵² Several of these references include spectra of deuterated water or deuterated ammonia to avoid the overlap of the ammonia NH stretching region and the water OH stretching region.

In Figure 4.2, we compare the spectra of mixed particles with thin film measurements that have been previously published and made available for download.^{150,176} Figure 4.2(a) and (b) both show our experimental spectra for mixed ammonia-water particles, with $\text{H}_2\text{O}:\text{NH}_3$ ratios of approximately 2:1 and 5:1, respectively. The different ratios were obtained by varying the amount of ammonia injected into the cell while keeping the amount of water constant. The main differences in these two spectra relate to moderate difference in the intensity of the ammonia features. Apart from that, very similar band profiles are observed for both mixing ratios. The infrared spectra in traces (c) to (e) are thin film measurements for a 5:1 mixture, the monohydrate, and the hemihydrate, respectively, from Hudson et al.^{150,176} The spectra were recorded at 90 K for the ammonia-water film and 95 K for the monohydrate and hemihydrate thin films. The broad features above $\sim 2000\text{ cm}^{-1}$ for the thin film spectrum of the 5:1 mixture (trace (c)) may be due to artifacts

inherent to thin film measurements. For this reason, we focus our comparisons to the region between 600 cm^{-1} and 2000 cm^{-1} .

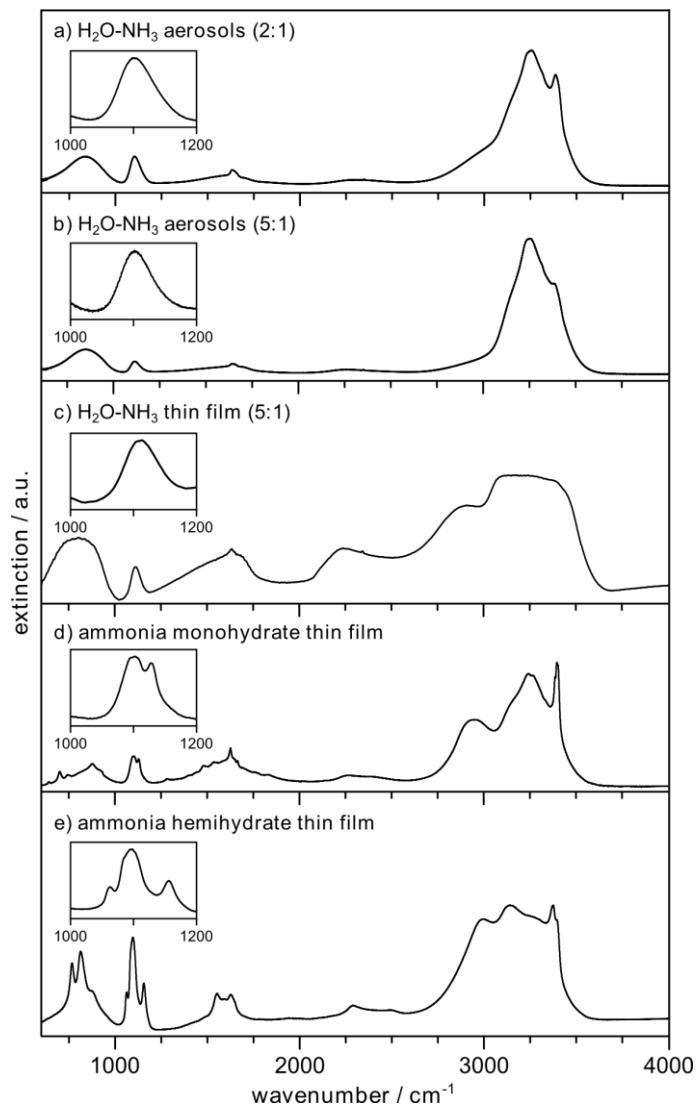


Figure 4.2: Comparison of $\text{NH}_3\text{-H}_2\text{O}$ aerosol particle spectra to thin film spectra. a & b) Molecularly mixed $\text{H}_2\text{O-NH}_3$ particles formed at 78 K after simultaneous injection of the sample gases, c) $\text{H}_2\text{O-NH}_3$ thin film measurement at 90 K, d) monohydrate thin film measurement at 95 K, e) hemihydrate thin film measurement at 95K. Insets show an expanded view of the umbrella region. Thin film measurements were taken from the work of Hudson et al.^{150,176} All spectra are scaled to the same maximum for ease of comparison.

The insets in Figure 4.2 show the region of the ammonia ν_2 band for each spectrum. The features in the particle spectra are quite similar to those for the 5:1 thin film in this region. The spectra of the hydrates, by contrast, are much more structured in the region of the H₂O libration band, the NH₃ umbrella band, and in the region where the ammonia ν_4 and water ν_2 bands overlap. Such strongly structured bands would be expected for the hydrates due to their ordered molecular structure. For molecularly mixed substances without any long range order, however, one expects to observe broad rather featureless bands, such as the bands in traces (a) to (c). While not shown here, our NH₃-H₂O particle spectra also bear a strong resemblance to the 3:1 thin film measurement at 10 K by d'Hendecourt and Allamandola¹⁴⁸ and the 5:1 thin film measurement at 70 K by Knacke et al.¹⁵⁵ These comparisons clearly indicate that the particles consist of ammonia and water molecules that are mixed on a molecular level but do not form hydrates. We would expect the formation of amorphous particles at 78 K based on the formation of amorphous films at similar temperatures. Additionally, we do not anneal the particles, which is the usual procedure for forming crystalline thin films.

4.3.1.3 Comparison to other particle spectra

We are not aware of any previous studies of free ammonia-water aerosol particles, though previously Devlin et al. have examined ammonia-water ice particles collected on a cold window with IR spectroscopy. These results are summarized in two publications. In the first one, they studied the conversion of water ice nanocrystals to the crystalline ammonia monohydrate with saturated pressures of ammonia at 120 K.⁶⁸ In the second study, they focused on NH₃-D₂O systems to avoid overlap between the ammonia and water bands and monitored the conversion of water ice particles to the monodeuterate (T = 115-123 K) and hemideuterate (T = 102-110 K) after exposure to ammonia vapour.⁶¹ For the monohydrate (and monodeuterate) particles, the ammonia ν_2 band

and the OH/OD-stretching bands again have much more structure than what we observe for our ammonia-water particles at 78 K.^{61,68} In the hemideuterate studies, the focus was mainly on the OD-stretching band, which is strongly structured for experiments carried out at 107-110 K, indicating a crystalline deuterate structure (at 102 K, the resulting particles are assigned to an amorphous structure based on the observed broad bands).⁶¹ Again, there is much greater structure observed in the OD-stretching region for the deuterate spectra compared to the broad bands in our mixed ammonia-water aerosol particle spectra. Again, this is a clear indication that our particles are not hydrates.

It is also worthwhile to briefly compare the ammonia-water aerosol spectra with spectra of ammonia-acetylene particles, which were previously measured and analyzed in our group.³⁴ The latter were found to have a co-crystalline structure. The ammonia ν_2 band in the ammonia-acetylene co-crystal observed at 1093 cm^{-1} is quite narrow, similar to the pure ammonia ν_2 band at 1067 cm^{-1} . This is in contrast to the broad band we observe for our ammonia-water aerosol particles at the same temperature and further indicates that the ammonia-water particles do not have any long-range order.

4.3.1.4 Comparison to calculated spectra

In order to confirm our experimental results that indicate the formation of molecularly mixed aerosol particles without long range order, we have performed vibrational exciton calculations for different ammonia particle structures. Calculations were performed for pure cubic and amorphous ammonia particles (Section 4.2.2). Figure 4.3 shows the comparison between experimental and calculated spectra in the region of the ammonia ν_2 band. The experimental spectrum of pure ammonia (panel (a)) closely matches the calculated spectrum for an octahedral ammonia particle

with a cubic crystal structure. (Note that the experimental spectrum also shows the $\nu_2 + \nu_6$ combination band at 1104 cm^{-1} , which is not included in the simulation.) There is also very good agreement between the experimental ammonia-water spectrum and the calculated amorphous spectrum in panel (b). Both show a similarly broad unstructured band, which is by a factor of ~ 2.5 broader compared with the band of the crystalline particle. This further confirms that we form molecularly mixed amorphous (non-hydrate) ammonia-water aerosol particles immediately after injection of a premixed sample or simultaneous injection of the two sample gases.

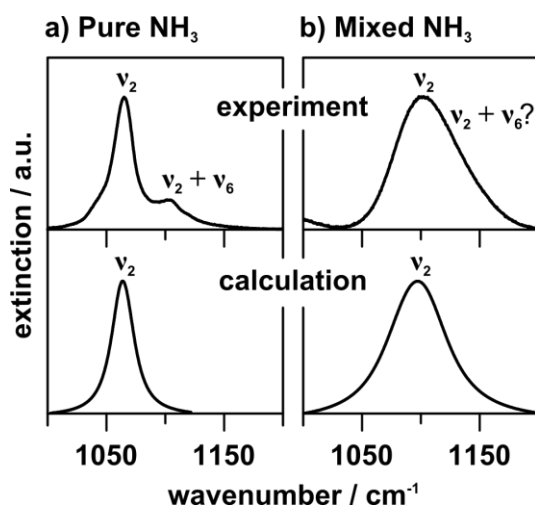


Figure 4.3: Comparison of experimental spectra and calculated spectra for a) pure crystalline ammonia aerosol particles and b) mixed amorphous ammonia-water aerosol particles.

4.3.1.5 Mixing in core-shell ammonia-water particles

For both the premixed and simultaneous injection measurements shown in Figure 4.1, the mixed particles were already formed by the time we record the first spectrum (i.e., $< 1\text{ s}$). As mentioned, a series of spectra were recorded for a further 30 minutes after injection. During this time, no changes were observed in the spectra of either the pure particles or the mixed particles. To

investigate how fast mixing of pure solid ammonia and pure solid water occurs, we measured spectra for aerosol particles formed after sequential injection of ammonia and water into the cell. The sequential injection initially forms core-shell particles with the substance injected first forming the core and the substance injected second forming the shell. We can then observe changes to the spectra with time due to the mixing of the two substances via solid state diffusion.

Time-resolved spectra from two sequential measurements with an H₂O:NH₃ ratio of ~2:1 are shown in Figure 4.4 in the region of the ammonia ν_2 mode. The spectra in Figure 4.4 are scaled to the same maximum to facilitate comparison of the band profiles. (Note that during the 30 minute measurement, particles gradually move towards the walls of the cell and out of the path of the IR beam, leading to a gradual decrease in signal intensity.) Panel (a) shows spectra from an experiment where water was injected first while panel (b) shows spectra from an experiment where ammonia was injected first. In both cases, some mixing has already started by the time we record the first spectrum (which is immediately after injection of the second gas sample).

Therefore, the first spectra contain features of the pure crystalline substances (Figure 4.1(a) to (c)) together with features of the molecularly mixed particles (Figure 4.1(d) and (e)). Over time, there is an evolution of the ammonia ν_2 band shape more and more toward that of the molecularly mixed particles for both injection orders. As a result, the broad band at 1100 cm⁻¹ gains intensity and the narrower band at 1066 cm⁻¹ loses intensity over time. While the spectra in Figure 4.4 approach the broad ν_2 band of the mixed state, the signature of the pure crystalline state at 1066 cm⁻¹ does not completely disappear within the 30 minute experiment. This experiment was repeated and spectra were monitored for 120 minutes after injection (not shown). Even during this longer time frame, the spectra never reached the fully mixed state seen in the simultaneous and premixed spectra (Figure 4.1(d) and (e)). The amount of further mixing after 30 minutes was found to be minimal.

We think that during the sequential injections a certain fraction of pure ammonia particles (and also pure water particles) are formed, which cannot mix by solid state diffusion (see discussion further below). These pure particles are likely responsible for the sudden stop of the mixing process. The extent of mixing can also be determined by examining changes to the band profiles in the region of the OH and NH stretching motions in the sequential measurements (not shown). With time, the OH stretching band evolves toward the profile observed in Figure 4.1(d) and (e)—namely, a broadening of the band at the base. Also, the NH stretching band broadens with time and becomes less prominent. In addition, a decrease in the intensity of the water dangling-OH band is observed (not shown). Devlin et al.⁶¹ previously used the decrease and disappearance of this band in IR spectra (referred to in their case as ‘dangling-D’ since they used D₂O in measurements) to indicate the coating of D₂O nanocrystals with ammonia.

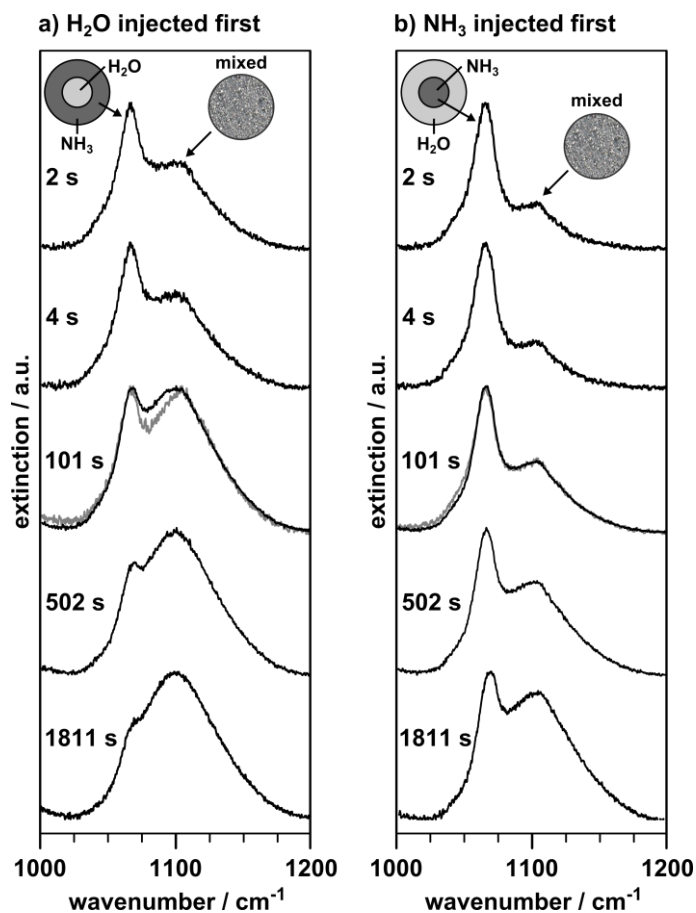


Figure 4.4: Temporal evolution in the region of the ammonia umbrella mode after sequential injection of the sample gases. The injection orders were: a) H₂O then NH₃ and b) NH₃ then H₂O. All other injection conditions remained the same for both experiments. The ratio of H₂O:NH₃ is approximately 2:1. Examples of fitting results used to create the plots in Figure 4.6 are shown for the spectra recorded at 101 s (grey traces).

To examine the effect of the ratio of H₂O:NH₃ on the mixing kinetics, the experiments shown in Figure 4.4 were repeated with a H₂O:NH₃ ratio of approximately 5:1 (which corresponds to the simultaneous measurement in Figure 4.2(b)). For these experiments, the concentration of the water gas sample remained constant while a lower concentration was used for the ammonia gas sample. The results for these experiments are presented in Figure 4.5 in an analogous manner to

the spectra in Figure 4.4. The evolution of the bands with time is very similar to those observed for the 2:1 ratio. The difference to Figure 4.4 is that everything happens faster in Figure 4.5 and that mixing almost goes to completion after 30 minutes. Faster mixing is to be expected for the 5:1 ratio because the ammonia shell (trace (a)) is thinner and the ammonia core (trace (b)) is smaller compared to the 2:1 mixture. A lower ammonia content obviously also results in a much lower fraction of pure ammonia particles (most ammonia is bound in core-shell particles).

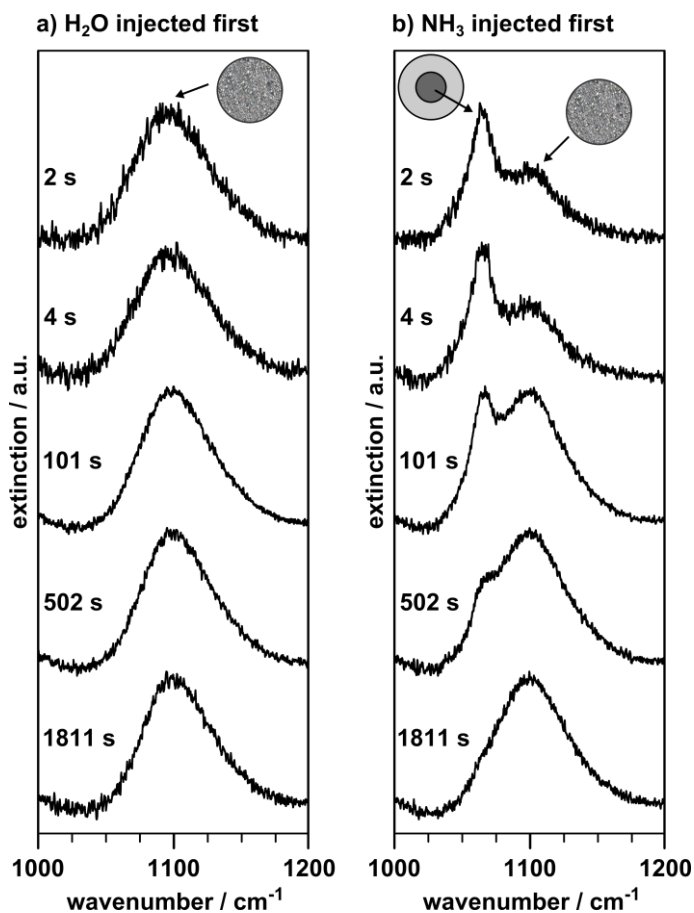


Figure 4.5: As for Figure 4.4, but with a ratio of H₂O:NH₃ of approximately 5:1.

Fitting the spectral band shapes allows us to quantify the extent of molecular mixing in the ammonia-water aerosol particles. We analyzed the fraction of mixing for both the 2:1 and 5:1 H₂O:NH₃ aerosol particle measurements (Figure 4.4 and Figure 4.5, respectively). A linear combination of the pure (Figure 4.1(a)) and mixed (Figure 4.2(a) or (b)) band shapes were fitted to the experimental spectra. We assumed the spectra after simultaneous injection to represent the case where the particles have the maximum extent of mixing since there were no further changes to these spectra with time. Examples of fitted spectra are shown in Figure 4.4 for the spectra recorded 101 s after injection (grey traces). The plots in Figure 4.6 show the fraction of mixed ammonia as a function of time for both injection orders. (It is important to note that the mixing fraction in the figures is not the same as the mole fraction since the extinction coefficients for the ν_2 band in pure and mixed ammonia are not equal (see, for example, the work by d'Hendecourt and Allamandola¹⁴⁸ of band strengths for the ν_2 band in pure ammonia and a 3:1 water-ammonia mixture)). The data in Figure 4.6(a) corresponds to the 2:1 spectra (Figure 4.4), while the plot in Figure 4.6(b) corresponds to the 5:1 spectra (Figure 4.5). Both mixing ratios show similar trends with time. Mixing is fast in the first 300 s after injection, and then begins to level off. For both concentration ratios, the extent of mixing is greater when water is injected first, though the difference between the injection orders is less pronounced when the concentration of ammonia is lower. The fraction of molecularly mixed ammonia reaches the greatest value when less ammonia is present in the aerosol particles.

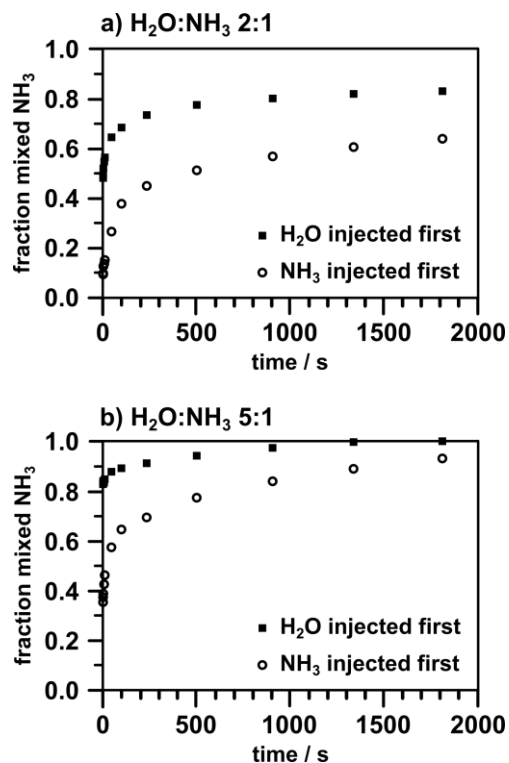


Figure 4.6: Fraction of molecularly mixed NH_3 as a function of time for particles formed by sequential injection. The ratio of $\text{H}_2\text{O}:\text{NH}_3$ is approximately a) 2:1 and b) 5:1. The corresponding spectra are shown in Figure 4.4 and Figure 4.5, respectively. Sample fits are depicted in Figure 4.4 (grey traces) for spectra recorded 101 s after injection.

We suspect that the fact that the onset of mixing always occurs sooner when water is injected first and also proceeds to a more fully mixed state may be related to the different melting points of water and ammonia (273.15 K and 195.41 K, respectively, at 1 atm). When water is injected first, it freezes and forms solid aerosol particles already in the lower part of the injection tube just before the entrance into the actual cell (see Figure 1 in Lang et al.³⁵ or Figure 2.1 in this thesis). These water particles could then act as nucleation sites for the ammonia gas because the ammonia is not likely to freeze in the inlet tube due to its lower melting point. This leads to the formation of predominantly core-shell particles and not the formation of a substantial fraction of pure ammonia

and pure water particles. Molecular mixing would then proceed via solid state diffusion in these core-shell particles. It has been previously shown that ammonia on the surface of water particles can diffuse within the particles.^{61,68} In the case where ammonia is injected followed by water, it is likely that more pure water and pure ammonia particles are formed by homogeneous freezing instead of core-shell particles. As said, part of the water vapour will freeze in the inlet tube and thus no longer be available for heterogeneous freezing. This results in fewer core-shell particles in comparison to the opposite injection order, and thus less mixing via solid state diffusion. This explanation is consistent with the spectra and data in Figure 4.4 to Figure 4.6. We believe that the majority of mixing occurs via solid state diffusion after the formation of core-shell particles, although it may not be the sole mechanism for the formation of molecularly mixed particles. Collision of pure particles in the cell followed by solid state diffusion might contribute as well. Sublimation and re-condensation of gas is not plausible considering the calculated sublimation pressures for ammonia and water of 1.3×10^{-14} bar and 5.2×10^{-27} bar, respectively (at 78 K).¹⁷⁷ As we are not able to accurately quantify the properties of our particles (e. g. we do not know the interface area in the core-shell particles), we do not try to assign a rate to the mixing process observed in spectra.

4.3.2 Acetylene-water aerosol particles

4.3.2.1 Overview of aerosol particle IR spectra

We observed very similar trends for the acetylene-water aerosol particles as for the ammonia-water particles. Since the ammonia-water results have already been discussed in detail, we only briefly summarize the results for the acetylene-water aerosol particles.

Overview IR spectra of pure and molecularly mixed solid acetylene and water aerosol particles at 78 K are shown in Figure 4.7. A summary of the band positions in the pure and mixed acetylene and water aerosol particle spectra is provided in Table 4.2. There were no significant changes observed in any of the spectra over a measurement time of 30 minutes. The spectrum of pure acetylene particles (trace (a)) most resembles that of orthorhombic polycrystalline (partially amorphous) particles.^{21,28,32,34,178} Thin films of acetylene were also found to be polycrystalline at 63 K.¹⁴⁹ The most prominent bands in the spectrum are the ν_5 band at 773 cm^{-1} (the bending mode) and the ν_3 band at 3230 cm^{-1} (anti-symmetric CH stretching mode). We will focus the majority of our analysis of the molecularly mixed acetylene-water particles on the acetylene ν_5 band due to its strong transition dipole and sensitivity to particle properties.²¹ A spectrum for pure water aerosol particles is shown in trace (b). A detailed description of the corresponding bands is given in Section 4.3.1.1. Figure 4.7(c) displays a sum spectrum of pure acetylene particles (trace (a)) and pure water particles (trace (b)) with a ratio of $\text{H}_2\text{O}:\text{C}_2\text{H}_2$ of $\sim 3:1$. An experimental spectrum of molecularly mixed acetylene-water particles with the same $\text{H}_2\text{O}:\text{C}_2\text{H}_2$ ratio is shown in trace (d). It was recorded after simultaneous injection of the two sample gases into the cell. The ratio of water to acetylene was determined from integration of bands using the band strengths obtained for water¹⁴⁸ and acetylene^{163,178} thin films, both at 10 K. (Note that due to the overlap of the major water and acetylene bands, integration was performed for the respective pure spectra with the same ratio of the two substances.)

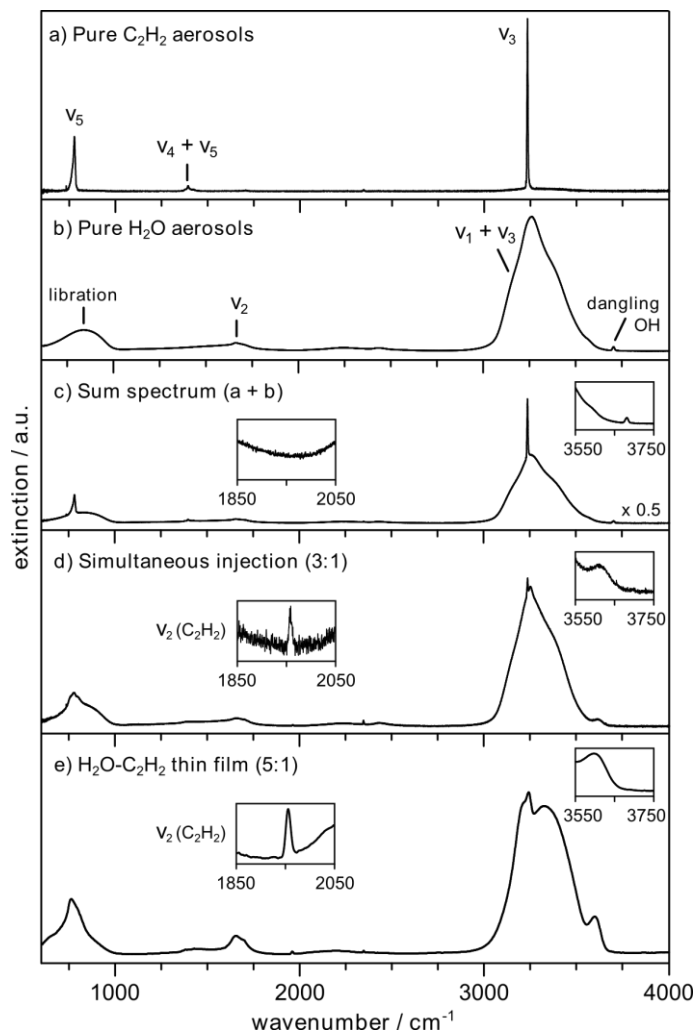


Figure 4.7: Overview infrared aerosol particle spectra for a) pure C_2H_2 , b) pure H_2O , c) a sum spectrum (addition of spectrum (a) and spectrum (b)), and d) particles formed after simultaneous injection of C_2H_2 and H_2O samples. The ratio $H_2O:C_2H_2$ is approximately 3:1 in (c) and (d). e) An $H_2O-C_2H_2$ (5:1) thin film measurement at 20 K. The thin film spectrum was taken from the work of Hudson et al.^{164,176} Insets show an expanded view of the region for the C_2H_2 v_2 mode and the dangling-OH stretch region.

Table 4.2: Infrared band assignments for pure and mixed C₂H₂ and H₂O aerosol particles formed in the cooling cell (see Figure 4.7).

	Band	Position (cm ⁻¹)	
		Pure	Mixed*
C ₂ H ₂	v ₅	773	789 [‡]
	v ₄ + v ₅	1390	1390 [‡]
	v ₂	-	1958
	v ₃	3230	3231 [‡]
H ₂ O	libration	814	‡
	v ₂	1650	1653
	v ₁ + v ₃	3257	3246 [‡]
	dangling-OH	3698	-
	unassigned	-	3611

*Taken from spectra recorded after simultaneous injection of the sample gases

‡H₂O and C₂H₂ overlap in this region

The overlap between the most intense acetylene bands and the broad water bands in the region around 780 cm⁻¹ and 3230 cm⁻¹ complicates the detection and analysis of spectral features.

Nonetheless, distinct changes are observed between the pure acetylene bands and the bands of the molecularly mixed particles. The v₅ band (which overlaps with the water libration) is broadened and its position shifts to 789 cm⁻¹ for the mixed particles. The acetylene v₃ band in the spectrum of the mixed particles appears as a narrow sharp peak on top of the broad water OH stretching band. Its position is only shifted by 1 cm⁻¹ towards higher wavenumbers compared with pure acetylene particles. As seen for the ammonia-water mixed aerosol particles, the dangling-OH stretch band is not present in the mixed acetylene-water aerosol particle spectrum; however, a new shoulder at 3611 cm⁻¹ appears (insets in Figure 4.7(d) and (e)). The origin of this band is not clear. Some suggestions are provided by Hagen et al.,¹⁴⁹ e.g. shifted pure water or pure acetylene stretching absorptions. In addition, the normally IR inactive acetylene v₂ band (C-C stretching motion)

becomes active in the spectrum of the mixed particles (inset in traces (d) and (e)). This effect was previously observed in $\text{NH}_3\text{-C}_2\text{H}_2$ aerosol particles and was attributed to a change in the site symmetry of the C_2H_2 in the pure crystal versus the mixed state.³⁴

4.3.2.2 Comparison to thin film spectra

There is considerably less literature for the acetylene-water system compared to ammonia-water. There are very few studies of acetylene-water thin films and we are not aware of any other studies of acetylene-water aerosol particles. Figure 4.7(e) shows an example acetylene thin film measurement from the work of Hudson et al.^{164,176} The spectrum in this figure is for a $\text{H}_2\text{O-C}_2\text{H}_2$ mixing ratio of 5:1, though their work also includes spectra for a few other ratios, all recorded at 20 K. There are many of the same features in our particle spectrum as in the thin film spectrum, which include the broadening of the acetylene ν_5 and ν_3 bands, the shoulder at approximately 3611 cm^{-1} , and an IR-active acetylene ν_2 band. These features were also visible in their 1:1 film (not shown here). Hagen et al.¹⁴⁹ and Boudin et al.¹⁶³ also present a spectrum for an acetylene-water thin film (ratios of $\text{H}_2\text{O:C}_2\text{H}_2 = 1:2$ and $\text{H}_2\text{O:C}_2\text{H}_2 = 5:1$, respectively), which also exhibit very similar features (not shown). In addition, the latter contribution observed splitting of the acetylene bands, likely due to different C_2H_2 configurations within the water ice matrix, as acetylene was previously shown to bind to water ice surfaces as both a proton acceptor and a proton donor.¹⁷⁹ It is unclear if they also detected the shoulder around 3611 cm^{-1} , as this spectral region is not shown for the mixtures. Based on these comparisons, it is likely that we form molecularly mixed aerosol particles with an amorphous structure (see below).

It is possible for acetylene to form a co-crystal with water, where water molecules form a cage around an acetylene molecule (also referred to as a clathrate hydrate)^{165,180} with a ratio of $\text{H}_2\text{O:C}_2\text{H}_2$

equal to 46:8. Consani and Pimentel¹⁶⁵ measured IR spectra for thin films of the acetylene-water co-crystal, though they looked at C₂H₂-D₂O and C₂D₂-H₂O combinations to avoid overlap of the acetylene and water bands. They compared C₂D₂-H₂O spectra of deposited films (molecularly mixed) and annealed films (co-crystal) in the region of the C₂D₂ ν_3 and ν_5 bands. Both the ν_3 and ν_5 bands are much narrower and more intense for the co-crystalline structure compared with the molecularly mixed films. In addition, they observed a large blue shift (~ 27 cm⁻¹) for the ν_3 band and a large red shift (~ 30 cm⁻¹) for the ν_5 band in the co-crystal compared to pure acetylene. Our aerosols particles are not co-crystalline structures. The H₂O:C₂H₂ ratio in our work is very different from the one needed to form co-crystals and our conditions for particle formation are quite different from what is used to form the co-crystal. (Thin films of the acetylene-water co-crystal were formed by depositing the sample gases at 9-12 K and annealing to 130-135 K¹⁶⁵). Furthermore, the band shifts observed for the co-crystal do not correspond to what we find for our C₂H₂-H₂O aerosol particles. For the aerosol particles, the ν_3 band is shifted by only 1 cm⁻¹ and the ν_5 band is blue shifted and not red shifted compared to pure acetylene.

4.3.2.3 Comparison to calculated spectra

Figure 4.8 compares experimental and calculated spectra for aerosol particles in the region of the acetylene ν_5 band. The spectra in panel (a) are for the pure acetylene particles while the spectra in panel (b) are for mixed acetylene-water particles. (The experimental spectrum in panel (b) has had the contribution from the broad water libration subtracted to facilitate comparison to the calculated spectrum.) There is very good agreement between the experimental pure acetylene spectrum and exciton calculation for the polycrystalline particle derived from an orthorhombic structure. There is also good agreement between the experimental acetylene-water spectrum and the calculated amorphous acetylene spectrum. As for the ammonia case, the amorphous structure

seems a good approximation for molecularly mixed. These calculations provide further confirmation that we form molecularly mixed acetylene-water aerosol particles with an amorphous structure.

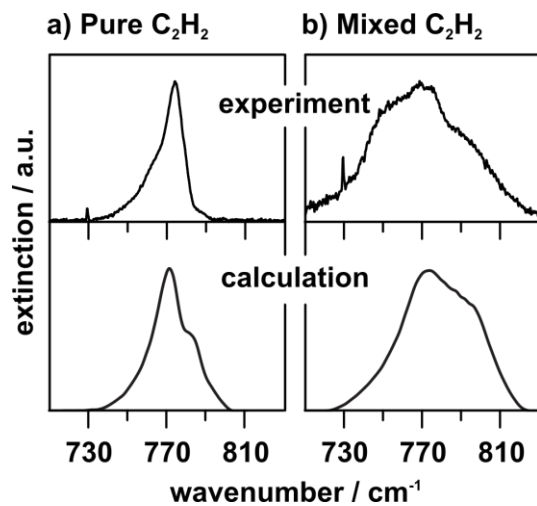


Figure 4.8: Comparison of experimental spectra and calculated spectra for a) pure polycrystalline acetylene particles and b) mixed amorphous acetylene-water aerosol particles. The calculated spectra were taken from the work of Preston et al.²¹ For the experimental acetylene-water spectrum, we subtracted a pure water spectrum to remove the major contributions from the broad water libration band.

4.3.2.4 Mixing in core-shell acetylene-water particles

Sequential injection experiments were performed for the acetylene-water aerosol particles to study mixing in core-shell particles. Over time, similar mixing trends are observed as described in Section 4.3.1.5 for the ammonia-water particles. Figure 4.9 displays time-dependent spectra after the sequential injection of first water then acetylene in the region of the acetylene ν_5 band. (This band overlaps the broad water libration band.) The ratio of H₂O:C₂H₂ is approximately 3:1, which is the same ratio as for the simultaneous injection measurement shown in Figure 4.7(d). Even though

the overlap between the acetylene and water band complicates the analysis, there are distinct changes that can be monitored. Over time, the acetylene ν_5 band evolves from the sharp band of pure acetylene toward the broader band arising from molecularly mixed acetylene. This broadening effect is similar to what is observed for the ammonia-water aerosol particles in Section 4.3.1.5. In addition, we also see the following temporal evolution of other bands in the spectra (not shown): the acetylene ν_3 band broadens with time, there is a decrease in the intensity of the dangling-OH band of water, and the shoulder at 3611 cm^{-1} increases in intensity. As for the ammonia-water aerosol particles, the majority of mixing likely occurs via solid state diffusion after the formation of core-shell particles. (The calculated sublimation pressures for acetylene at 78 K is $5.0 \times 10^{-9}\text{ bar}^{177}$ which speaks against substantial contribution to mixing by sublimation and recondensation of gas.) Again, we do not try to extract any rate constants for the mixing process because we cannot accurately quantify the properties of our particles.

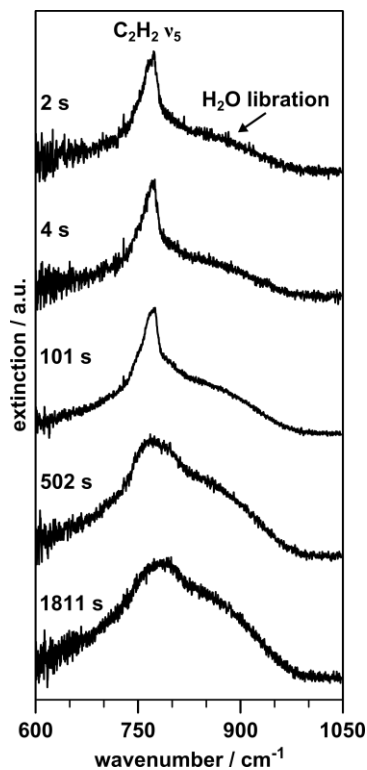


Figure 4.9: Temporal evolution of spectra in the region of the $C_2H_2 \nu_5$ mode after sequential injection of the sample gases (H_2O then C_2H_2). The ratio of $H_2O:C_2H_2$ is approximately 3:1.

4.4 Summary

We find that ammonia-water and acetylene-water form amorphous molecularly mixed aerosol particles in a bath gas cooling cell at 78 K. This differs from results for acetylene-carbon dioxide,^{32,33} ammonia-acetylene,³⁴ and water-carbon dioxide¹⁶⁶ particles formed under similar conditions. The infrared spectra of these particles exhibit distinct features that allow their identification and clear distinction from pure particles and mixed hydrate particles. Our studies on core-shell particles reveal fast solid state diffusion that leads to the formation of molecularly mixed particles (on the order of a few tens of minutes). Ammonia-water and acetylene-water particles

show a similar structural behaviour, which clearly differs from that of acetylene-carbon dioxide, ammonia-acetylene, and water-carbon dioxide particles.

Molecularly mixed ammonia-water and acetylene-water aerosol particles without any long range order form under various conditions (e. g. various mixing ratios) and might thus be more important in planetary and lunar atmospheres than the corresponding hydrate structures. The spectra of these mixed systems are useful for the prediction of the type of aerosol particles that might be present in these atmospheres as well as for the analysis of spectra from future orbiter missions.

Chapter 5: Optical trapping of single aerosol particles

5.1 Introduction

This chapter focuses on the study of single aerosol particles at both room temperature and low temperatures (as low as $-45\text{ }^{\circ}\text{C}$) using the counter-propagating Bessel beam (CPBB) optical trap. The eventual goal is to study single aerosol particles at 78 K to complement the ensemble aerosol studies in Chapter 3 and Chapter 4. This chapter demonstrates the use of the CPBB optical trap at room temperature for the study of aqueous carbohydrate particles and how the CPBB design is coupled to a temperature-controlled cell for preliminary study of the freezing of single aerosol particles.

5.1.1 Optical trapping: trapping forces

This section focuses on the forces that allow for trapping of aerosol particles by light. In the current work, the focus is on particles that have a refractive index (RI) higher than that of the surrounding medium. When this is the case, particles may become trapped in the high intensity regions of a

laser beam.^{93,181} The major forces that are involved in optical trapping are illustrated in Figure 5.1. These forces are known as the gradient force and the scattering force.¹⁸¹

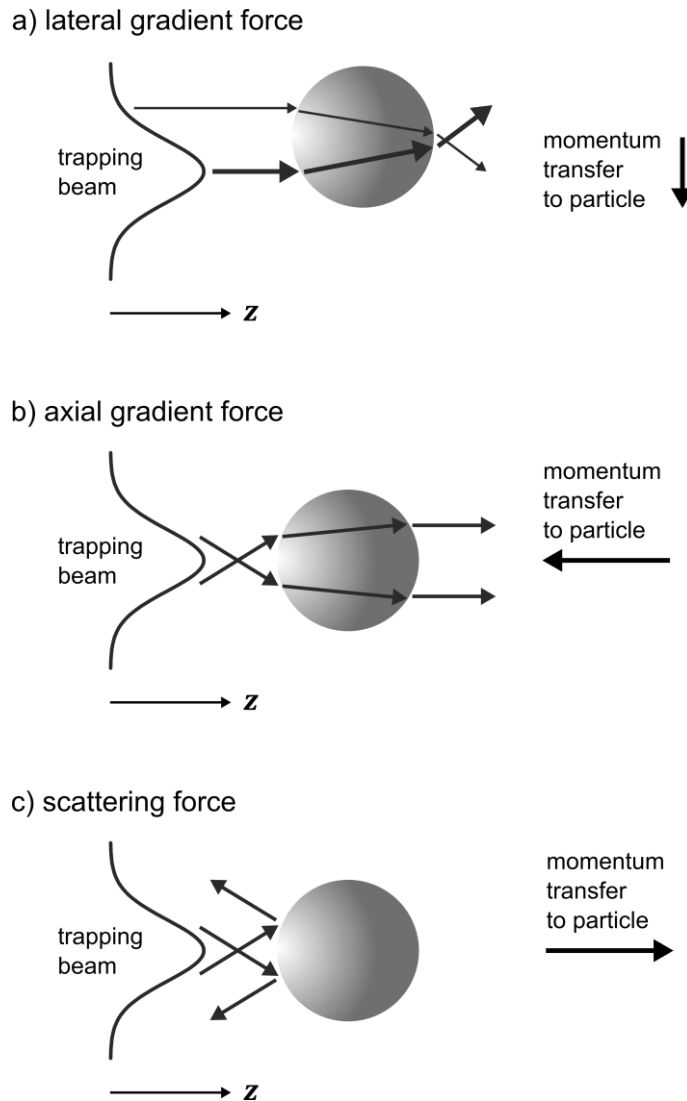


Figure 5.1: Ray optics diagrams for a) the lateral gradient force, b) the axial gradient force, and c) the scattering force involved in optical trapping.

The forces described in Figure 5.1 are described in terms of a focused Gaussian trapping beam. The gradient forces result from intensity gradients in the Gaussian beam. When light from the trapping

beam interacts with a particle, there is a transfer of momentum to the particle as the light refracts, as illustrated in Figure 5.1(a) and (b). If a particle moves out of the focus of the beam laterally, the lateral gradient force acts to restore the particle to the central (high intensity) region of the beam whereas the axial gradient force acts in the direction opposite to beam propagation. The scattering force is illustrated in Figure 5.1(c). The scattering forces result because photons from the trapping beam transfer momentum to the particle along the z -axis in the direction of beam propagation.

The ray-optics description of the optical trapping forces shown in Figure 5.1 is sufficient when particles are much larger than the wavelength of the trapping beam. When the size of particles is on the same order as the wavelength of light, as is the case for some particles in this work, it is more accurate to describe the trapping forces on the particle in relation to the electric field.¹⁸¹ In the region near the trapped particle, there is an intensity gradient in the beam. The gradient force, F_{grad} , relates to the refraction of light according to:

$$F_{grad} = \frac{-n^3 r^3}{2} \left(\frac{N_{RI}^2 - 1}{N_{RI}^2 + 2} \right) \nabla(|E|^2) \quad (5.1)$$

where N_{RI} is the ratio of the RI of the particle to the RI, n , of the medium, and r is the particle radius.¹⁸¹ As in the ray optics description, the gradient force directs the particle to the highest intensity region of the beam. The scattering force (arising from scattering of the light), F_{scat} , can be calculated from:

$$F_{scat} = \frac{I_0}{c} \frac{128\pi^5 r^6}{3\lambda^4} \left(\frac{N_{RI}^2 - 1}{N_{RI}^2 + 2} \right)^2 n \quad (5.2)$$

where I_0 is the intensity of the beam and λ is the wavelength of light.¹⁸¹ The scattering force acts in the direction of beam propagation.

Different optical trapping and manipulation techniques rely on the balance or relative strengths of these trapping forces. For example, when the scattering force is greater than the axial gradient force, particles can be seen to move along the z -axis in the direction of beam propagation. This is referred to as “optical guiding”.⁹³ In contrast, optical tweezers confine particles to a small three-dimensional region in space using a single trapping beam. In order to produce a three-dimensional trap, the axial gradient force must exceed the scattering force and to achieve this requires a beam that is extremely tightly focused (typically achieved using a microscope objective with a high numerical aperture).¹⁸¹

5.1.2 Bessel beams

All of the optical trapping experiments in this work employ the CPBB optical trap. The design and properties of a CPBB optical trap are discussed in Section 5.1.3, while the advantages for a CPBB optical trap are discussed in further detail and compared to other trapping methods in Section 5.1.4. In this section, the Bessel beam itself is described. A Bessel beam has a cross-sectional view that consists of concentric rings. A unique feature of Bessel beams is that they are considered to be “non-diffracting”. This property means that Bessel beams are attractive for use in many applications, including optical trapping. This section outlines the description and formation of Bessel beams, and why they are considered to be “non-diffracting”.

Bessel beams can be described in terms of a Bessel function, J_b , and the order of the Bessel beam relates to the order of the Bessel function (where b is the order of the function). A cross-sectional image for a zeroth-order ($b = 0$) Bessel beam is shown in Figure 5.2. Zeroth-order Bessel beams have a bright core while the higher order ($b > 0$) Bessel beams have a dark core. The experiments in this thesis all make use of a zeroth-order Bessel beam (the term Bessel beam will always refer to

a zeroth-order Bessel beam in the subsequent descriptions). Particles with a higher RI than the surrounding medium can become optically trapped in the high intensity regions of the Bessel beam (see Section 5.1.1), i.e. the core and rings.

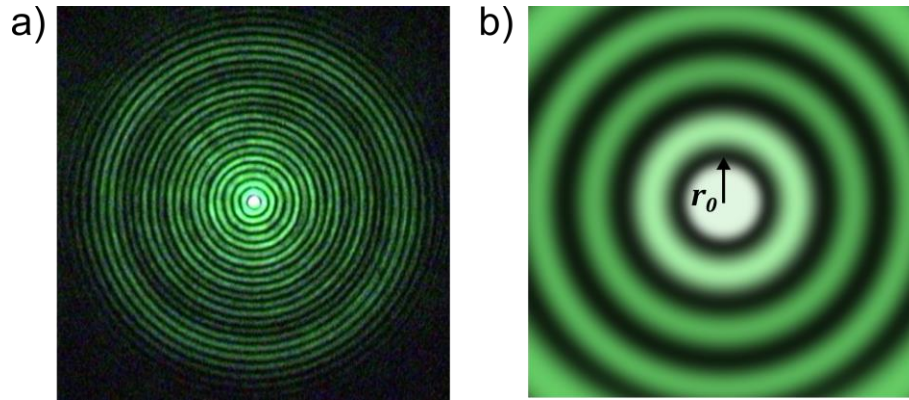


Figure 5.2: a) A cross-sectional view of a zeroth-order Bessel beam created using an axicon and b) a simulated image showing a close up view of the Bessel beam core and several rings to illustrate the core radius, r_0 .

One property of Bessel beams relates to the power (or energy) carried in each ring. The integrated intensity of each ring is equal to the power carried in the core of the Bessel beam. In theory, a true Bessel beam would carry infinite power over an infinite number of rings.¹⁸² Since the number of rings is proportional to the propagation distance of the Bessel beam, the true Bessel beam would also propagate over an infinite distance. In reality, one cannot create a true Bessel beam; however, Durnin et al.¹⁸³ have shown that it is possible to create a pseudo-Bessel beam experimentally. Such a beam still possesses the “non-diffracting” property of the true Bessel beam (described later in this section), but since the cross section is composed of a finite number of rings over a finite area, it carries a finite power.¹⁸² The experimental pseudo-Bessel beam will be referred to simply as a Bessel beam in the remainder of this work.

A common method of forming a Bessel beam (and the method used in the current work) is to pass a Gaussian beam through an axicon (a conical lens).¹⁸⁴ (Higher order Bessel beams can also be created using an axicon but with an incident Laguerre-Gaussian beam.¹⁸⁵) Other methods to form Bessel beams include the use of an annular slit with a converging lens or holographic techniques.^{182,184} Axicons are often chosen to form Bessel beams since this constitutes a highly efficient formation method (e.g. in comparison to an annular slit, where a fraction of the incident Gaussian beam is lost).¹⁸² In the case of an axicon, the light from the incident Gaussian beam refracts towards the central z-axis after passing through the axicon, as illustrated in Figure 5.3. The Bessel beam is formed by the interference of this light after the axicon.

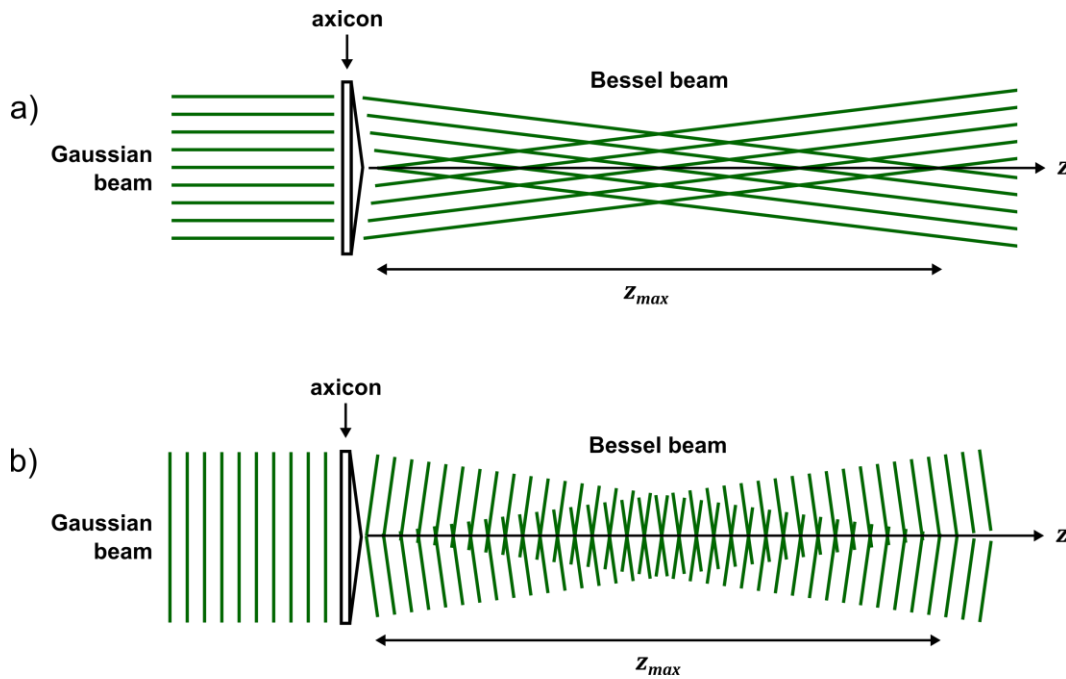


Figure 5.3: The formation of a Bessel beam from an incident Gaussian beam using an axicon illustrated as a) a ray tracing diagram and b) plane waves.

A zeroth-order Bessel beam is described by:⁹³

$$E(r, \phi, z) = E_0 \exp(i\vec{k}_z z) J_0(\vec{k}_r r) \quad (5.3)$$

where r , ϕ , and z are the radial, azimuthal, and longitudinal components, respectively, and \vec{k}_z and \vec{k}_r are the longitudinal and radial wavevectors, respectively. Each of these wavevectors is illustrated in Figure 5.4 for a Bessel beam described in terms of plane waves (with wavevectors \vec{k}) propagating along a cone. The wavevectors are related by:

$$\vec{k}_z = \vec{k} \cos\theta \quad (5.4)$$

$$\vec{k}_r = \vec{k} \sin\theta \quad (5.5)$$

where θ is the opening angle of the cone (see Figure 5.4(a)) and the wavevector \vec{k} is related to the wavelength, λ , of the Bessel beam by:¹⁸²

$$\vec{k} = \frac{2\pi}{\lambda} \quad (5.6)$$

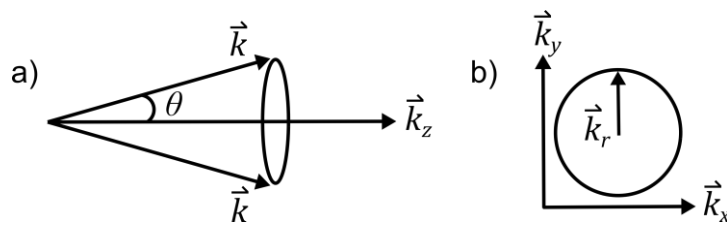


Figure 5.4: a) The longitudinal wavevector, \vec{k}_z , and b) radial wavevector, \vec{k}_r , for a Bessel beam described in terms of plane waves propagating along a cone.

The Bessel beam properties are defined by the opening angle of the axicon and the beam waist of the incident Gaussian beam. The axicon opening angle, γ , and the cone opening angle, θ , are approximately related by:^{93,182}

$$\theta = (n - 1)\gamma \quad (5.7)$$

where n is the RI of the axicon. The axicon opening angle and apex angle, τ , are illustrated in Figure 5.5. The Bessel beam propagation distance in the non-diffracting region, Z_{max} , is illustrated in Figure 5.3 and can be calculated according to:⁹²

$$z_{max} = \frac{w_0}{(n - 1)\gamma} \quad (5.8)$$

where w_0 is the diameter of the incident Gaussian beam. The Bessel beam core size, r_0 , (the radial distance from the core centre to the first intensity minimum, see Figure 5.2(b)) is given by:

$$r_0 = \frac{2.405}{\bar{k}_r} \quad (5.9)$$

The factor 2.405 in Equation (5.9) comes from the result for the root of the zeroth-order Bessel function.¹⁸²



Figure 5.5: Diagram showing the opening angle, γ , and apex angle, τ , of an axicon.

A major advantage of Bessel beams compared to Gaussian beams is that they are said to be “non-diffracting”. For a Gaussian beam and a Bessel beam core of similar diameter, the guiding distance (distance over which the scattering force acts to guide particles,¹⁸⁶ refer to Section 5.1.1) for the Bessel beam can be up to ten times larger than for the Gaussian beam.⁹² The divergence of a Gaussian beam is described by the Rayleigh range, Z_r , according to:

$$Z_r = \frac{\pi w_0^2}{\lambda} \quad (5.10)$$

The Rayleigh range describes the propagation distance for a Gaussian beam’s cross-section to increase by a factor of two.¹⁸²

Additionally, unlike a Gaussian beam, which diffracts upon encountering an obstacle, the Bessel beam can be viewed to have a core that is propagation invariant within the region denoted by Z_{max} .¹⁸² When an obstacle blocks the core of the Bessel beam, the light from the unobstructed rings can interfere to reform the core after a certain distance past the obstacle. This distance, Z_{min} , is therefore related, in part, to the size of the obstacle. For an obstacle with a radius given by r_{obs} , Z_{min} is given by:⁹³

$$Z_{min} = \frac{r_{obs} \vec{k}}{\vec{k}_r} \quad (5.11)$$

The reformation of a Bessel beam after an obstacle is shown in Figure 5.6. Immediately past the obstacle, there is a “shadow region” where the light is obstructed. However, because many of the Bessel beam rings are not blocked, the beam core can reform, and this constitutes the “non-diffracting” property of Bessel beams.

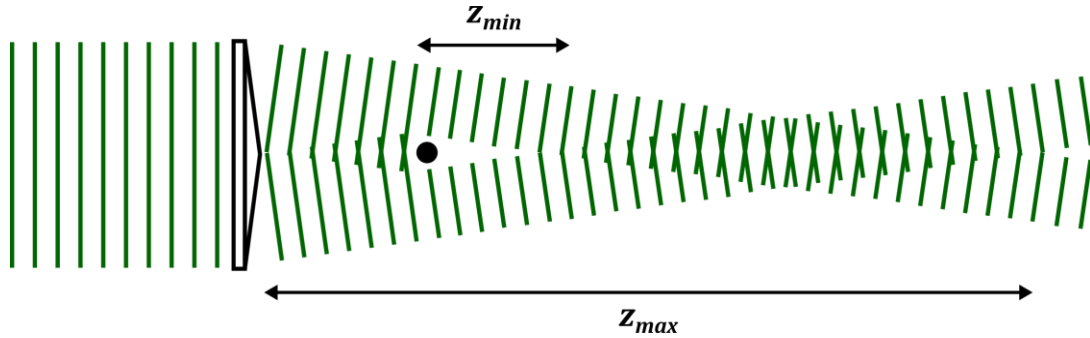


Figure 5.6: A Bessel beam illustrated as plane waves that encounters an obstacle. The Bessel beam reforms at a distance z_{min} after the obstacle.

5.1.3 Counter-propagating Bessel beam optical trap

The CPBB optical trap used in the current work is formed by two counter-propagating, orthogonally polarized Bessel beams that overlap in the trapping cell. (Note that when counter-propagating beams of like polarization are used, the setup is referred to as a “standing wave trap”,⁹³ and the trapping positions are defined based on the phase of the wave.¹⁸⁷) The use of Bessel beams in a standing wave counter-propagating optical trap was first introduced by Čižmár and coworkers for trapping polystyrene particles,^{187,188} while Reid and coworkers have made use of orthogonally polarized CPBB optical traps to study aerosol particles at room temperature.^{92-94,189} Our research group has recently used CPBBs for trapping of submicron-sized particles⁹⁶ and calculated the dynamics of submicron particles in this trap.¹⁹⁰ The CPBB trap in the current work makes use of a zeroth-order Bessel beam and particles are trapped in the high intensity core (particles may also become trapped in the Bessel beam rings; however these particles tend to not be quite as stable as those in the core).

Due to the small gradient force along the propagation axis (z -axis), the scattering force dominates in this direction and particles cannot be confined in three-dimensions within a single Bessel beam as, for example, in an optical tweezer. Note that a strong lateral gradient force acts to maintain the particles laterally in the high intensity regions of the beam, i.e. the Bessel beam core or rings, as described in Figure 5.1. This is the motivation for the use of the counter-propagating arrangement for the Bessel beam trap. The counter-propagating beams allow for three-dimensional confinement of particles when the scattering forces of the two beams are balanced. (A single Bessel beam can however be used to trap particles against a counter-propagating gas flow, where the scattering forces balance against the gravitational force and the drag force of the gas.^{95,191,192})

Figure 5.7 illustrates the formation of the Bessel beam in the trapping cell. In the CPBB optical trap setup, the incident Gaussian beam passes through an axicon to form a Bessel beam immediately past the axicon. The beam then passes through a polarizing beam splitter (PBS) cube, to create one arm of parallel polarization and a second of perpendicular polarization. (Note that this image does not include the PBS cube, which would be located after the axicon, just before the first lens, as shown in Figure 2.5. The scheme in Figure 5.7 is meant to illustrate the formation of the Bessel beam in the trapping cell for one of the Bessel beam arms.) After passing through several lenses, the Bessel beam is reformed in the trapping region where the two orthogonally polarized beams overlap to form the CPBB optical trap. This counter-propagating design means that when the scattering forces (described in Section 5.1.1) for each beam balance, particles may be trapped in the Bessel beam core around an equilibrium position.⁹³ When the Bessel beams are not aligned properly (and thus the scattering forces from each beam do not balance properly), particles can be seen to be optically guided along the core of each beam in the direction of beam propagation.

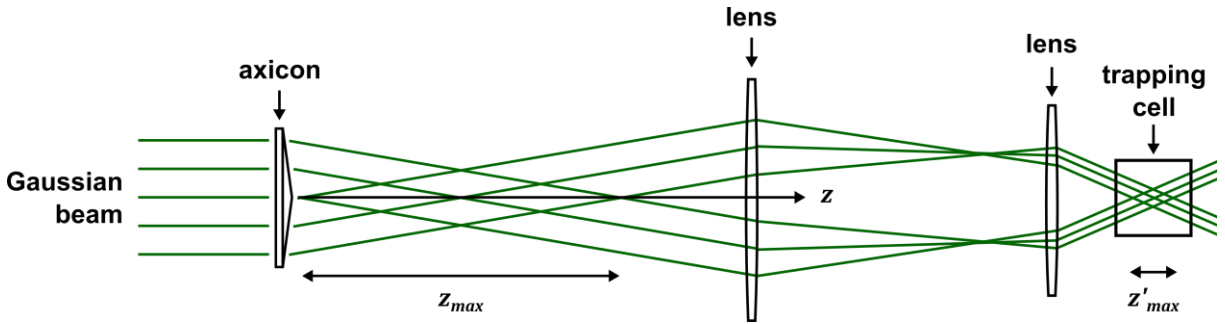


Figure 5.7: Reformation of the Bessel beam in the trapping cell after initial formation using an axicon. Note that this illustration does not show the second (counter-propagating) Bessel beam.

One interesting property of the CPBB optical trap is that longitudinal optical binding is possible, whereby multiple aerosol particles may be simultaneously trapped in a row.^{93,189,190,193,194} An image of the elastically scattered light from five particles simultaneously trapped in the CPBB optical trap is shown in Figure 5.8. In optical binding, there are no pre-defined trapping sites—the presence of a particle creates additional trapping sites.^{93,194} This occurs because a trapped particle will scatter light in all directions (e.g. Figure 2.11), including along the direction of beam propagation.



Figure 5.8: Five particles simultaneously trapped in a CPBB optical trap, demonstrating optical binding.

Optical binding is characterized by a regular spacing between particles, which is the case for the particles in Figure 5.8. The spacing between particles has previously been shown to be greater than the distance z_{min} (refer to Section 5.1.2).⁹³ It is possible to have more than five particles simultaneously trapped in the CPBB optical trap and the number of trapped particles can be an indication of the quality of the alignment of the two counter-propagating beams.

Carruthers et al.⁹⁴ have shown that the size of particles trapped in a CPBB optical trap is related to both the Bessel beam core size and the core power. Reducing the core diameter to 1.7 μm resulted in a greater likelihood of trapping smaller particles ($r < 500 \text{ nm}$). However, a larger core diameter of 4.5 μm allowed for trapping of larger particles as well as a greater size range of particles. A higher core power increased the number of larger particles that were trapped, in part by increasing the frequency of droplet coalescence. As well, Meresman et al.⁹² have found that particles larger than the Bessel beam core size can be trapped in the CPBB optical trap. The core radius, r_0 can be adjusted by changing the axicon to one with a different angle, τ (refer to Section 5.1.2).

5.1.4 Advantages of the counter-propagating Bessel beam optical trap

The CPBB optical trap was chosen in the present work to study single aerosol particles due to a few inherent advantages compared to other single particle techniques, including other optical trapping techniques. In this section, other trapping methods will be briefly described and compared to the CPBB optical trap to justify the choice of the CPBB optical trap in the present work.

One common technique to study single levitated particles is the electrodynamic balance (EDB). The EDB was first applied to aerosol particles to study the evaporation rates of single droplets of dibutyl sebacate by Davis and Ray.¹⁹⁵ EDB's are typically designed using two hyperboloidal electrodes along with a central ring electrode. When an AC voltage is applied, an electric field with a "null

point” is created. A charged particle can be held at this null point by a DC field, which counters the gravitational force.^{195,196} One disadvantage of the EDB is that particles must be charged. It is not clear how the charge may affect, for example, the freezing dynamics of particles.^{197,198} Another disadvantage is the size of particles that can be stably trapped. Theoretically, particles ranging in size from 0.1-100 μm should be stably trapped within the EDB.¹⁹⁶ In practice, experiments are typically for particles on the order of a few microns, and though particles in the nanometer range can be trapped, these experiments are typically conducted under vacuum.¹⁹⁹ Additionally, due to the large AC field that must be applied, particles are not generally very well confined,¹⁹⁹ which could be problematic for the characterization of the particles (smeared scattering patterns).

Acoustic levitation is another technique that can be used to study single aerosol particles. It uses standing acoustic waves to trap particles via an acoustic radiation pressure.¹⁹⁹ Acoustic levitation is widely applicable to many different types of materials, e.g. insulators, magnetic, etc. However, only large particles (50 μm to 2 mm) are typically trapped under ambient pressures. It is possible to trap smaller particles (0.1-10 μm), but this involves increasing the chamber pressure to 2 atm.²⁰⁰ The possibility of trapping submicron particles in an acoustic chamber has been investigated.¹⁹⁹ However, it was found that particles may experience a drifting motion and that the trapping volume is broadened by Brownian motion. Particle movement could complicate characterization methods, such as scattering measurements. As well, acoustic levitation can be more difficult in gaseous media as compared to liquids, especially for solid particles.

Other optical trapping techniques include optical levitation and optical tweezing. Optical levitation occurs at a point in a vertical Gaussian beam (unfocussed) where the light forces on the particle balance against the force of gravity.²⁰¹ A lateral gradient force maintains the particle laterally within the trapping beam. This lateral restoring force is comparatively weak, which means that

particles are in general less stable in the trap in comparison to other trapping methods (e.g. optical tweezers). The optical tweezing technique (described in Section 5.1.1) uses a high numerical aperture objective (short working distance) to focus the Gaussian laser beam. This creates a trapping region that is more stable, but that is typically only a few tens of microns away from the objective.

The CPBB optical trap offers distinct advantages over other trapping methods. The majority of other single particle techniques are generally suited to trapping particles that are on the order of a few microns or larger. Previous studies have shown that submicron sized aerosol particles can be stably trapped in a CPBB optical trap,^{92,94,96,190} and submicron particles may be very important in atmospheric processes. Particles can be trapped far from any surfaces (a few centimeters) and optical components. When using a low temperature trap, this minimizes temperature gradients (and thus convection) in the trapping region. This also allows for an accurate reading of the temperature in the trapping region for freezing studies. As well, there are no pressure gradients within the trapping cell, and trapping can be performed at atmospheric pressure.

The study of particles in a temperature controlled environment requires a specialized trapping cell and vacuum chamber to maintain a constant temperature in the region of trapped particles (see Section 2.3.2). The use of the CPBB optical trap facilitates the implementation of this type of equipment, since the particles are not required to be near an objective (as for optical tweezers) or other surfaces. This leads to the opportunity to study aerosols at a variety of temperatures at sizes into the submicron regime.

5.2 Optical trapping at room temperature

Experiments for single aerosol particles trapped in the CPBB optical trap were initially performed at room temperature. These experiments illustrate the types of comparatively straightforward studies that are possible at room temperature before focusing on the freezing experiments at low temperatures in Section 5.3. Room temperature experiments for single aerosol particles were performed to study the possibility of relative humidity (RH)-induced glassy aerosol formation. Previous work in the group has focused on the study of aqueous sucrose aerosols in the CPBB optical trap.⁹⁶ This section discusses experiments for glucose, fructose and raffinose aerosols under similar experimental conditions as in the work of Lu et al.⁹⁶

5.2.1 Motivation

There has been recent interest in studying the formation and properties of glassy aerosols with atmospheric relevance.^{96,202-207} The formation of a glass would, for example, significantly inhibit the mass transfer of water and affect a particle's nucleating ability, which could greatly affect aerosol processes in the atmosphere (e.g. cloud formation).^{96,202-209} Glasses are amorphous solids (thermodynamically metastable) characterized by a dynamic viscosity, η , greater than 10^{12} Pa·s and the mechanical properties of a solid.^{202,204} Glass formation can occur by rapid cooling of a liquid below the glass transition temperature, T_g , or reducing the RH of the environment below the glass transition RH, RH_g , for an aqueous liquid at a sufficient rate.²⁰³ In either case, a disordered, non-equilibrium structure (rather than crystallization) results, along with a concomitant exponential increase of the viscosity.²⁰⁵ The values for T_g and RH_g may be highly dependent on the rate of change of each of these variables,²⁰³ (for example, reported T_g values for sucrose range from 319-348 K²⁰⁴) and thus a temperature or RH range may sometimes be reported.

Recent studies have shown that secondary organic aerosols (SOA) are likely to exist in a highly viscous ($\eta = 10^2$ - 10^{12} Pa·s) or glassy state in the atmosphere.^{208,209} SOA are formed in the atmosphere by chemical reactions to volatile organic compounds. They are highly prevalent in the Earth's atmosphere and can affect the planet's radiative balance. Carbohydrates are relatively simple molecules for studying the formation of glassy aerosols in the lab,⁹⁶ thus their use as a proxy for SOA. In addition, carbohydrates have been detected as components of atmospheric aerosols and are themselves of interest for atmospherically relevant experiments.²¹⁰⁻²¹⁵

Here, the focus is on RH-induced formation of highly-viscous or glassy aerosols for several aqueous carbohydrates. Particles are studied in a cell where the RH can be controlled at a constant temperature. A decrease in the RH of the environment induces water evaporation from the aqueous droplets and results in an associated decrease in particle size and increase in solute concentration. At high RH, the aqueous particle should be in equilibrium with the surrounding gas phase. As the RH is lowered toward the RH_g for the aqueous particle, the increasing concentration of the solute could lead to an increase in viscosity and a decrease in water diffusion within the particle. The particle could move out of equilibrium with the surrounding gas phase, potentially by formation of a highly viscous or glassy shell around the particle, trapping remaining water near the centre.^{204,216} In this case, the particle size in response to RH would differ from the expected RH-dependent equilibrium size.

In the current work, particle sizes are determined from the elastic light scattering phase functions (see Section 2.3.3.2) and are used to calculate hygroscopic growth factors (GF) and particle radius half-times ($t_{1/2}$) as a function of RH. The comparison of $t_{1/2}$ values at low RH (below the glass transition RH) to those at high RH can be used to infer if a viscous state has been formed. As well, deviations of the GF from theoretical equilibrium GF values can also serve as an indication of the

formation of viscous aerosols. The use of the CPBB optical trap provides the possibility to extend previous studies of glassy aerosols into the submicron regime. Studies of submicron particles are important to gain a better understanding of size-dependent effects for aerosols.

5.2.2 Sample preparation and experimental conditions

Aqueous solutions of glucose (350 g/L), fructose (400 g/L), or raffinose (200 g/L) were nebulized into the room temperature trapping cell as described in Section 2.3.1.3. Individual particles were trapped in the CPBB optical trap at a high RH ($\sim 70\%$) and allowed to equilibrate for two hours. A constant humidified N_2 flow was introduced to the trapping cell at a flow rate of 20-50 mL/min during both the initial equilibration time and the remainder of the experiment. The RH setting was then reduced in steps of 10% RH down to a setting of RH 0%; the RH was held constant at each step for approximately 60 minutes. Note that the RH setting and the RH reading for the cell (from the probes located before and after the cell, see Figure 2.5) typically differed by a few percent. The light scattered from the particle (perpendicular polarization) was collected during the duration of the experiment (as outlined in Section 2.3.3.1). Each phase function image is the average of approximately 10 frames per second (i.e. one image is saved per second).

5.2.3 Data analysis

5.2.3.1 Sizing of aqueous particles

Experimental phase functions were collected as outlined in Section 2.3.3.1. The particle sizes were calculated by fitting the experimental phase functions using Mie theory (see Section 2.3.3.2). The elastically scattered light was recorded as 1 image/s (the average of approximately 10 frames) and the particle size was determined for each of these phase function images.

In the current room temperature measurements, the aqueous carbohydrate particles are studied with respect to RH. When the RH in the cell is reduced, water from the aqueous particle will evaporate leading to a decrease in particle size and a corresponding increase in concentration. A change in RI occurs for the aqueous particles with the decrease in particle size since the RI is concentration dependent.⁹⁴ When performing the fits to the experimental phase functions, the LabVIEW program varies the particle radius. The variation in radius thus implies a change to particle concentration and RI. The exact relationship requires the parameterization of the RI as a function of concentration (referred to as the “concentrative RI parameterization”) and the initial size, RI, and the concentration (in g/L) for the particle (taken for the equilibrated particle at RH 70% for 2 hours) as input parameters. The concentrative RI parameterization for each of the carbohydrates will be outlined in Section 5.2.4.

In Section 2.3.3.3, the overall error in the absolute particle radius was given as $r \pm 150$ nm. For the room temperature trapping experiments, the particle size is determined as a function of RH. While the error for the absolute particle size is quite large, the uncertainty for the change in particle radius with respect to RH is estimated to be approximately 10 nm or less.⁹⁶ This value is based on the uncertainty of the RI data and the error associated with the RH probe readings (RH $\pm 3.5\%$). For the GF and $t_{1/2}$ calculations (outlined in Section 5.2.3.2 and Section 5.2.3.3, respectively) used to analyze the particles, it is the change in particle size that is more important than the absolute size of particles. An example of the separation between the local minima in the error for different Mie sizing results can be found in Figure 2.10. The typical separation between the local minima is ~ 150 nm. For the analysis of particle size for the carbohydrate particles, the amount the particle size is allowed to vary from one frame to the next is constrained (typically a value of 20-40 nm is used). This means that only one local minimum is followed during the sizing calculations.

5.2.3.2 Growth factor calculations

Growth factors (GF) were calculated for the carbohydrate particles at each RH. These values were compared to theoretical GF calculated under the assumption that equilibrium is established for all RHs. Deviations from theoretical values may indicate the formation of a highly viscous or glassy state.

The diameter growth factor, GF_{dia} , (typically referred to as simply GF throughout this work) is derived from:^{96,203}

$$GF_{dia}(RH) = \frac{d_{wet}(RH)}{d_{dry}} \quad (5.12)$$

where d_{wet} is the diameter of the wet particle as a function of RH and d_{dry} is the diameter of the dry particle. The mass fraction of solute (MFS) was used to calculate the value for d_{dry} in combination with the particle size (d_{wet}) after equilibrating for 2 hours at RH 70%. The diameter GF can also be derived from:²⁰³

$$GF_{dia}(RH) = \sqrt[3]{\left(\frac{m_{wet}\rho_{dry}}{m_{dry}\rho_{wet}}\right)} = \left(\sqrt[3]{GF_{mass}(RH)}\right) \left(\sqrt[3]{\left(\frac{\rho_{dry}}{\rho_{wet}}\right)}\right) \quad (5.13)$$

where m_{wet} and m_{dry} are the wet and dry mass of the particle, respectively, ρ_{wet} and ρ_{dry} are the wet and dry density of the particle, respectively and GF_{mass} is the mass growth factor with respect to RH. The value for GF_{mass} can be calculated from:²⁰³

$$GF_{mass}(RH) = \frac{m_{wet}}{m_{dry}} = \frac{1}{MFS} \quad (5.14)$$

The MFS is typically calculated based on the water activity at a given RH. The water activity, a_w , and the RH are related (assuming equilibrium conditions) via:

$$RH = a_w \times 100\% \quad (5.15)$$

The theoretical GF_{dia} curve with respect to RH is calculated for each particle according to Equations (5.13) and (5.14) (i.e. based on the MFS and density with respect to RH, which assumes equilibrium conditions).

The parameterization for the relationship between RH and the MFS, as well as other concentration related parameters (e.g. density, RI), will be provided for each of glucose, fructose, and raffinose in Section 5.2.4.

5.2.3.3 Half-time calculations

Half-times ($t_{1/2}$) were calculated by fitting the sizing results for each stepwise RH decrease (e.g. 70% to 60%) according to a first-order exponential decay:

$$y = (y_0 - y_p) * \exp(-k_t(x - x_0)) + y_p \quad (5.16)$$

for all values of $x > x_0$. In Equation (5.16), x_0 is the time when the decay begins, y_0 is the initial value before the decay begins, y_p is the plateau after the decay, and k_t is the rate constant. This equation is illustrated in Figure 5.9.

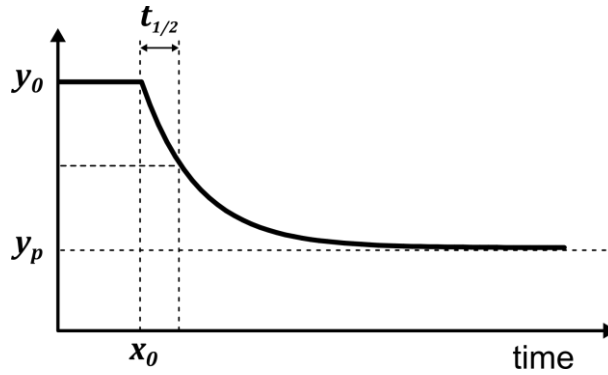


Figure 5.9: A first-order exponential decay according to Equation (5.16).

After determining the value for k_t , $t_{1/2}$ is calculated according to:

$$t_{1/2} = \frac{\ln(2)}{k_t} \quad (5.17)$$

The half-time is the time taken to reach the mid-size between the initial size (at RH_1) and the final size (at RH_2 , where $RH_2 < RH_1$). The half-times were also calculated for the response of each probe to the change in RH. Comparison between the particle half-times and probe half-times can indicate if there is formation of a highly viscous state.

The assumption that the decay is first-order is based on the first-order diffusion within a spherical droplet:⁹⁶

$$t_{D,1/2}(r) = \frac{r^2}{\pi^2 D_{drop} \ln(2)} \quad (5.18)$$

where $t_{D,1/2}$ is the diffusion half-time with respect to radius, r , and D_{drop} is the diffusion coefficient.

5.2.4 Concentrative refractive index parameterizations

The sizing of particles requires the parameterization of the RI as a function of concentration (referred to as the “concentrative RI parameterization”). RI data is typically available for carbohydrate particles at various concentrations. However, for our purposes, the RI must be determined in relation to the RH (the variable that is controlled in experiments). The RI parameterizations used to determine the particle RI with respect to RH are outlined in this section. These data are required for both the sizing of particles and the subsequent calculation of GF data. The methods used to calculate the required values for each of glucose, fructose, and raffinose are outlined below.

5.2.4.1 Glucose

The concentrative RI data for glucose (293.15 K, 589 nm) were taken from the CRC Handbook of Chemistry and Physics.²¹⁷ The RI vs. MFS data is plotted in Figure 5.10.

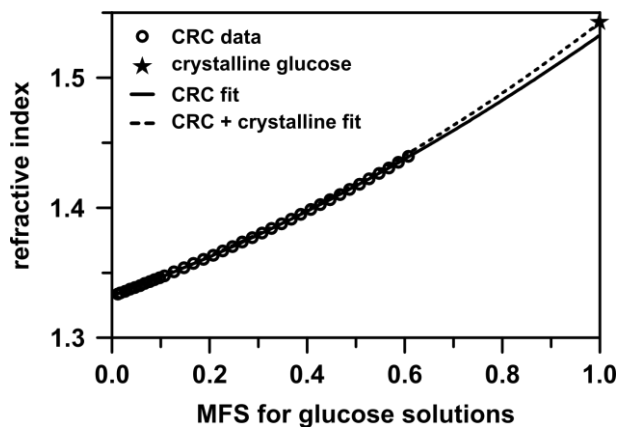


Figure 5.10: Refractive index data as a function of the mass fraction of solute (MFS) for aqueous glucose solutions. The concentrative data were taken from the CRC Handbook of Chemistry and Physics.²¹⁷ The crystalline glucose RI value was taken from the work of Cao et al.²¹⁸

A quadratic fit of the CRC RI vs. MFS data in Figure 5.10 yields:

$$RI = a_1(MFS)^2 + a_2(MFS) + a_3 \quad (5.19)$$

with $a_1 = 0.0624$, $a_2 = 0.1391$, and $a_3 = 1.3331$. A second fit was performed including a RI value for crystalline glucose,²¹⁸ however, the fit to solely the CRC data is what is used in the remainder of this work (see discussion in Section 5.2.5.1 for justification).

The MFS parameterization was taken from Peng et al.²¹⁹ to determine the MFS with respect to RH.

The MFS for glucose was calculated with respect to a_w according to:

$$MFS = b_1 + b_2 a_w + b_3 a_w^2 + b_4 a_w^3 + b_5 a_w^4 + b_6 a_w^5 \quad (5.20)$$

with $b_1 = 1.0025$, $b_2 = -0.3066$, $b_3 = 3.6075$, $b_4 = -15.335$, $b_5 = 22.043$, and $b_6 = -10.932$.

Equation (5.20) is valid at 298 K over the range $0.05 < a_w < 0.98$. The relation between the water activity and the RH was provided in Equation (5.15) and thus the combination of Equation (5.19) and Equation (5.20) allow for the calculation of RI with respect to RH.

To change the RI with respect to particle size during the particle sizing process, the concentration of the particle (in g/L) at the initial RH is required. This concentrative data for glucose was also taken from the CRC Handbook of Chemistry and Physics²¹⁷ and the data is plotted in Figure 5.11.

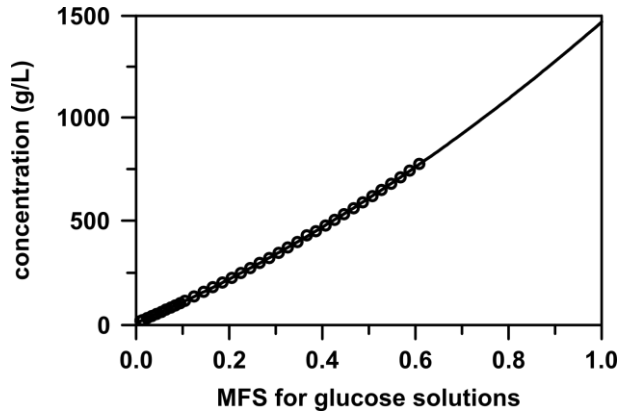


Figure 5.11: Concentration as a function of the mass fraction of solute (MFS) for aqueous glucose solutions. The concentrative data were taken from the CRC Handbook of Chemistry and Physics.²¹⁷

A quadratic fit of the glucose solution concentration (C_{soln}) vs. MFS data in Figure 5.11 yields:

$$C_{soln} = c_1(MFS)^2 + c_2(MFS) + c_3 \quad (5.21)$$

with $c_1 = 504.707$, $c_2 = 971.070$, and $c_3 = 1.090$. This equation can then be used to calculate the particle concentration at a given RH in combination with Equation (5.20).

The density (ρ) for aqueous glucose in relation to the MFS was taken from the CRC Handbook of Chemistry and Physics²¹⁷ (Figure 5.12). A quadratic fit to this data gives:

$$\rho = d_1(MFS)^2 + d_2(MFS) + d_3 \quad (5.22)$$

with $d_1 = 0.1545$, $d_2 = 0.3736$, and $d_3 = 0.9985$.

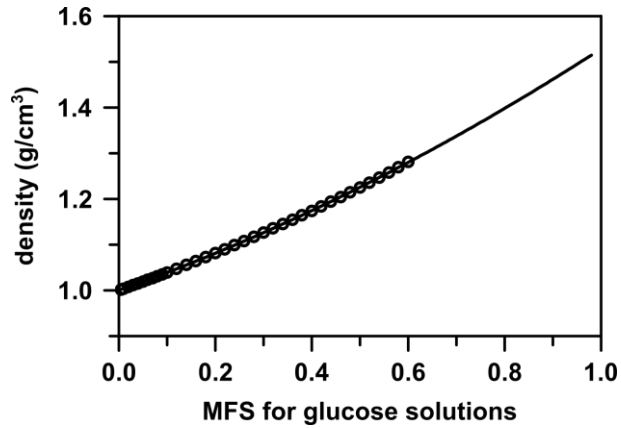


Figure 5.12: Density as a function of mass fraction of solute (MFS) for aqueous glucose solutions. The concentrative data were taken from the CRC Handbook of Chemistry and Physics.²¹⁷

5.2.4.2 Fructose

For fructose, a combination of concentrative data for the water activity as a function of MFS were taken from the work of Correa et al.,²²⁰ Lericci et al.,²²¹ and Gharsallaoui et al.²²² These data are plotted in Figure 5.13.

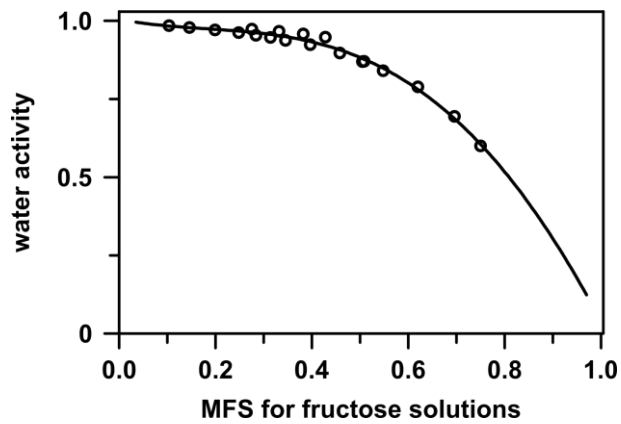


Figure 5.13: Water activity as a function of mass fraction of solute (MFS) for aqueous fructose solutions. The concentrative data were taken from the work of Correa et al.,²²⁰ Lericci et al.,²²¹ and Gharsallaoui et al.²²²

The data in Figure 5.13 were fit to a polynomial function to yield:

$$a_w = e_1(MFS)^4 + e_2(MFS)^3 + e_3(MFS)^2 + e_4(MFS) + e_5 \quad (5.23)$$

where $e_1 = 0.4655$, $e_2 = -2.1631$, $e_3 = 0.9799$, $e_4 = -0.2100$, and $e_5 = 1.0068$, and used to determine the MFS with respect to RH (see Equation (5.15)).

The concentrative RI data for fructose (293.15 K) were taken from the CRC Handbook of Chemistry and Physics.²¹⁷ The RI values are the same for fructose as for glucose, but provided over a slightly smaller range. The fructose RI data were plotted with respect to MFS (refer to Figure 5.10 for the data for glucose) and fit according to:

$$RI = f_1(MFS)^2 + f_2(MFS) + f_3 \quad (5.24)$$

where $f_1 = 0.0612$, $f_2 = 0.1393$, and $f_3 = 1.3331$.

A fit of the concentration vs. MFS data (Figure 5.14) gave the following:

$$C_{soln} = g_1(MFS)^2 + g_2(MFS) + g_3 \quad (5.25)$$

with $g_1 = 494.39$, $g_2 = 978.09$ and $g_3 = 0.7233$. Equation (5.25) can be used to relate the concentration to the RH via Equation (5.23).

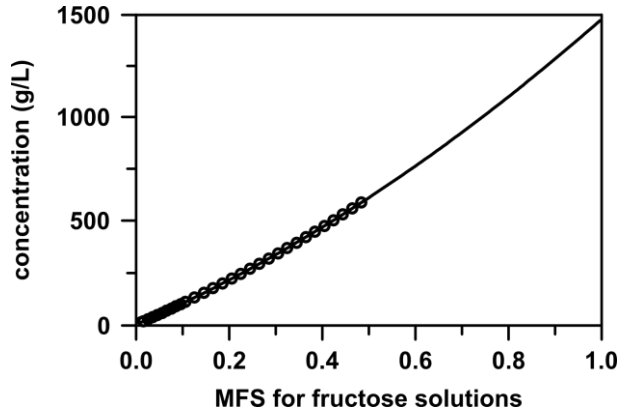


Figure 5.14: Concentration as a function of the mass fraction of solute (MFS) for aqueous fructose solutions. The concentrative data were taken from the CRC Handbook of Chemistry and Physics.²¹⁷

The relationship between the density (ρ) and MFS for aqueous fructose was taken from the CRC Handbook of Chemistry and Physics.²¹⁷ The data are shown in Figure 5.15.

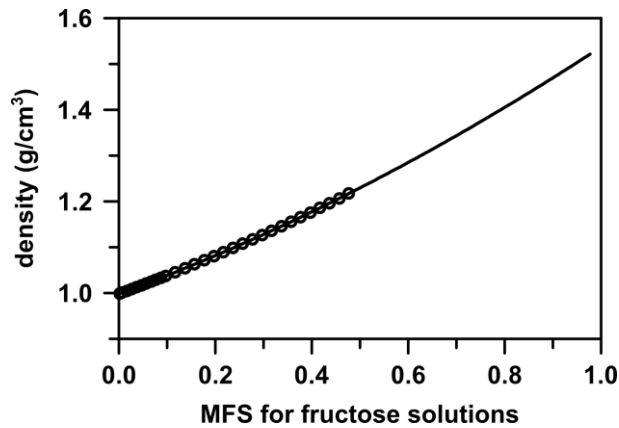


Figure 5.15: Density as a function of mass fraction of solute (MFS) for aqueous fructose solutions. The concentrative data were taken from the CRC Handbook of Chemistry and Physics.²¹⁷

A quadratic fit to the density data for fructose yields:

$$\rho = h_1(MFS)^2 + h_2(MFS) + h_3 \quad (5.26)$$

with $h_1 = 0.1528$, $h_2 = 0.3852$, and $h_3 = 0.9984$.

5.2.4.3 Raffinose

The parameterization of Zobrist et al.²⁰⁵ was used to calculate the water activity based on the MFS for raffinose according to:

$$a_w = \frac{(1 + i_1(MFS))}{(1 + i_2(MFS) + i_3(MFS)^2)} \quad (5.27)$$

$$+ (T - T^\theta)(i_4(MFS) + i_5(MFS)^2 + i_6(MFS)^3 + i_7(MFS)^4)$$

where T is the absolute temperature (292.15 K in this work), and $T^\theta = 298.15$ K. The coefficients take on the values as follows: $i_1 = -1$, $i_2 = -1.0035$, $i_3 = 0.1206$, $i_4 = 0.0005149$, $i_5 = -0.000263$, $i_6 = 0.002451$, and $i_7 = -0.002698$. Equation (5.27) is valid across the entire concentration range and from 160-313 K.

The concentrative data for raffinose was taken from the work of Lienhard et al.²²³ Figure 5.16 shows a plot of the RI with respect to MFS.

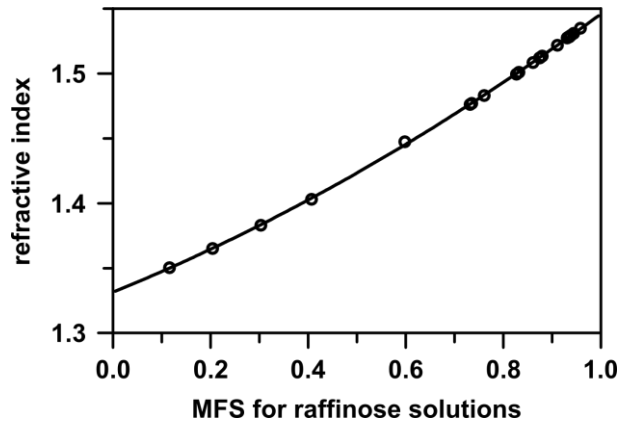


Figure 5.16: Refractive index data as a function of the mass fraction of solute (MFS) for aqueous raffinose solutions. The concentrative data were taken from the work of Lienhard et al.²²³

The RI data in Figure 5.16 were fit according to:

$$RI = j_1(MFS)^2 + j_2(MFS) + j_3 \quad (5.28)$$

where $j_1 = 0.0614$, $j_2 = 0.1531$, and $j_3 = 1.3314$. Equations (5.27) and (5.28) were used to calculate the RI with respect to RH (along with Equation (5.15)).

The concentration data (Lienhard et al.²²³) was plotted with respect to MFS in Figure 5.17.

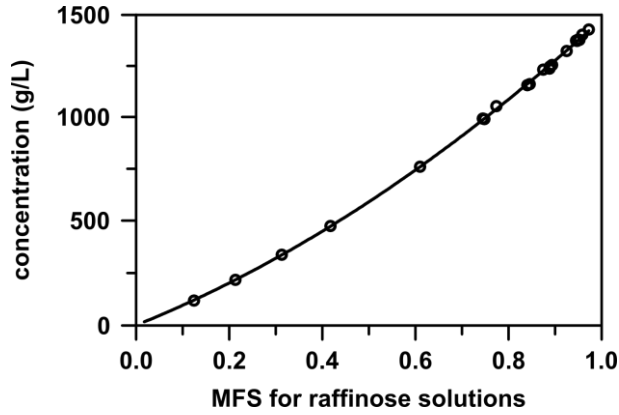


Figure 5.17: Concentration as a function of the mass fraction of solute (MFS) for aqueous raffinose solutions. The concentrative data were taken from Lienhard et al.²²³

A polynomial fit to the concentration data in Figure 5.17 gave:

$$C_{soln} = k_1(MFS)^2 + k_2(MFS) + k_3 \quad (5.29)$$

with $k_1 = 579.69$, $k_2 = 920.81$, and $k_3 = 8.534$.

The density for aqueous raffinose with respect to MFS (Figure 5.18) was obtained from the work of Lienhard et al.²²³ A plot of density (ρ) vs. MFS gives:

$$\rho = l_1(MFS)^2 + l_2(MFS) + l_3 \quad (5.30)$$

with coefficients $l_1 = 0.0761$, $l_2 = 0.4454$, and $l_3 = 0.9895$.

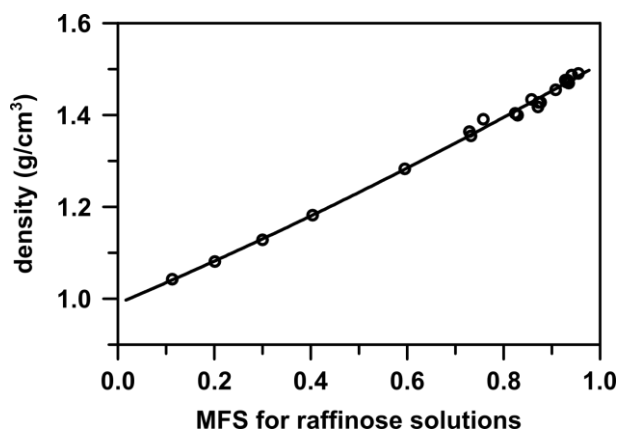


Figure 5.18: Density as a function of mass fraction of solute (MFS) for aqueous raffinose solutions. The concentrative data were taken from the work of Lienhard et al.²²³

5.2.5 RH-induced effects on single aqueous carbohydrate particles

Previous work in our group has studied the onset of a viscous state in response to a decrease in the RH for single micron and submicron-sized sucrose particles in a CPBB optical trap at room temperature.⁹⁶ This section presents preliminary experiments for three additional carbohydrate aerosol particles under similar experimental conditions: glucose, fructose, and raffinose. Raffinose is known to have a RH-induced glass transition at room temperature^{203,205} while glucose and fructose are not expected to form a glassy state at low RH. For all experiments, the room temperature was approximately 292 K.

5.2.5.1 Glucose

In this section, aqueous glucose particles are examined in the CPBB optical trap at room temperature to examine possible RH-induced effects on the single particles. Glucose is not expected to have an RH-induced glass transition at room temperature. Simperler et al.²²⁴ provide

experimental glass transition temperatures (T_g) for glucose of $T_g = 295$ - 296 K. The effect of RH on the value of T_g is generally to decrease the value of T_g compared to the dry value. The reported values of T_g are generally the value for the dry compound (i.e. at or near RH 0%) and thus indicate the highest temperature that a glass transition can be expected across the entire range of RH.²⁰⁴ In other words, in order to observe a RH-induced glass transition at room temperature in our CPBB optical trap setup, the T_g for the (dry) substance would need to be sufficiently higher than room temperature (depending, of course, on the exact relation between T_g and RH for the substance). Since the T_g for glucose is reported to be near room temperature (~ 293 K), an RH-induced glass transition is unlikely to be observed with the current experimental setup.

About a dozen glucose particles were studied in the CPBB optical trap. The initial size for trapped particles (i.e. equilibrated at RH 70%) ranged from approximately $r = 950$ - 2350 nm. The RH-induced decrease in particle radius typically ranged from 120-200 nm from RH 70% to RH 0%. This section will focus on a couple of the best glucose particle measurements. Experiments continued for as long as particles remained stably trapped. For the experiments not included here, particles were either lost at a mid-range RH (e.g. 40%) or there were errors in the way that the particle phase functions were recorded (e.g. if a particle was very unstable or moved from the initial trapping position) leading to difficulty in sizing these particles.

The effect of RH on single glucose particles has previously been studied in an EDB.²¹⁹ While bulk measurements for glucose have indicated that glucose should crystallize from a saturated solution, single particles did not crystallize or deliquesce in the EDB. Rather, reversible absorption and desorption of water was observed and at low RH ($\sim 5\%$), glucose particles were determined to be near water-free (i.e. high MFS). In the current work, no indications of particle crystallization were observed for any aqueous glucose particle experiments between RH 70% and 0%. It is expected

that there would be a change to the scattering phase function for crystalline particles compared to liquid or amorphous particles. These changes are discussed in further detail in Section 5.3 in the discussion of particle freezing observations. Briefly, crystallization is characterized by an irregular scattering pattern and an increase of the scattering intensity.

Figure 5.19 shows examples of the light scattering images from one glucose particle experiment. The images show the scattering from the particle at the start of the measurement (RH 70%) and at the end of the measurement (RH 0%). During experiments, there was typically a noticeable change in the scattering phase functions for each decreasing RH step. The RH-induced change in particle size is evident due to the decrease in the number of stripes in the image at low RH (panels (a) and (d)). The accompanying phase function plots show the quality of the Mie fits for this experiment (panels (b) and (e)) and that each Mie fit is that with the lowest calculated error (panels (c) and (f)).

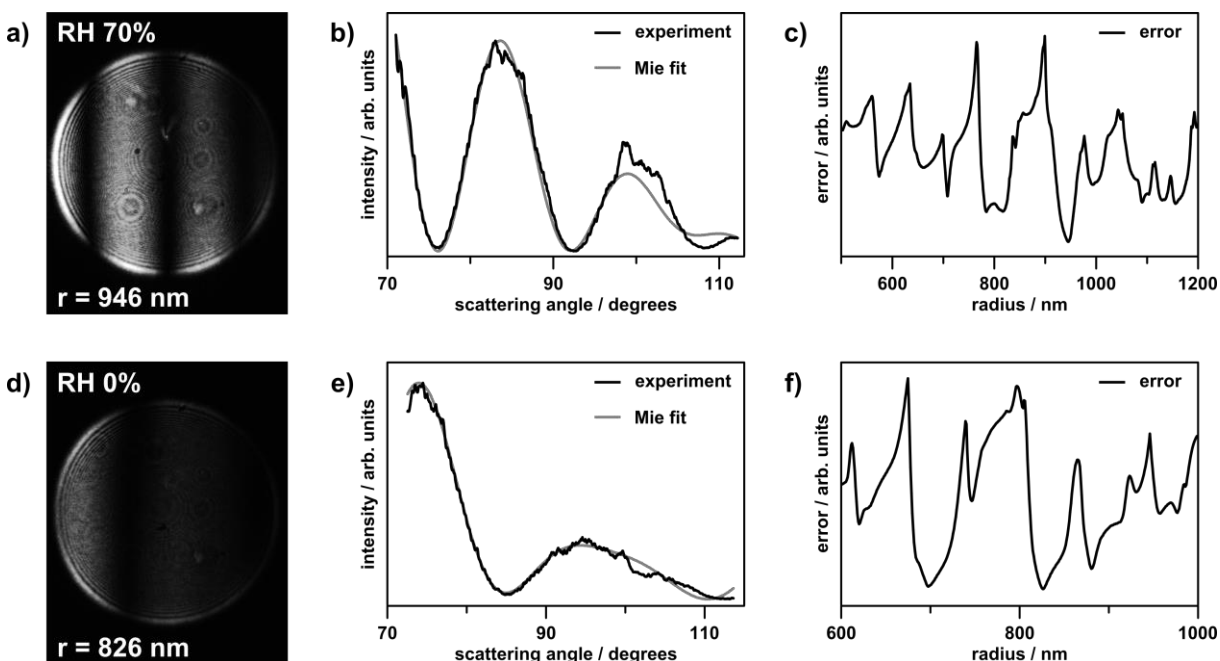


Figure 5.19: Light scattering data for a glucose particle during one experiment where RH was decreased from 70% to 0% (in steps of 10%). a) The scattering image, b) experimental phase function and best Mie fit, and c) error for the possible sizes for the glucose particle at RH 70%. d) The scattering image, e) experimental phase function and best Mie fit, and c) error for the possible sizes for the same glucose particle at RH 0%.

The remainder of this section will focus on experiments for two glucose particles. For these experiments, data are shown for particles trapped over approximately 9 hours. The data for each of these particles are shown in Figure 5.20 and Figure 5.21. The phase function images shown in Figure 5.19 correspond to the experiment in Figure 5.20. Panel (a) in each of Figure 5.20 and Figure 5.21 show the change in the RH (left y -axis) and the corresponding particle radius (right y -axis) with respect to time. These two particles were each initially at different sizes ($r = 949 \text{ nm}$ and $r = 1937 \text{ nm}$). After equilibrating at RH 70% for approximately 2 hours (scattering images were not recorded for the full time at RH 70%), the RH in the cell was decreased to 0% in steps of

10%. The particles remained at each RH step for approximately 1 hour. A stepwise decrease in particle radius can typically be observed each time the RH of the cell is reduced. Note that panel (a) in each of these figures shows the sizing result for only one phase function per 30 seconds due solely to the quantity of data for each experiment (1 image/s, i.e. tens of thousands of phase function images per experiment). However, for each experiment, all images were sized and used in the subsequent analyses.

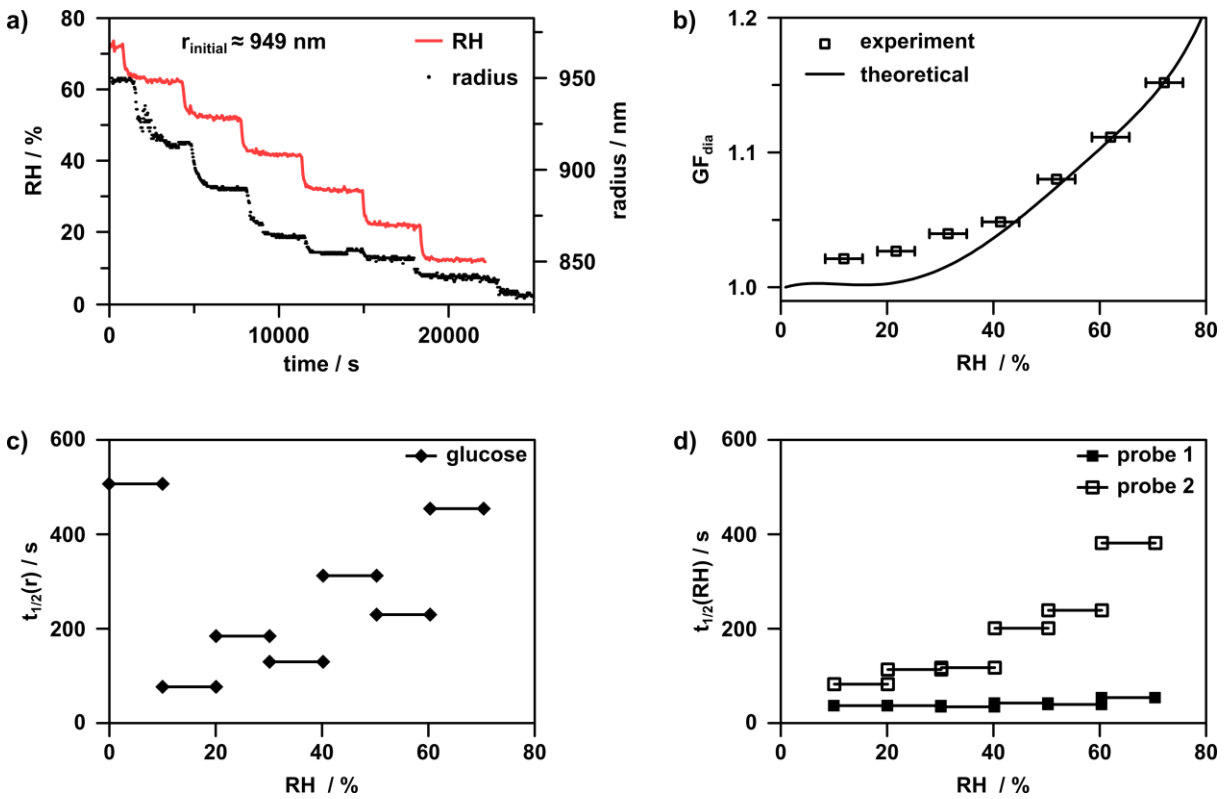


Figure 5.20: a) The decrease of particle radius and change in RH with respect to time for a glucose particle with initial size $r = 949$ nm. The particle was equilibrated at RH 70% for 2 hours. Note, due to a computer error, RH data was not recorded for the change to RH 0%. b) The experimental and theoretical growth factors for the particle in panel (a). c & d) The calculated half-times for the change in particle radius with respect to RH (c) and the response of each probe to the change in RH (d) for the data in panel (a).

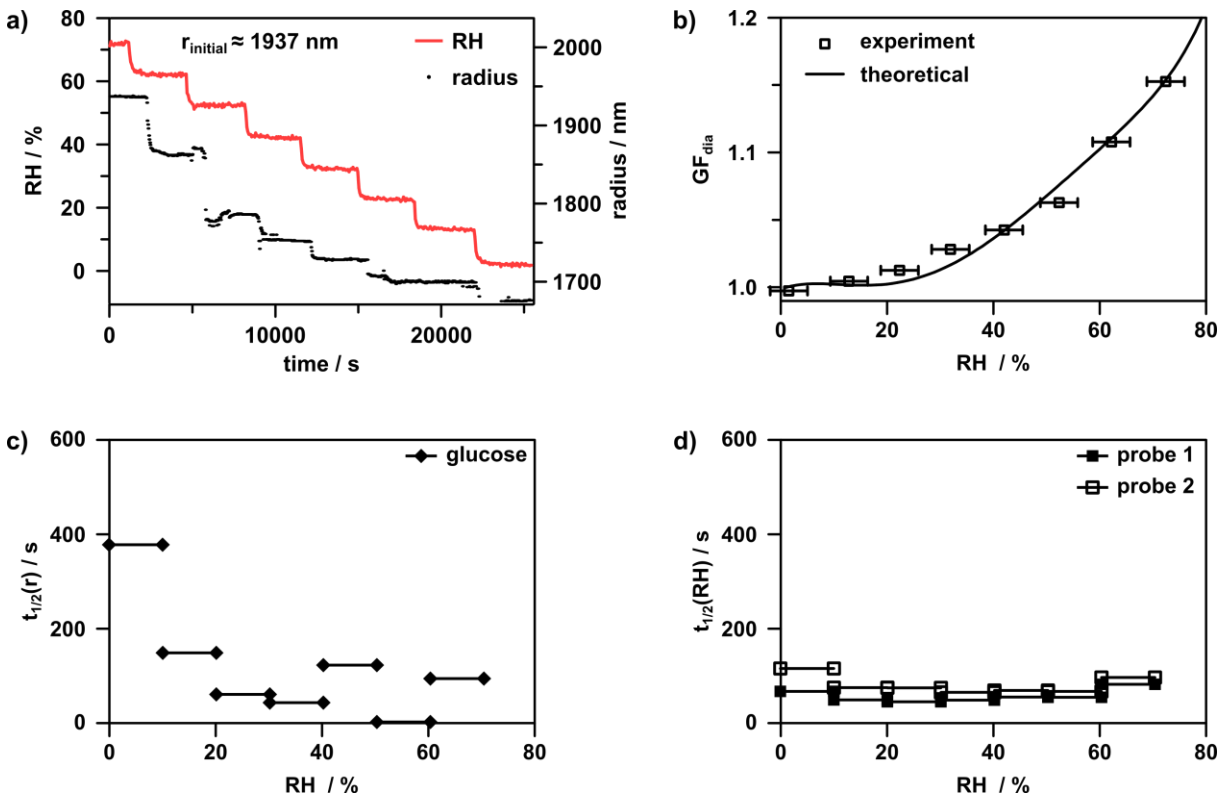


Figure 5.21: a) The decrease of particle radius and change in RH with respect to time for a glucose particle with initial size $r = 1937$ nm. The particle was equilibrated at RH 70% for 2 hours. b) The experimental and theoretical growth factors for the particle in panel (a). c & d) The calculated half-times for the change in particle radius with respect to RH (c) and the response of each probe to the change in RH (d) for the data in panel (a).

In Section 5.2.4.1, two quadratic fits for the glucose RI vs. MFS were shown: one for the CRC data over a MFS range of 0.0-0.6 and one for the same CRC data including a RI value for bulk crystalline glucose (i.e. MFS = 1.0). However, the fit to only the CRC data was used throughout this work.

Previous work by Lu et al.⁶ for sucrose particles compared the use of the two different types of fits (specifically, a fit of CRC RI data over a MFS range of ~ 0.1 -0.8 and a fit of the same CRC data including a RI value for bulk crystalline sucrose). While the sucrose RI fits were slightly different

above a MFS of 0.8, they found that the phase function sizing results using the two different RI fits were essentially identical. Additionally, the calculated GF and $t_{1/2}$ values were similar using the two different RI fits (i.e. the determined onset of the highly viscous state in sucrose particles was not affected by the exact RI data used). The decision to only use one set of RI data for the glucose analysis was made based on this observation for sucrose. It is assumed that small differences for the RI data would not have a significant effect on the overall results (see, for example, Figure 2.12(b)). Additionally, the RI values for the bulk crystalline glucose and the extrapolated CRC glucose data to MFS = 1.0 are very similar ($n = 1.543$ vs. $n = 1.535$, respectively).

After sizing the particles, experimental diameter GF values were calculated. Comparison of the experimental GF values to the theoretical values can give insight as to whether a particle has deviated from being in equilibrium with the surrounding gas phase. Figure 5.22 shows an example of calculated and theoretical GF values for an aqueous NaCl particle, taken from the work of Lu et al.⁹⁶ Aqueous NaCl particles are expected to remain in equilibrium with the surrounding gas phase as they evaporate over the RH range of 75-45%, i.e. above the crystallization RH for NaCl of ~40%.²²⁵ As can be seen from Figure 5.22, there is very close agreement between the experimental and theoretical GF values, indicating that the particle is very likely in equilibrium with the surrounding gas phase at each step. This type of behavior can be used for comparison to the behaviour of the aqueous carbohydrate particles.

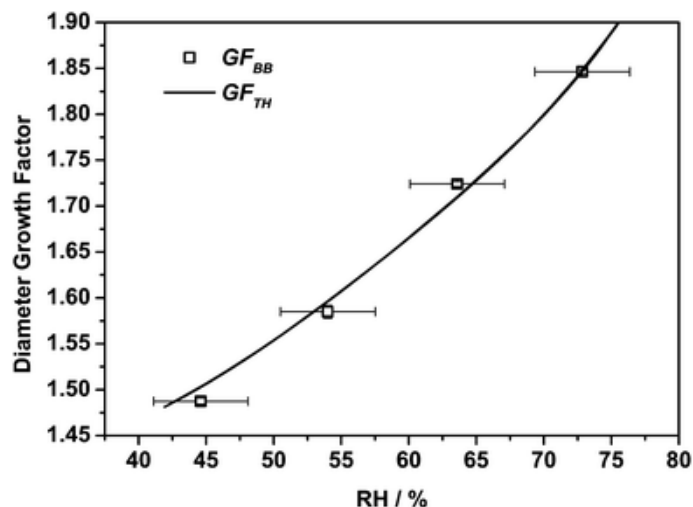


Figure 5.22: Experimental (GF_{BB}) and theoretical (GF_{TH}) diameter growth factors for aqueous NaCl particles as a function of RH. Uncertainty for the RH values is $\pm 3.5\%$ and uncertainty in the values of GF_{BB} is one standard deviation of the average of 50 data points taken at a certain RH (note the latter is of similar magnitude to the symbol size and thus difficult to see). The theoretical hygroscopic growth curve has been derived from the Clegg parameterization²²⁶ and the Clegg and Wexler solution density.²²⁷ Reproduced from *Phys. Chem. Chem. Phys.*, 2014, **16**, 9819–9830 with permission of the PCCP Owner Societies. <http://dx.doi.org/10.1039/C3CP54233E>

Values for GF were calculated for each glucose particle at each of the RH steps. The results are presented in panel (b) in each of Figure 5.20 and Figure 5.21 and are plotted in comparison to the calculated theoretical GF across the experimental RH range. In all GF figures, each experimental point is the average of the calculated growth factors for 50 data points at each RH. The error bars for the RH values are the error on the probes ($\pm 3.5\%$) and the error bars for the growth factor values are one standard deviation of the mean growth factor for the 50 phase functions. Note, the latter error is typically the same size (or smaller) than the data points on the plot and thus error bars are not easily visible.

For each glucose particle, the experimental GF are in good agreement with the theoretical curve from RH 70%-40% (typically within the error on each experimental point). Below RH 40% there are deviations from the theoretical values, in particular for the 949 nm particle. However, it is interesting to note that for the glucose particle in Figure 5.21, the calculated GF down to 0% correspond closely to the theoretical curve.

While deviation from the predicted GF value may imply the formation of a highly viscous state, it is only an indirect indication of such an event and thus cannot be used as the sole assignment of glassy aerosols formation. The GF calculations offer no insight into the kinetics of the evaporation process. Had particles remained at each RH step for a longer period of time, the experimental GF points might correspond more closely to the theoretical curve. Previous work has shown that experimental growth factors for sucrose particles calculated 5000 s after an RH change correspond more closely to the theoretical values compared to growth factors calculated 2700 s after an RH change.⁹⁶ Lu et al.⁹⁶ also found that the RH history experienced by a sucrose particle can have an effect on the agreement of GF values to the theoretical curve. Similarly for bulk materials, Burnett et al.²²⁸ have found that the observed value for RH_g is dependent on the rate of RH change.

Note as well that the calculated GF values assume that particles are in equilibrium with the surroundings after 2 hours at RH 70%.⁹⁶ This is because the size of the equilibrated particles at RH 70% is used to calculate the size of the dry solute particles (d_{dry}), and the value of d_{dry} is required to calculate the experimental growth factor at each RH. If particles were not in fact in equilibrium with the surrounding gas phase at RH 70%, this could cause a gradual increase in the deviation from the predicted GF curve at lower RH.

Another issue to consider when analyzing the GF plots is the dependence of the GF data on the corresponding RH and size obtained at each RH. The GF values are plotted with respect to RH, and this assumes that the RH is well defined at all times. During experiments, the particle phase functions (and by extension particle sizes) are recorded using one personal computer (PC) while the RH probe readings are recorded using a second PC. The sizing results and RH readings must then be aligned manually with respect to time (e.g. as shown in Figure 5.20(a)). It is possible that the RH and radius data do not correspond exactly in time (i.e. differing by anywhere from seconds to minutes) and this could affect the accuracy of the GF plots. The magnitude of this error would be different for each particle since the data alignment is performed independently for each experiment. It would also depend on the amount of variation in the RH readings and particle sizing results. For several data sets, the alignment of the RH data with respect to particle size has been altered by a few hundred seconds to examine the change in the plotted GF values. However, in all cases, the effect of RH and particle radius alignment appeared to be minimal.

While the GF data cannot provide information about the kinetic aspects of the particle response to RH, calculating the half-times for the change in particle radius can be useful to study changes in the rate of evaporation. The half-time calculations are useful to compare the response of the particle to the response of the RH probes, both with respect to the change of the RH setting. The data points in the half-time plots represent the initial and final RH setting for each half-time value, consistent with previous presentations of this type of data.^{96,203} In general, the RH probe half-times either remain fairly constant at each RH step or the half-times decrease at the lower RH steps. The half-times calculated for probe 1 are generally less than those calculated for probe 2 due to the position of the probes relative to the flow of the humidified N₂ and the cell (probe 1 is positioned before the entrance to the trapping cell while probe 2 is located after the cell, refer to Figure 2.5). A dramatic

increase in the half-times for the particle radius at lower RH (compared to the half-times for the probes at the same RH step) could indicate the formation of a highly viscous state where water mass transport is hindered.

For each of the glucose particles, there is not a marked increase in the calculated half-times at low RH compared to those values at high RH. For the smaller particle (Figure 5.20(c)), the half-time for the RH change from 10% to 0% is a similar value as that for the RH change from 70% to 60%. For the larger particle (Figure 5.21(c)), there is an increase in the half-time for the last size change (RH 10% to 0%) compared to those at higher RH. However, the magnitude of this value is less than that calculated for the previous glucose particle at high RH. The calculated half-times for the glucose particles are generally larger than the half-times for the RH probes at each of the corresponding RH steps. However, there is no strong indication of a dramatic decrease in the rate of the decrease in particle size, i.e. the mass transport of water.

In comparison to previous work, the half-time for sucrose particles showed a dramatic increase at the low RH steps. In one sucrose experiment, the half-time for the RH step from RH 15% to RH 5% was approximately 2250 s, while the half-times at higher RH were on the same order as those calculated in this work for glucose.⁹⁶ Thus, it is unlikely that glucose aerosols have formed a highly viscous or glassy state in the current work since the timescales are not near those observed for the highly viscous sucrose particles.

There is error associated with each of the calculated half-times. These results depend more on the change in particle size for each RH change than the absolute particle size at each RH. As mentioned earlier, the error for the change in particle size is typically only ± 10 nm. Much of the error associated with the half-time values stems from the error in the exponential decay fits to the

experimental particle sizes. These fits depend on the quality of the sizing results and vary for each size change. For RH steps where there is a well-defined initial and final size (i.e. the particle size changes by only ± 1 -2 nm at the experimental RH), the quality of the fit is typically much greater than for those RH steps where there is more variation in the initial and final sizing results. Some segments of the sizing results contain more outlying points than others, also affecting the quality of the fits. It was sometimes necessary to indicate the time at which the decay started (x_0 , refer to Figure 5.9) in order to obtain a reasonable fitting result. As mentioned above, since the RH data and the particle phase functions are recorded on separate PCs, it is not possible to know the time that the RH was changed when setting the value for x_0 . Additionally, even if there was a clear alignment of the phase function and RH data, there is likely a delay (response time) between the start of the decrease of the RH within the cell and the onset of particle evaporation, and it is not clear exactly what this response time may be. The input value for x_0 would have an effect on the resulting half-time for the RH step. However, since the half-times for both the probes and the particles are typically of similar magnitude (i.e. on the order of a few hundred seconds), it is unlikely that there is formation of a highly viscous state for the glucose aerosols studied in this work. This is in agreement with our expectation that glucose would not undergo formation of a RH-induced glassy state.

5.2.5.2 Fructose

Experiments performed by Truong et al.²²⁹ found values of T_g for fructose of approximately 289-298 K. Because of the relationship between T_g and RH_g (see discussion in Section 5.2.5.1), no glass transition induced by a decrease in RH at room temperature is expected for fructose. Four fructose particles were studied in the CPBB optical trap. The fructose particles that were trapped

were often larger than the glucose particles, with initial sizes for fructose ranging from approximately $r = 1350\text{-}3050$ nm.

A fit to the CRC data for the fructose RI vs. MFS (over a MFS range of 0.0-0.5) was performed and used for all analysis in this work. The RI values provided for glucose and fructose in the CRC Handbook of Chemistry and Physics correspond exactly to one another. Since there was not a dramatic difference in fitting just the CRC glucose data versus fitting the CRC and crystalline glucose data (refer to Figure 5.10), no other data sets for fructose were considered.

The general trends for fructose particles were similar to those for glucose particles and thus much of the discussion for glucose can apply to the results present in this section. No indications of particle crystallization were observed for fructose particles. Figure 5.23 shows the data for a fructose particle presented in an analogous manner to the data for glucose particles (over an RH range of 70% to 10%). Note in Figure 5.23(a) that there are very few sizing results at RH 10%. This is due to the fact that the fructose particle had moved off camera for most of the time at this RH. This further limits the RH range to 70% to 20% for the GF and half-time data (Figure 5.23(b) and Figure 5.23(c) and (d), respectively). However, there were a few phase functions recorded at RH 10% and the sizing results at this RH are smaller than for RH 20%, indicating that the particle was still losing water down to RH 10%.

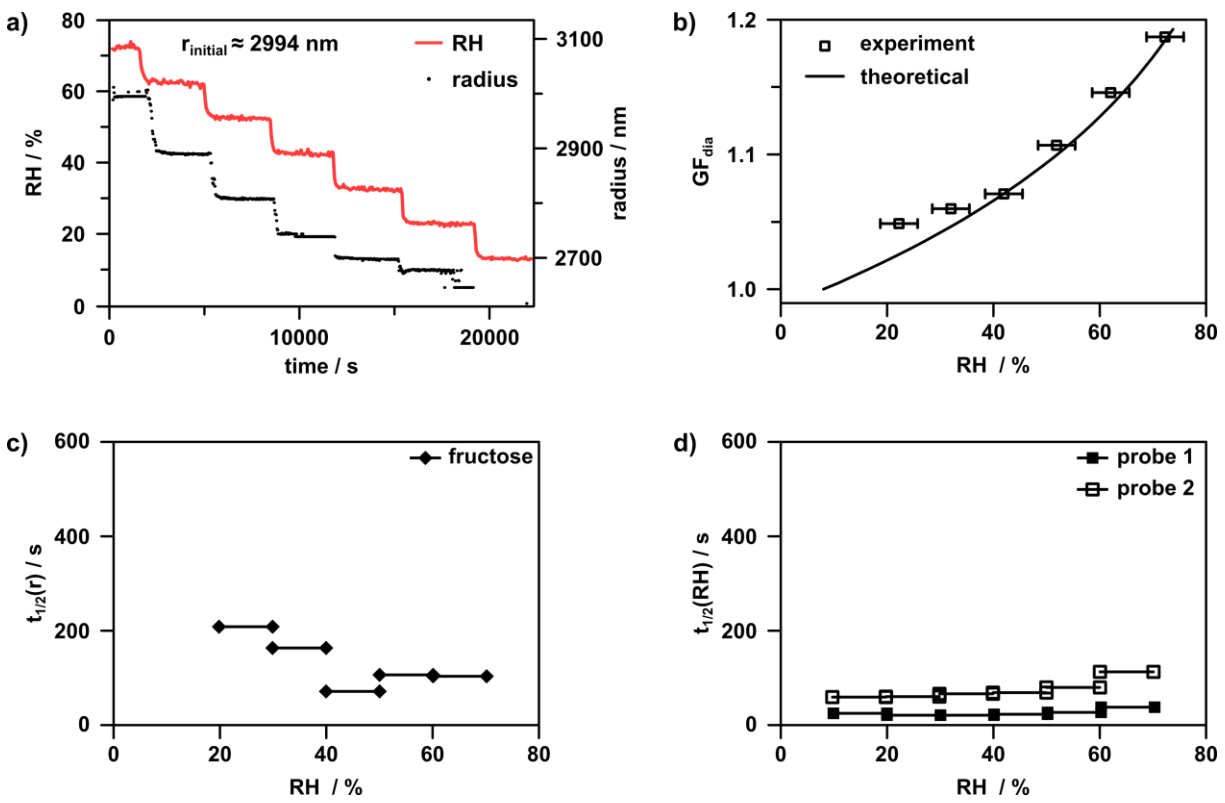


Figure 5.23: a) The decrease of particle radius and change in RH with respect to time for a fructose particle with initial size $r = 2994$ nm. The particle was equilibrated at RH 70% for 2 hours. b) The experimental and theoretical growth factors for the particle in panel (a). c & d) The calculated half-times for the change in particle radius with respect to RH (c) and the response of each probe to the change in RH (d) for the data in panel (a). Note, the particle had moved off of camera after the RH change to 10%. As a result, there are no calculated values for the GF_{dia} at RH 10% or for $t_{1/2}(r)$ for the change from 20% to 10%.

For the fructose particle, the calculated GF values deviate from the predicted equilibrium values at lower RH (30% and 20%). The magnitude of this deviation is similar to what was observed for glucose particles. The calculated half-times for the fructose particle do increase slightly at lower RH, but the values of the half-times are very similar to those calculated for glucose. The fructose particle does not show any clear evidence of glassy or highly viscous behaviour over the RH range

that has been examined (refer to the discussion of the results and errors for the glucose particles in Section 5.2.5.1). However, additional fructose particles should be examined (down to RH 0%) to be certain that there is not any indication of highly viscous behaviour at lower RH.

5.2.5.3 Raffinose

In contrast to glucose and fructose, raffinose should exhibit a glass transition at an RH of approximately 53% at room temperature.²⁰³ Tong et al.²⁰³ previously observed formation of a glassy state for coarse-mode ($r > 1 \mu\text{m}$) raffinose particles in an optical tweezer. In the current work, four raffinose particles were studied in the CPBB optical trap. All experiments were performed in the same manner as for the glucose and fructose particles. Initial particle sizes ranged from $r = 830\text{-}1300 \text{ nm}$. As for glucose and fructose, no indications of particle crystallization were observed.

The phase functions from one raffinose experiment are shown in Figure 5.24. The sizing results and subsequent GF and half-time calculations for the same raffinose particle are shown in Figure 5.25. This particle did equilibrate at RH 70% for 2 hours but the initial equilibrated size is not known (phase functions did not begin to be recorded until after the RH setting was changed to 60% for this particle).

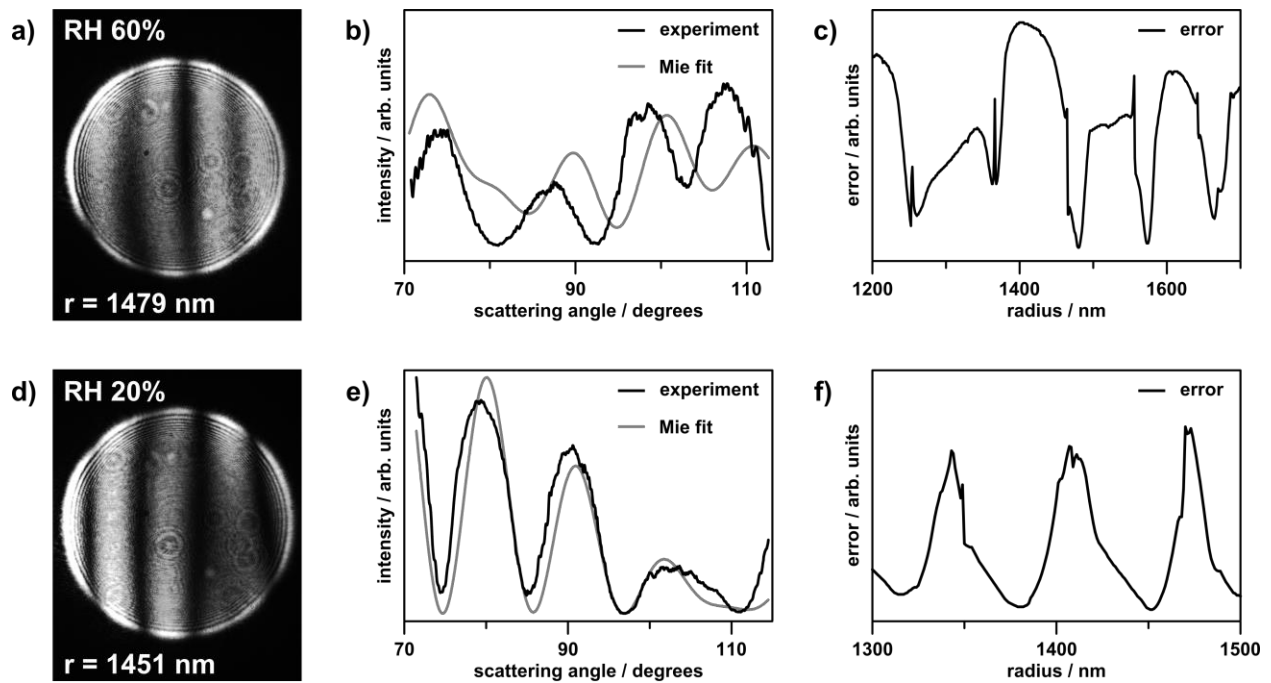


Figure 5.24: Light scattering data for a raffinose particle during one experiment where RH was decreased from 70% to 20% (in steps of 10%). a) The scattering image, b) phase function and Mie fit, and c) error for the possible sizes for the glucose particle at RH 60%. d) The scattering image, e) phase function and Mie fit, and c) error for the possible sizes for the same glucose particle at RH 20%.

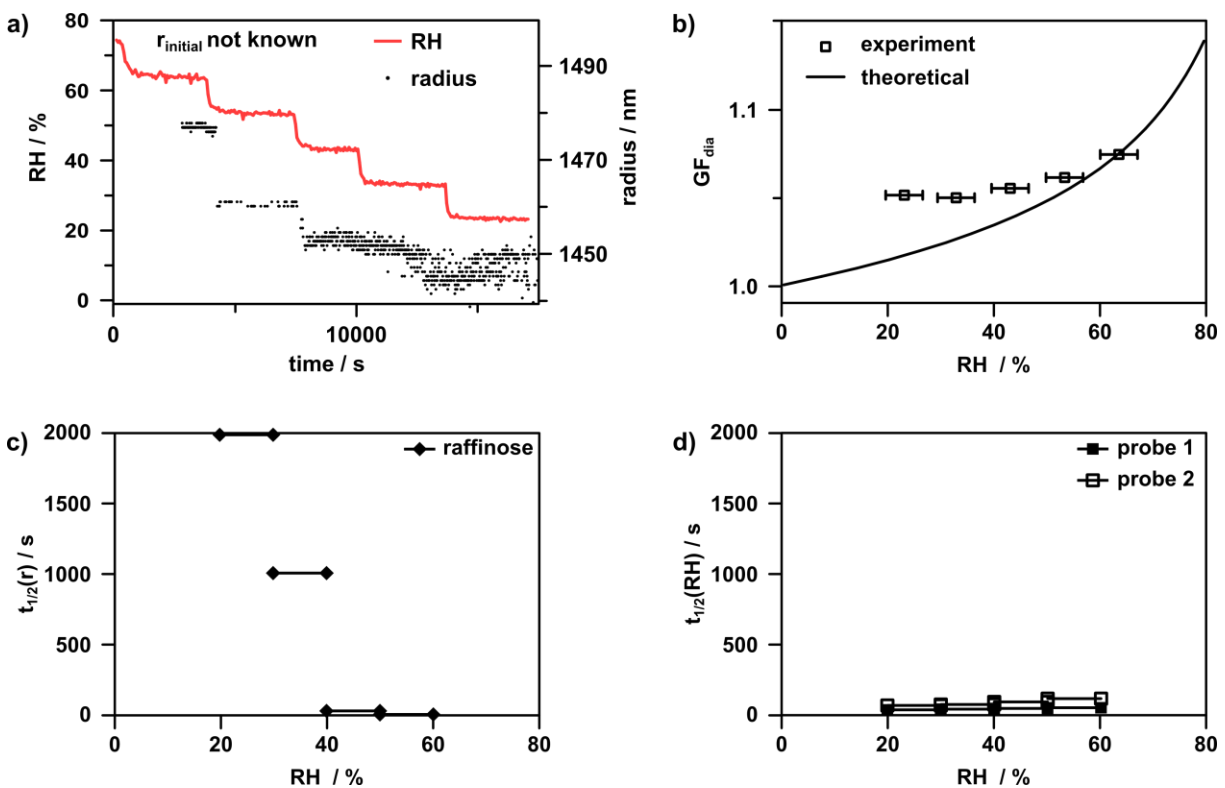


Figure 5.25: a) The change of particle radius and change in RH with respect to time for a raffinose particle. Note, the phase functions for this particle did not begin to be recorded until RH 60%. The particle equilibrated at RH 70% for 2 hours, but the initial particle radius at this RH is not known. b) The experimental and theoretical growth factors for the particle in panel (a). c & d) The calculated half-times for the change in particle radius with respect to RH (c) and the response of each probe to the change in RH (d) for the data in panel (a).

While this particle does not represent one for which we have an optimal data set (due to the lack of particle sizes at RH 70%), it is clear that the particle size response to RH change is not the same below RH 40% as above RH 40% (Figure 5.25(a)). Additionally, this is different from the sizing results typically observed for glucose (Figure 5.20 and Figure 5.21) and fructose (Figure 5.23) particles. For glucose and fructose particles studied in the previous sections, changes to the phase functions could typically be observed during the change from one RH to the next. Interestingly,

when the RH in the cell was change from 40% to 30% and from 30% to 20% for this raffinose particle, there were essentially no changes observed in the scattering pattern.

Figure 5.25(b) shows experimental and theoretical GF data for the raffinose particle. GF values were calculated for the raffinose particle in a slightly different manner than those for glucose and fructose. For this specific particle, sizing data is not available for the particle at RH 70% and the calculated value for d_{dry} was determined using the particle size at RH 60%. For this raffinose particle, the calculated GF values show a larger deviation from the theoretical curve compared to what was observed for both the glucose and fructose. The GF value at RH 20% is slightly higher than the value calculated at RH 30%.

The raffinose particle was analyzed in terms of the calculated half-times for the size decrease of the particle at each RH change. There is a dramatic increase in the half-time for the raffinose particle at low RH compared to the calculated values at high RH (Figure 5.25(b)) and the corresponding RH probe half-times (Figure 5.25(c)). Above 40%, the half-times are of similar value to those for glucose and fructose (note the difference in the values on the $t_{1/2}$ axis for raffinose compared to those for glucose and fructose). Below 40%, there is a dramatic increase in the half-time values compared to those at high RH, and also compared to those for glucose and fructose at the same RH. The half-time values at low RH are also very similar to what was observed for sucrose particles at low RH⁹⁶ and it is possible that raffinose particles form a glassy or highly viscous state as indicated by the decrease in water mass transport from the particle at low RH (below 40%). Raffinose particles are currently under further study within the research group. These experiments have also shown evidence of raffinose forming a highly viscous or glassy state at low RH.

5.2.6 Conclusions for room temperature trapping experiments

The previous experiments to study sucrose particle response to RH changes showed evidence of the formation of a highly viscous state below the RH_g for sucrose.⁹⁶ In this previous work, 15 RH dependent experiments were performed on sucrose particles of different sizes. Due to the limited amount of data presented here for each of glucose, fructose, and raffinose, it is difficult to draw clear conclusions for each of these aerosols in response to the RH of their surroundings. However, based on the current experiments, it seems likely that raffinose takes on a highly viscous or glassy state at low RH, while neither glucose nor fructose show such an increase in viscosity. It is, however, important to note that the GF and half-time calculations are used as indirect indicators of changes to particle viscosity.

It is known that a particle's history can have an effect on the calculated values in GF and half-time calculations. However, these effects are not currently fully understood and provide an area of glassy aerosol formation that requires further study. The CPBB extends the study of glassy aerosol formation in single aerosols into the submicron range. In the submicron size range, size-dependent effects may be extremely pronounced, and thus a thorough study of single glucose, fructose, and raffinose aerosols would require the study of multiple particles of a given size to accurately assess these effects.

One thing to consider with the optical trapping experiments is the trapping efficiency. Here, it is important to note that the efficiency may be different for different substances (i.e. glucose vs. fructose vs. raffinose). For example, the size of fructose particles that were trapped was generally larger than the size of glucose particles. The alignment of the Bessel beams in the trapping region is

vital for keeping particles trapped for long periods of time. A method for improving the general particle trapping efficiency in the CPBB optical trap will be discussed in Section 5.4.

5.3 Optical trapping at low temperatures[‡]

The optical setup for the room temperature experiments presented in Section 5.2 has been coupled to a low temperature trapping cell to allow for temperature controlled studies of freezing for single aerosol particles. Preliminary freezing studies were performed for micron and submicron-sized supercooled particles in the CPBB optical trap.

5.3.1 Motivation

In this section, preliminary experiments using a CPBB optical trap coupled to a temperature controlled trapping cell are presented. These first experiments show the types of studies that are possible for the new instrument design (described in Section 2.3.2), such as homogeneous and heterogeneous freezing, freeze-melt cycles, and evaporation of supercooled single particles (note, it is also possible to study solid particles in the low temperature trapping cell, though this is not considered in the current work). The particles are trapped far from surfaces of the cell, which can minimize temperature gradients, and thus convection that could lead to particle instability. Particles can remain stably trapped in the CPBB low temperature trap for hours, making this a tractable method for the study of freezing rates for submicron particles.

[‡]The majority of the work in this section has been published and excerpts are reprinted with permission from Review of Scientific Instruments, 2014, **85**, 095107. Copyright 2014, AIP Publishing LLC.

There are a number of previous single particle freezing studies that have been conducted. Many have used optical trapping techniques. A cooled optical trapping apparatus was developed by Anders et al.²³⁰ and used to study the freezing of supercooled water droplets^{230,231} and mixed water-sulfuric acid droplets²³⁰ trapped in a focused Gaussian beam. In this study, particles were only trapped for a few minutes. Mund and Zellner^{201,232} studied single supercooled, micron-sized mixed water-sulfuric acid droplets using optical levitation coupled to Raman spectroscopy. They were able to keep particles trapped on the order of hours. As well, supercooled water droplets^{198,233} and ice crystals¹⁹⁸ have been trapped using focused counter-propagating Gaussian beams by Tachikawa et al., while Ishizaka et al.²³⁴ have used optical tweezers to study the crystallization of aqueous ammonia sulfate droplets. In addition, freezing studies using other trapping techniques such as acoustic trapping (sulfuric acid/nitric acid freezing)^{235,236} and a quadrupole trap (sulfuric acid freezing)²³⁷ have been performed. The above studies all focus on micron-sized particles, i.e. $r \geq 2 \mu\text{m}$. Our current work seeks to extend the size range of single particle freezing studies into the submicron regime.

5.3.2 Data analysis

The particle phase functions were collected as described in Section 2.3.3.1. The particle sizes were determined using the LabVIEW program described in Section 2.3.3.2. The sizing of the hexadecane, dodecane and water particles studied in this section is less complicated than for the aqueous carbohydrate particles studied in Section 5.2 because the RI for each of these particles is constant at a given temperature (i.e. there are no RH induced concentration changes).

The scattered light from solid (crystalline) particles is quite irregular compared to that scattered by liquid particles and cannot be fit using the methods described in this work. This irregular

scattering pattern will be discussed in more detail throughout the low temperature trapping section. Thus, in this section, the only sizing results that are presented are for liquid particles. Any sizes that are given for particles that freeze refer to the particle size immediately before freezing occurs.

5.3.3 Freezing studies

The freezing studies presented in this thesis represent the preliminary studies performed in the low temperature CPBB optical trap. Further improvements to the setup will be required before an extensive study of the homogeneous freezing kinetics of single aerosols particles can be completed. The required improvements to the setup will be discussed in Section 5.4. The initial freezing studies focus on hydrocarbons (hexadecane and dodecane) and water.

5.3.3.1 Hexadecane

The majority of freezing experiments were performed on hexadecane. Hexadecane was chosen as a first test substance for freezing experiments due to its relatively high melting point (291.27 K)²¹⁷ and its low vapour pressure (approximately 2.94×10^{-4} mmHg).²³⁸ Hexadecane was nebulized into the low temperature cell and particles were initially trapped at 287.5 K. Freezing times were determined from 286.2-287.5 K, which represents supercooling of hexadecane by 3.8 -5.0 K. A constant dry N₂ flow was used during all hexadecane measurements. Before reaching the cell, the N₂ passed through a copper coil which was submerged in a refrigerated circulator unit at approximately 286.15 K. Initially, a flow of 4.0 mL/min was used to remove excess particles from the cell. Once only the trapped particle of interest remained in the cell, the flow was reduced as low as 0.25 mL/min.

The RI for hexadecane at our experimental wavelength and temperature was not available in the literature. A value for hexadecane under the current conditions was approximated from values available at other wavelengths and temperatures.²³⁹ The literature RI data at 632.8 nm was plotted with respect to temperature (over the range of 294-305 K), fit according to a second-order polynomial and extrapolated to approximately 284 K. A second polynomial expression (second-order) was derived from a single RI data point at 589.3 nm, assuming a similar relationship between RI and temperature at both wavelengths, and also extrapolated to approximately 284 K. Assuming a Cauchy relationship¹⁰⁸ between the RI and wavelength, a two-term Cauchy equation²⁴⁰ was used to calculate the RI at 532 nm based on the RI data at 632.8 nm and 589.3 nm according to:

$$n(\lambda) = B + \frac{C}{\lambda^2} \quad (5.31)$$

where n is the wavelength (λ) dependent RI and B and C are the Cauchy coefficients. The Cauchy coefficients were calculated from the extrapolated RI data to 284.2 K at both 632.8 nm and 589.3 nm according to:

$$B = n_1 - \frac{C}{(\lambda_1)^2} \quad (5.32)$$

$$C = \frac{(n_2 - n_1)(\lambda_1)^2(\lambda_2)^2}{(\lambda_1)^2 - (\lambda_2)^2} \quad (5.33)$$

The approximated RI for hexadecane at 532 nm and 284.2 K that is used in all analysis is $n = 1.445$.

As discussed in Section 5.1.3, optical binding (the simultaneous trapping of multiple particles) is possible in the CPBB optical trap. Figure 5.26 shows an image of two simultaneously trapped hexadecane particles (supercooled liquid droplets) at 287.4 K. This image shows the range in

particles sizes that can be trapped with the same Bessel beam core size. Interestingly, these two particles are roughly near the upper and lower size limits for hexadecane particles that have been trapped in the current setup. The large particle on the left in the image was sized at $r = 5386$ nm. The smaller particle on the right cannot be sized directly as no images were recorded that contain the entire scattering phase function. However, comparison to other scattering images that have been sized indicates that the size for this particle was likely around $r = 800$ - 900 nm. We have been able to simultaneously trap up to 10 particles in the current low temperature trap setup.

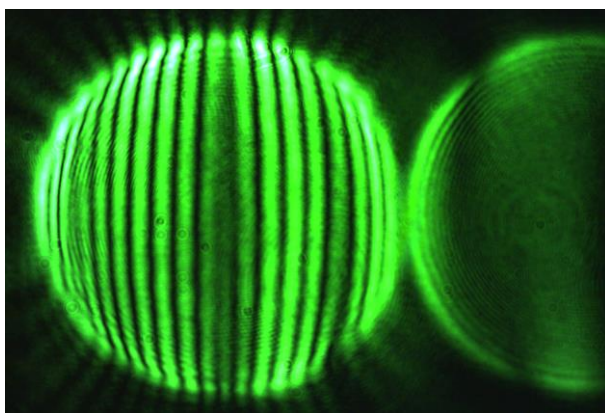


Figure 5.26: Image of the scattering phase functions for two supercooled liquid hexadecane droplets that were simultaneously trapped in the low temperature cell at 287.4 K.

Another example of optical binding in the low temperature trap is shown in Figure 5.27. In this image, two particles were simultaneously trapped at 287.5 K. This image is interesting because the particle on the left is frozen, while the particle on the right is a supercooled liquid particle. The particle on the left is deemed to be frozen because of the changes to the phase function that are known to occur upon freezing. These changes will be discussed in further detail later in this section. Briefly, the irregular scattering pattern, rather than the regular stripes seen for the particle on the right, is one indication that a particle is frozen.

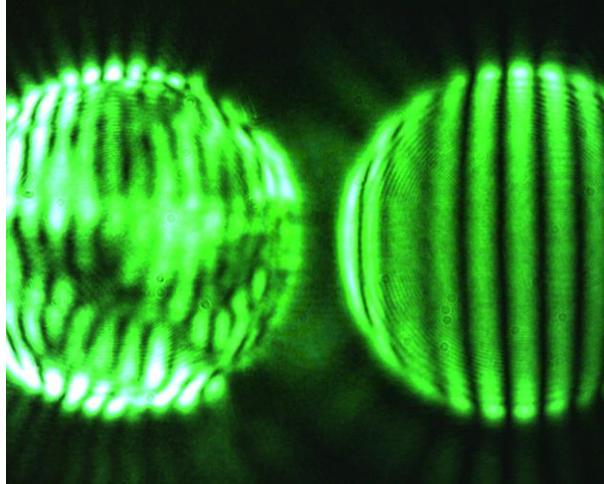


Figure 5.27: Image of the scattering phase functions for two hexadecane particles simultaneously trapped at 287.5 K in the CPBB optical trap. The particle on the left is frozen, while the particle on the right is a supercooled liquid droplet. Reprinted with permission from *Review of Scientific Instruments*, 2014, **85**, 095107. Copyright 2014, AIP Publishing LLC.

The goal for these initial studies was to look at the length of time for individual supercooled hexadecane particle to homogeneously freeze at a given temperature. The homogeneous freezing times for 18 supercooled hexadecane particles are plotted in Figure 5.28 for temperatures ranging from approximately 286.2-287.7 K. The freezing times represent the length of time that a particle was trapped at the stated temperature before freezing (all particles were initially trapped at approximately 287.5 K before the cell temperature was lowered to the desired temperature for a given experiment). The plot includes particles ranging in size from approximately $r = 800$ nm to $r = 5500$ nm.

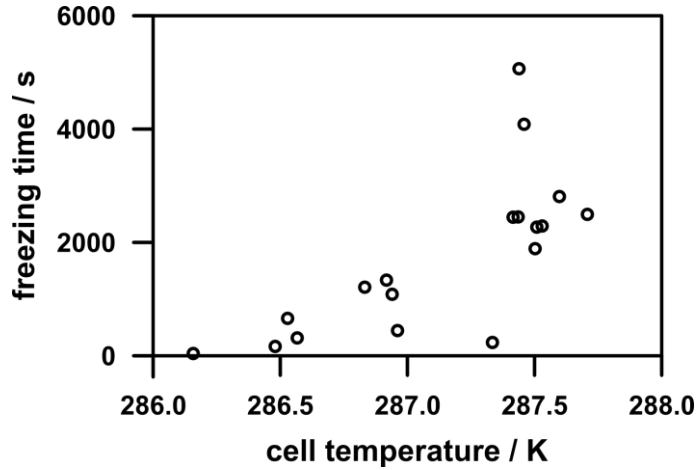


Figure 5.28: Homogeneous freezing times for supercooled hexadecane particles ($r = 800\text{-}5500\text{ nm}$) between 286-288 K. Reprinted with permission from *Review of Scientific Instruments*, 2014, **85**, 095107. Copyright 2014, AIP Publishing LLC.

On average, the particles freeze faster at the lower cell temperatures. This trend is expected due to the strong temperature dependence on the rates of homogeneous nucleation, according to classical nucleation theory. Of course, the size of particles also influences the freezing rate, and this causes a spread in freezing times for particles at the same temperature. The probability for freezing with respect to time can be expressed as:⁹

$$-\frac{d \ln P(t)}{dt} = J_V(T)V(r) + J_S(T)S(r) \quad (5.34)$$

where $P(t)$ is the probability that a droplet (at temperature, T and of radius, r) is still unfrozen at time t (i.e. $P(0) = 1$). $V(r)$ and $S(r)$ are the particle volume and surface area, respectively, and $J_V(T)$ and $J_S(T)$ are the volume and surface freezing rate constants, respectively.

The freezing times for particles are determined based on the change in the scattering image that occurs upon freezing. Figure 5.29 shows images of the elastically scattered light for a large particle

($r = 5042$ nm) and a small particle ($r = 924$ nm) immediately before and after freezing. The large particle was observed to freeze at 287.5 K. The scattering phase function for the liquid large particle (Figure 5.29(a)) has a regular striped pattern that is fairly constant with time. For the frozen particle (Figure 5.29(b)), the scattering pattern is much more irregular, and changes with time. In general, the integrated intensity of the scattered light is greater for the solid particle compared to the liquid particle. The plot in Figure 5.30(a) shows this increase in scattering intensity upon freezing for the large particle. It plots the integrated intensity for several phase function images with respect to time. At the time of freezing, there is an increase in the integrated scattering intensity (note that this particle was lost from the trap very soon after freezing, thus there are only a couple of points showing the increased scattering intensity for the frozen particle). These changes to the scattering pattern and scattering intensity were also observed in previous single particle freezing studies.^{197,230,241-245} The small particle in Figure 5.29 was observed to freeze at 286.9K. For smaller particles, the change in the scattering pattern is often less pronounced (Figure 5.29(c) (liquid) and Figure 5.29(d) (solid)). However, there is still an increase in the scattering intensity upon freezing. A plot of the integrated intensity of the scattering images for this smaller particle is shown in Figure 5.30(b).

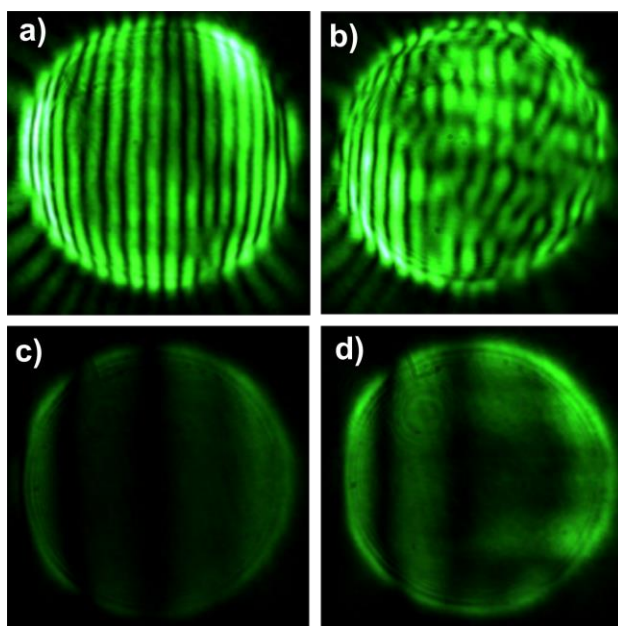


Figure 5.29: A large ($r = 5042$ nm) supercooled hexadecane particle at 287.5 K a) before and b) after freezing. A small ($r = 924$ nm) supercooled hexadecane particle at 286.9 K c) before and d) after freezing. Reprinted with permission from *Review of Scientific Instruments*, 2014, **85**, 095107. Copyright 2014, AIP Publishing LLC.

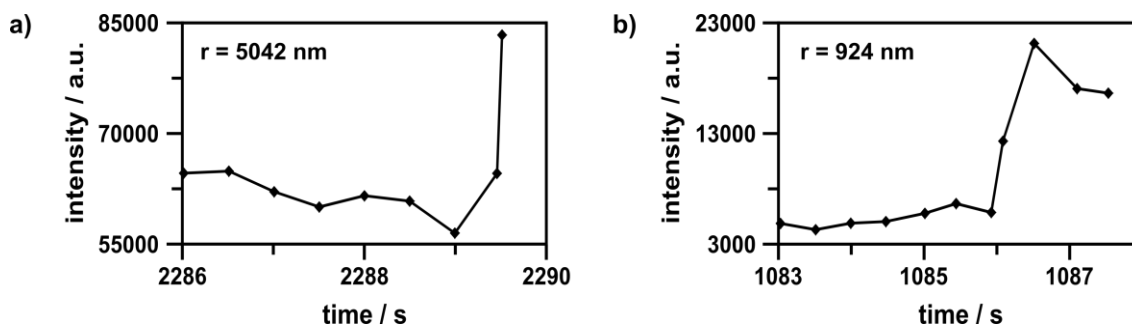


Figure 5.30: The integrated scattering intensity with respect to time for the particles in Figure 5.29. a) The scattering intensity for the large particle (panels (a) and (b) in Figure 5.29) and b) the scattering intensity for the small particle (panels (c) and (d) in Figure 5.29). Note, the large ($r = 5042$ nm) particle was lost from the trap shortly after freezing, thus there are not very many intensity points on the plot in panel (a) after the time of freezing.

Hexadecane particles often fall out of the trap immediately after freezing (as was the case for the large hexadecane particle in Figure 5.29(a) & (b)). While the crystal structure of particles cannot be directly observed in the current setup, previous studies of bulk hexadecane have shown that it has a triclinic crystal structure^{246,247} and a crystal habit resembling elongated and flat needles.²⁴⁸ Both the shape and RI of the hexadecane particles changes upon freezing. There is likely a difference in the balance of the forces exerted on the solid versus liquid particles due to these changes.²³⁴ As well, the crystalline particles appear to rotate within the trap, likely caused by a torque introduced by the radiation pressure from each of the counter-propagating beams.¹⁹⁸ We believe that these factors often lead to the particles being lost from the equilibrium trapping position.

Figure 5.31 shows an example of a hexadecane particle ($r = 3236$ nm) that falls out of the trap immediately after freezing (284.1 K). The sequential still frames were extracted from the video (the video was recorded at approximately 18 frames per second). The supercooled liquid particle was quite stable in the trap (e.g. frames 1-3). When the particle homogeneously freezes (frame 4), as denoted by the appearance of bright spots in the scattering image and a less regular scattering pattern, it becomes unstable (frame 5 & 6) and is quickly lost from the trap (frame 7 & 8). This behavior was typical for many of the particles upon freezing.

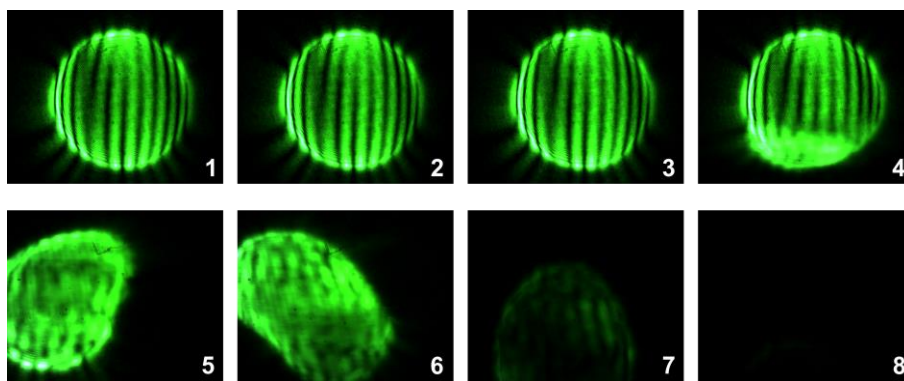


Figure 5.31: Individual frames (sequentially from frame 1-8) from a video of a stable supercooled hexadecane particle (frames 1-3) that homogeneously freezes (frame 4), becomes unstable (frames 5-6), and then falls from the trapping position in frame 7. The video was recorded at a rate of approximately 18 frames per second, and each frame was recorded 0.054 s apart.

While waiting to observe homogeneous freezing of hexadecane particles, in some cases we would observe heterogeneous freezing caused by a collision with another incoming hexadecane particle. Figure 5.32 illustrates this process for one such collisional freezing event. Frames 1-3 show a stably trapped hexadecane particle. In frame 3, a second particle (size not known) can be seen to approach the trapped particle, initiating freezing in frame 4. The frozen particle becomes unstable in is quickly lost from the trap in a similar manner to what was observed for the homogeneously frozen particle in Figure 5.31.

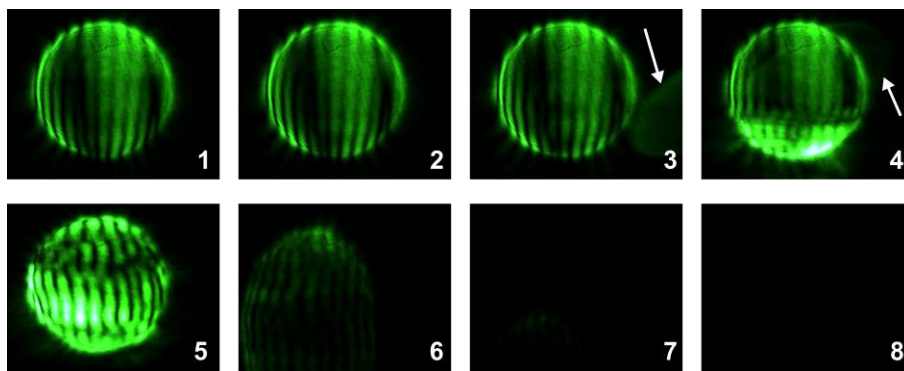


Figure 5.32: Individual frames (sequentially from frame 1-8) from a video of a stable supercooled hexadecane particle (frames 1-3) that freezes by contact (collision) with a second hexadecane particle. The arrows in frames 3 & 4 point toward the second particle. The frozen particle becomes unstable and is lost from the trapping position in frames 6-7. The video was recorded at a rate of approximately 19 frames per second, and each frame was recorded 0.052 s apart.

While many hexadecane particles were lost from the trap after freezing and subsequently becoming unstable, this was not the case for all particles. Solid particles that have remained fairly stably trapped have made it possible to perform freeze-melt cycles for several hexadecane particles. Particles are cycled between the solid and liquid phase by increasing or decreasing the temperature of the cell. Note that for all these experiments, the temperature setting on the refrigerated circulation unit was ramped higher or lower by changing the temperature setting to at temperature above or below, respectively, the melting point for hexadecane. The temperature of the trapping cell was not stabilized before a freezing or melting event, and thus an accurate temperature reading is not available at the time of freezing or melting for these particles. These experiments are not included in the plot in Figure 5.28 for this reason.

Five hexadecane particles were cycled in a solid-liquid-solid cycle. Figure 5.33 shows images for one such particle. The cycle was started for a trapped frozen particle. Increasing the temperature

in the cell above the melting point led to melting at $t = 518$ s after nebulization ($r = 3948$ nm immediately after melting). The temperature of the cell was then rapidly cooled below the hexadecane melting point and the particle was observed to freeze at $t = 1620$ s ($r = 3740$ nm immediately before freezing). Note that there is a change in particle size while the in the liquid state due to evaporation of the hexadecane.

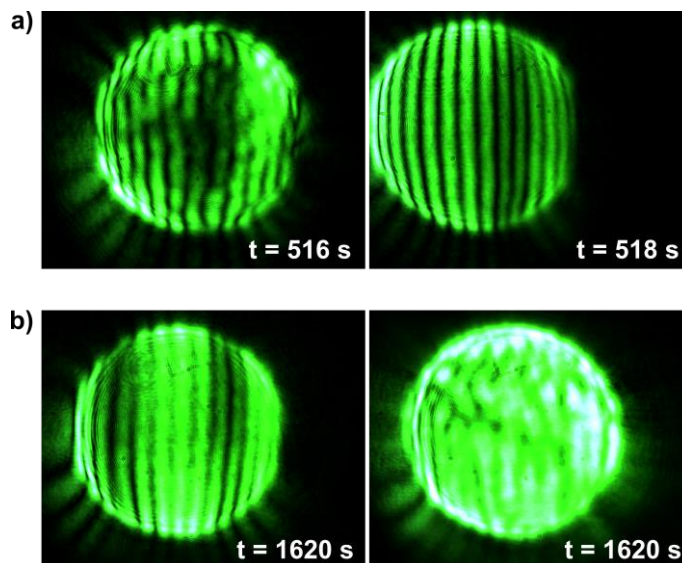


Figure 5.33: A cycled hexadecane particle. a) Melting of the frozen particle (note the particle moved off camera between these two frames) and b) subsequent freezing of the same particle (two adjacent frames from the video).

One additional cycling experiment was performed where a single hexadecane particle was alternately frozen 6 times and melted 5 times. This particle remained trapped for a total of 78 minutes. The plot in Figure 5.34 outlines the times for each of the freezing and melting events and indicates the size of the particle at each time. One of the video files that was being recorded during this experiment became corrupted and thus there is no size available for the particle when it froze at $t = 3658$ s. Future cycling studies with a more controlled temperature increase or decrease

(i.e. allowing for the cell temperature to stabilize) could prove to be very interesting, especially since the particle changes size due to evaporation during the cycle. Hexadecane evaporation will be discussed in more detail in Section 5.3.4.

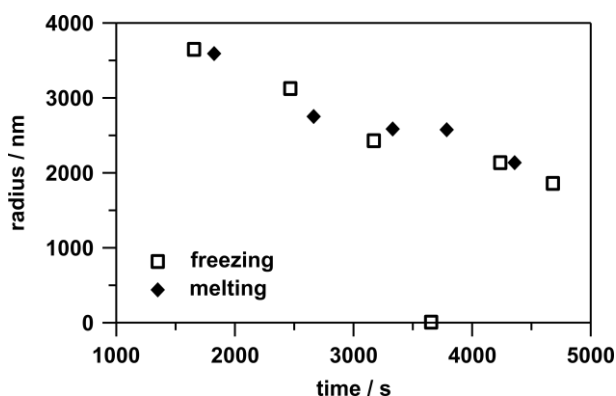


Figure 5.34: Plot of the freezing and melting times for one hexadecane particle that was cycled between the solid and liquid state. The plot indicates the particle size at the time of each phase change. Note, the particle could not be sized for the freezing event which occurred at $t = 3658$ s due to corruption of the video file that was recorded at that time.

5.3.3.2 Dodecane

Similar experiments were performed for dodecane as for hexadecane. The main difference is that experiments were performed at lower temperatures, as the melting point for bulk dodecane is 263.58 K.²¹⁷ Freezing of a small number of supercooled dodecane particles was observed for particles trapped at 258.1 ± 0.2 K (5.5 K supercooled) and further cooled as low as 252.5 ± 0.2 K (11.0 K supercooled). For the dodecane experiments, a dry N_2 flow was used at a rate of 0.25-8.0 mL/min. The N_2 flowed through copper tubing that was submerged in a chilled bath near 273 K. The 8.0 mL/min flow rate was required to remove the excess dodecane particles from the cell. In comparison to hexadecane, the excess dodecane particles were more difficult to remove

from the cell and required the higher N₂ flow rate. Once all the excess particles were removed from the cell, the flow was reduced as low as 0.25 mL/min. The RI value used for dodecane was 1.451 at 532 nm and 252.0 K and was obtained following the same method described for hexadecane (Section 5.3.3.1). Bulk dodecane has a similar crystal structure to bulk hexadecane (triclinic)²⁴⁹ and is also expected to have a corresponding similar crystal habit of flat, needle-like particles.²⁴⁸

Homogeneous freezing was observed for several dodecane particles ranging in size from $r = 1700$ nm to $r = 4700$ nm, each in less than 60 s. Fewer experiments were performed for dodecane compared to hexadecane; however, very similar trends were observed for both substances. Figure 5.35 shows images for a dodecane particle before and after freezing. As for hexadecane, the solid particles are characterized by an irregular scattering pattern. Figure 5.35 shows a plot of the intensity of the perpendicularly polarized scatter light with respect to time. The solid dodecane phase is also characterized by a sharp increase in this scattering intensity at the time of freezing.

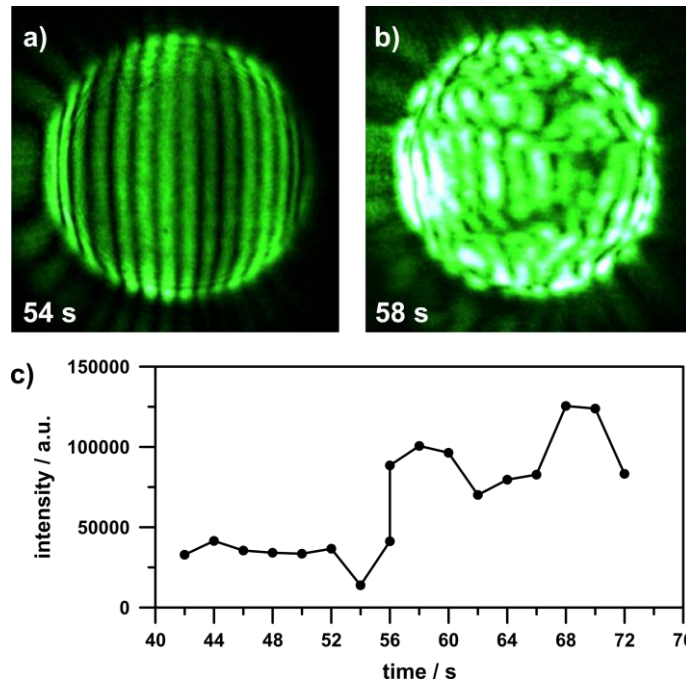


Figure 5.35: A dodecane particle ($r = 4180$ nm) before a) and after b) homogeneous freezing at 252.6 K. c) The integrated scattering intensity for this particle is plotted with respect to time. Reprinted with permission from *Review of Scientific Instruments*, 2014, **85**, 095107. Copyright 2014, AIP Publishing LLC.

Freeze-melt cycles have also been possible for dodecane particles. Figure 5.36 shows a plot of the freezing times for one particle that was cycled between the solid and liquid state. The size of the particle at each event is indicated. As seen for hexadecane, the dodecane particle was found to decrease in size due to evaporation during the time that it was trapped.

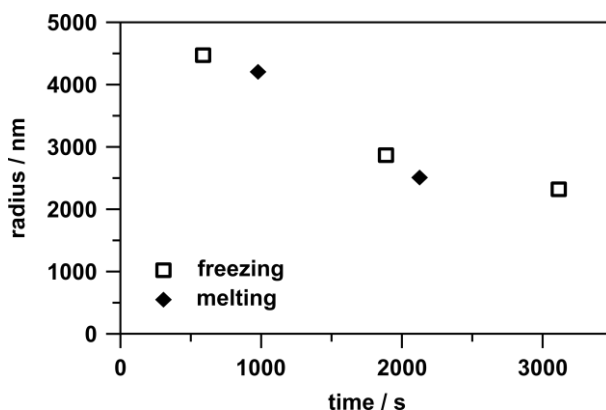


Figure 5.36: Plot of the freezing and melting times for one dodecane particle that was cycled between the solid and liquid state. The plot indicates the particle size at the time of each phase change.

5.3.3.3 Water

After performing freezing studies for hydrocarbon particles (hexadecane and dodecane), the temperature of the cell was lowered even further in order to observe the homogeneous freezing of single supercooled water particles. Water particles were trapped at 228.05 ± 0.03 K and the temperature was held constant for all experiments. At this temperature, water particles were supercooled by about 45.1 K. In order to minimize particle evaporation, we used a humidified flow (95% RH at 294.15 K) at a flow rate of 3.0-5.0 mL/min during the experiments. In this temperature range, the crystal structure for water is hexagonal and the crystal habit is expected to also be hexagonal.²⁵⁰ The RI for water was not available at the experimental conditions. As for hexadecane and dodecane, a value was estimated from available data in a similar manner as for hexadecane and dodecane. A fifth-order polynomial fit of the literature data at 632.8 nm and 589.3 nm was performed.²¹⁷ Assuming a Cauchy relationship (Equation (5.31)), a value of $n = 1.327$ was determined at 532 nm and 228.0 K for water.

There have been several previous studies of freezing for levitated supercooled water particles. Leisner and coworkers^{197,242-244} have studied homogeneous water nucleation in a cooled EDB for particles that were on the order of tens of microns in radius. They observed homogeneous freezing at temperatures ranging from approximately 236-238 K. Taji et al.¹⁹⁸ have also trapped single liquid and solid water particles in an optical trap. Homogeneous freezing was observed below 233 K for supercooled water droplets typically between $r = 10 \mu\text{m}$ and $r = 20 \mu\text{m}$ in size. In these experiments, particles were only trapped on the order of a few minutes.

In our current experiments, freezing was observed for particles ranging in size from $r = 456 \text{ nm}$ to $r = 1956 \text{ nm}$, with freezing times ranging from 282-976 s (at 228 K). Water has proven to be the most difficult substance to study thus far in the low temperature trap because of the extremely quick evaporation of particles before freezing is observed. However, we have been able to trap supercooled water particles for up to 16 minutes at 228 K. This temperature is in the region of the water phase diagram known as “no-man’s land”—below the homogeneous nucleation temperature ($\sim 235 \text{ K}$ for bulk water)²⁵¹ and above the crystallization temperature ($\sim 155 \text{ K}$).²⁵² This region is experimentally restricted due to the rapid crystallization of supercooled water. Our ability to trap submicron particles may open up this range for further experimental studies since the small particle size reduces the probability of nucleation (refer to Equation (5.34)).

5.3.4 Particle evaporation

The temperature-controlled CPBB setup also allows for the study of particle evaporation for particles at low temperatures. Rates of evaporation measured at a constant temperature can provide low vapour pressure data that can often be difficult to measure.²⁵³ It is also a way to determine vapour pressure data for metastable states, such as supercooled liquids. Here, the focus

is on evaporation experiments for supercooled hexadecane particles. The results presented in this section are the preliminary evaporation measurements in the low temperature trapping cell. It is important to note that the system has not yet been optimized for conducting these types of experiments. Determining optimum parameters for the evaporation studies for hexadecane particles is a point of ongoing work.

The hexadecane particles were observed to continuously decrease in size due to evaporation during their time in the trap (Section 5.3.3.1). The probability of homogeneous nucleation (Equation (5.34)) depends on the particle volume and surface area. A thorough study of single particle freezing kinetics thus requires understanding and control of particle evaporation. The plot in Figure 5.37 shows the decrease in size for five hexadecane particles with respect to time. Particles were sized from scattering images taken roughly every 5-10 minutes and particle sizes were determined as outlined in Section 2.3.3.2. Initial sizes for the particles in Figure 5.37 range from $r = 3000\text{-}5000$ nm. After approximately 30 minutes in the trap, particle radii typically decreased to about half the initial value. While a continuous decrease in particle size complicates the study of particle freezing kinetics, the fact that particles remain in the trap over such a large size change illustrates the range of particle sizes that can be studied in the current CPBB setup. However, the position of the particle within the trap often fluctuated with the changing size.

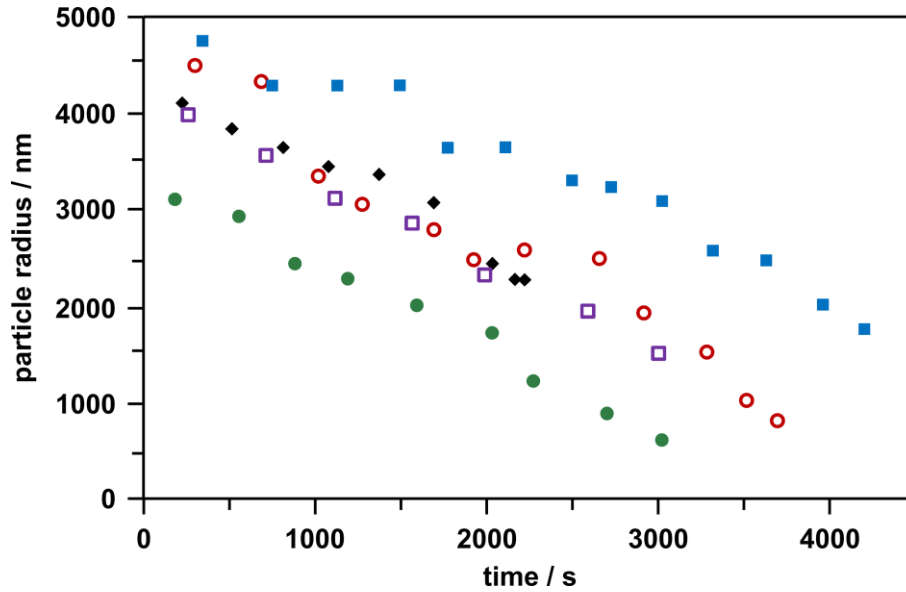


Figure 5.37: Sizes for five hexadecane particles plotted with respect to time. Particles were trapped at 287.5 K. Each particle is represented by a different shape/colour data point.

In the current hexadecane evaporation experiments, we work within the continuum regime.²⁵⁴ The single hexadecane particles are trapped in an environment at a constant temperature and at atmospheric pressure with a continuous N₂ flow. In the continuum regime, it can be assumed that the size of particles is much greater than the mean free path of the evaporating gas molecules and that the N₂ flow prevents accumulation of hexadecane vapour around the liquid particle. The rate of droplet evaporation can then be calculated from:²⁵⁴

$$\frac{dr^2}{dt} = -\frac{8D_v M p}{\rho R T} = -S_e(T) \quad (5.35)$$

where D_v is the vapour diffusion coefficient, M is the molecular weight of the vapour, p is the vapour pressure, ρ is the droplet density, R is the gas constant, and T is the absolute temperature. In this

regime, the evaporation is controlled by the rate of vapour diffusion. Integration of Equation (5.35) shows that the square of the droplet radius should be a linear function of time with slope $S_e(T)$:

$$r^2 = r_i^2 - S_e(T) \cdot t \quad (5.36)$$

where r_i is the initial particle radius.

Determination of the vapour pressure from the above equations is complicated by the fact that diffusion coefficients are often not known experimentally and must then be estimated, leading to large errors in the resulting values. Tang and Munkelwitz²⁵⁴ have suggested a method to avoid this problem by using known vapour pressure data determined at higher temperatures along with the known evaporation rates at the higher temperatures.

Figure 5.38 shows the same data from Figure 5.37 plotted as the squared radius as a function of time. The slope for each data set in Figure 5.38 should be equal since all hexadecane particles were studied at the same constant temperature (287.5 K). From a linear regression of each particle's sizing data, values for $S_e(T)$ were found to range from $3.34 \times 10^3 \text{ nm}^2/\text{s}$ to $5.80 \times 10^3 \text{ nm}^2/\text{s}$, with an average value of $4.84 \times 10^3 \text{ nm}^2/\text{s}$. This broad range for the value of $S_e(T)$ derives in part from the error associated with each sizing result ($r \pm 150 \text{ nm}$), which is more significant when the data is plotted as r^2 .

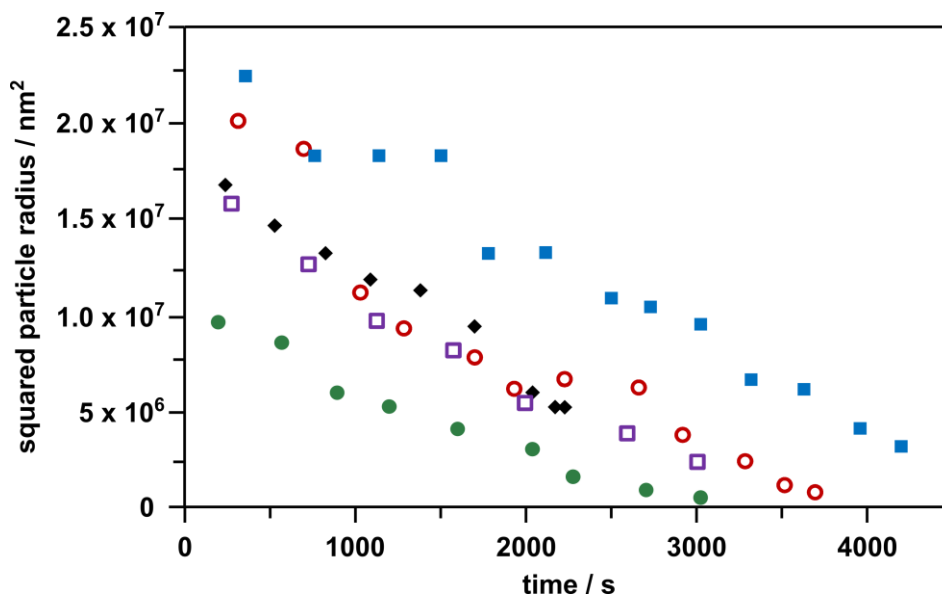


Figure 5.38: Data for hexadecane evaporation experiments plotted as squared particle radius as a function of time. The data points (colour and shape) correspond to those for the particles in Figure 5.37.

As mentioned earlier, these single particle evaporation experiments were not performed under optimized conditions. One parameter that needs to be optimized is the N₂ flow rate in order to remove the hexadecane vapour at an appropriate rate. If the N₂ flow rate is too low, there may be accumulation of hexadecane vapour around the particle. Other particle evaporation studies have used constant flow rates of approximately 30 mL/min²⁵³ and 100 mL/min.²⁵⁵ These flow rates are much higher than that used in the current hexadecane experiments (0.25-4.0 mL/min). We were not able to keep particles trapped with flow rates greater than approximately 10 mL/min.

Additionally, the current method for introducing particles in to the trap may be problematic for evaporation studies. The introduction of a large quantity of particles into the trapping cell likely results in a high concentration of hexadecane vapour within the cell. Davis and Ray²⁵⁶ have

previously noted the importance of introducing as few aerosols as possible for evaporation experiments to avoid saturation of the surrounding gas phase. Improvements to the method of particle introduction will be discussed in Section 5.4. Optimizing the methods for particle introduction could improve all types of trapping experiments discussed in this work, not just those dealing with particle evaporation.

These preliminary experiments show that there is promise to study particle evaporation at low temperatures in the current setup. With the CPBB optical trap, it is possible to study evaporation rates for single particles where the particle radius decreases into the submicron range.

5.3.5 Conclusions for low temperature trapping experiments

This section has demonstrated preliminary experiments in a temperature-controlled CPBB optical trap. These experiments represent the first reported observations of the freezing process for single levitated submicron particles in air using an optical trapping technique. Freezing (homogeneous and heterogeneous) and evaporation studies at a constant temperature can be performed in the current setup for single particles ranging in size from $r = 450\text{-}5500$ nm. The limitations for sizing particles below approximately $r = 400$ nm are discussed in Section 2.3.3.3. Trapping of particles larger than $r = 5500$ nm could be accomplished by changing the Bessel beam core size (refer to Section 5.1.3). Note that it is possible to size particles greater than $r = 5500$ nm with the current sizing methods. The current system can be used for measurements at temperatures as low as 223 K.

Improvements to the current setup are required for an in-depth study of particle freezing kinetics. The current cell design measures the temperature on the surface of the cell (refer to Section 2.3.2.1) and assumes this to be the temperature within the trapping region. Future experiments will make

use of a thermocouple within the cell to gain a more accurate temperature value which is required since nucleation times are highly dependent on temperature.

5.4 Summary of single particle measurements

This chapter has demonstrated the variety of experiments that can be performed at both room temperature and low temperatures for single aerosol particles. The use of the CPBB optical trap allows for trapping of particles into the submicron regime and opens up the possibility to further study size dependent effects for aerosol phase transitions, such as glassy aerosol formation and freezing.

One of the limiting factors in the study of single aerosols (especially for the long room temperature experiments presented in Section 5.2) is the residence time in the trap. This is in part based on the quality of the trap alignment. Small misalignments (and drift of the alignment with time) can severely limit trapping in the CPBB optical trap. One method that has been suggested to improve particle stability for long term experiments is the use of the quadruple Bessel beam (QBB) optical trap.¹⁹⁰ The QBB trap consists of two perpendicularly arranged CPBB optical traps.

Calculations of trap stability have shown that the QBB trap can offer solutions to the problems encountered with the CPBB trap.¹⁹⁰ It was found that trap alignment is much less critical for the QBB trap and that particle stability may be greatly enhanced, which would prove useful for studies requiring extended time in the trap. Additionally, particles could be confined to less than 100 nm in all dimensions. This feature could be very advantageous for evaporation studies where particles were seen to move to different positions within the trap as their size decreased. As well, the improved particle stability could facilitate the use of higher flow rates (> 10 mL/min) in the single

particle evaporation experiments. The greater stability of the QBB trap may also limit the number of particles that are lost from the trap immediately after freezing, thus facilitating cycling experiments between the solid and liquid state.

The method used to generate aerosols in the current work was to use a medical nebulizer which produces an abundance of particles over a fairly large size range (nanometers to several microns). This method leads to a few experimental problems. The lack of control of the particle size that is generated means there is no control over the size of particles that become trapped (within the size range that can be trapped in the CPBB trap with a given Bessel beam core size). As well, there is an extreme abundance of particles that enter into the cell. With time, the windows of the cell become dirty and this can limit both the trapping ability and the ability to size particles. Eventually, the vacuum chamber and cell must be disassembled for cleaning, which introduces the possibility of losing a good alignment. As well, a large number of particles within the cell tends to lead to agglomeration of particles, limiting the chances for trapping a submicron-sized particle.

Improvements to particle injection methods include the use of a valve to control the introduction of particles and reducing the flow rate of aerosols into the cell.

The current method of sizing particles based on the elastically scattered light from the laser (532 nm) is only useful for particles larger than approximately $r = 400$ nm. The implementation of a white light scattering system would provide more accurate sizing results²⁵³ and allow for sizing of particles below $r = 400$ nm (ongoing research within the Signorell group). This would be especially useful for freezing kinetic experiments due to the relationship of the freezing probability on the particle volume and surface area and for evaporation measurements to reduce the error in the calculated value of $S_e(T)$.

The combination of these improvements to the experimental setup and analysis methods will further allow for the study of single submicron particles and lead to a better understanding of aerosol processes, including glassy aerosols formation, freezing and melting, and particle evaporation.

Chapter 6: Conclusions

6.1 Summary

This thesis presents low temperature studies of ensembles of aerosol particles formed in a bath gas cooling cell and of single aerosol particles suspended in a counter-propagating Bessel beam (CPBB) optical trap. The use of both ensemble and single particle measurements can provide complementary information for characterizing aerosol particles, as discussed in Chapter 1. While it is not currently possible to examine single particles in the low temperature trapping cell at temperatures as low as those used for ensemble studies (78 K), this area is a point of further interest. Future experiments to this regard are outlined below (Section 6.2).

Chapter 3 and Chapter 4 both address infrared (IR) measurements of ensembles of aerosol particles formed in the bath gas cooling cell. The $\text{CO}_2\text{-H}_2\text{O}$, $\text{NH}_3\text{-H}_2\text{O}$, and $\text{C}_2\text{H}_2\text{-H}_2\text{O}$ aerosol ensembles are relevant to the atmospheres of various planets and moons throughout our solar system. In each of these chapters, the particle properties (and their temporal evolution) were inferred from IR spectra and supported by comparison to calculated spectra for various particle structures and architectures using the vibrational exciton model. The ensemble measurements are useful to help predict the types of particle structures and architectures (e.g. molecularly mixed, core-shell) that may be present in a variety of different atmospheres.

These ensemble measurements also show the variety of different particle structures and architectures that may exist for different systems. For example, while all experiments were performed under similar conditions, there were dramatic differences in the results for CO₂-H₂O aerosol particles compared to those for NH₃-H₂O and C₂H₂-H₂O aerosol particles. The properties of these aerosols also differ from other mixed aerosol particles that have been previously studied in our group under similar conditions (e.g. CO₂-C₂H₂ and NH₃-C₂H₂).³²⁻³⁴ These results illustrate that whether particles are molecularly mixed, form a core-shell structure, or form a co-crystalline structure, for example, is highly dependent on the molecules involved and how they interact with each other. It is not obvious that any general trends exist. The present investigations rather hint that each mixture needs to be examined separately.

Chapter 5 summarizes the single particle experiments performed at low temperatures (228-260 K) in a new CPBB optical trap for particles in the micron and submicron size range. The low temperature experiments examined homogeneous freezing times for supercooled single aerosol particles (hexadecane, dodecane, and water) and show preliminary studies of single particle evaporation rates (hexadecane). These experiments represent the first low temperature studies of single optically trapped particles in the submicron size range. The study of submicron sized aerosol particles at lower temperatures is highly relevant for a better understanding of atmospheric processes, where submicron sized particles are expected to play an important role.⁹⁵

This work shows how ensemble and single particle aerosol experiments can provide complementary information about aerosol particles. Ensemble studies are a suitable way to model atmospheric conditions as well as to study averaged properties of particle ensembles (e.g. clouds). However, in order to gain a complete understanding of the properties and behaviour of aerosol

particles, single particle measurements are required to probe properties that may not be easily accessed when features are averaged (e.g. size dependent effects).

6.2 Outlook

The low temperature CPBB optical trap can currently be used for experiments at temperatures as low as approximately 223-228 K. Chapter 5 outlines the first single particle experiments at low temperatures performed using this new experimental setup. Ultimately, the goal is to perform single particle measurements that would complement the ensemble aerosol particle studies outlined in Chapter 3 for CO₂-H₂O particles and in Chapter 4 for NH₃-H₂O and C₂H₂-H₂O particles.

In order to perform single particle measurements to complement the ensemble measurements, the system would need to be cooled to much lower temperatures (i.e. down to 78 K). The lowest temperature that can be realized with the current experimental setup is limited by the O-rings that are used to seal the vacuum chamber (at temperatures below 223-228 K, the vacuum is no longer maintained within the chamber using O-rings). To reach temperatures down to 78 K, we would need to use indium sealings and a cold finger cryocooler. The single particle measurements presented here were all performed at atmospheric pressure. For some studies, the pressure in the single particle trap would need to be decreased in order to match the conditions in planetary atmospheres (e.g. conditions in the Martian atmosphere). Trapping aerosol particles at lower pressures is a challenge but could be achieved with active feedback to stabilize the particles.²⁵⁷

Single particle measurements could be useful to extract additional information about particle properties that are averaged in the ensemble measurements (presented in Chapter 3 and Chapter 4). There is currently a limited understanding of the formation of CO₂ clouds on Mars,

where nucleation of CO₂ is suggested to occur onto water particles, dust particles, or water-coated dust particles (refer to Chapter 3). Single particle experiments at low temperatures would allow us to better characterize heterogeneous nucleation of CO₂ onto each of these possible substrates and help to elucidate which is the most plausible particle structure in the Martian atmosphere. Single particle measurements of CO₂ nucleation onto water particles could also help to confirm the particle structure determined from ensemble measurements (that of CO₂ patches on a water particle). Additionally, single particle measurements could be useful to qualify the kinetics for mixing/demixing. The kinetics of mixing in NH₃-H₂O and C₂H₂-H₂O particles in Chapter 4 was not further analyzed since there may be contributions from several mixing mechanisms (i.e. it is possible that mixing does not only occur via solid state diffusion of core-shell particles) and because we could not accurately quantify the properties of particles in the ensemble (e.g. interface area for core-shell particles). For single particles, it is possible to determine particle size and composition, which would allow for a detailed study of the kinetics of the mixing process. Such single particle measurements would increase the understanding of aerosol particles present in the atmospheres of planets and moons throughout our solar system.

References

1. J. H. Seinfeld and S. N. Pandis, *Atmospheric Chemistry and Physics - From Air Pollution to Climate Change*, John Wiley & Sons, Inc., Hoboken, New Jersey, 2nd edn., 2006.
2. C. F. Bohren and D. R. Huffman, *Absorption and scattering of light by small particles*, John Wiley & Sons, New York, 1983.
3. Ó. F. Sigurbjörnsson, G. Firanescu, and R. Signorell, *Annu. Rev. Phys. Chem.*, 2009, **60**, 127–146.
4. G. Myhre, D. Shindell, F.-M. Bréon, W. Collins, J. Fuglestad, J. Huang, D. Koch, J.-F. Lamarque, D. Lee, B. Mendoza, T. Nakajima, A. Robock, G. Stephens, T. Takemura, and H. Zhang, in *Climate Change 2013: The Physical Science Basis. Contribution of Working Group I to the Fifth Assessment Report of the Intergovernmental Panel on Climate Change*, eds. T. F. Stocker, D. Qin, G.-K. Plattner, M. Tignor, S. K. Allen, J. Boschung, A. Nauels, Y. Xia, V. Bex, and P. M. Midgley, Cambridge University Press, Cambridge, United Kingdom and New York, USA, 2013, pp. 659–740.
5. T. R. Karl and K. E. Trenberth, *Science*, 2003, **302**, 1719–1723.
6. N.-O. A. Kwamena and J. P. Reid, in *Colloid Science: Principles, Methods, and Applications*, ed. T. Cosgrove, Wiley-Blackwell, West Sussex, UK, 2nd edn., 2010, pp. 219–243.
7. S. Sastry, *Nature*, 2005, **438**, 746–747.
8. E. K. Lang, K. J. Knox, C. C. Wang, and R. Signorell, *Planet. Space Sci.*, 2011, **59**, 722–732.
9. Ó. F. Sigurbjörnsson and R. Signorell, *Phys. Rev. E*, 2008, **77**, 051601.
10. G. Firanescu, D. Hermsdorf, R. Ueberschaer, and R. Signorell, *Phys. Chem. Chem. Phys.*, 2006, **8**, 4149–4165.
11. G. Firanescu, T. C. Preston, C. C. Wang, and R. Signorell, in *Fundamentals and Applications in Aerosol Spectroscopy*, eds. R. Signorell and J. P. Reid, CRC Press, Boca Raton, 2011, pp. 25–47.
12. R. Signorell and M. K. Kunzmann, *Chem. Phys. Lett.*, 2003, **371**, 260–266.
13. A. Bonnamy, M. Jetzki, and R. Signorell, *Chem. Phys. Lett.*, 2003, **382**, 547–552.

14. R. Signorell, *Mol. Phys.*, 2003, **101**, 3385–3399.
15. M. Jetzki, A. Bonnamy, and R. Signorell, *J. Chem. Phys.*, 2004, **120**, 11775–11784.
16. R. Signorell, M. Jetzki, M. Kunzmann, and R. Ueberschaer, *J. Phys. Chem. A*, 2006, **110**, 2890–2897.
17. G. Firanescu, D. Luckhaus, and R. Signorell, *J. Chem. Phys.*, 2006, **125**, 144501.
18. R. Signorell and M. Jetzki, *Faraday Discuss.*, 2008, **137**, 51–64.
19. G. Firanescu, D. Luckhaus, and R. Signorell, *J. Chem. Phys.*, 2008, **128**, 184301.
20. Ó. F. Sigurbjörnsson, G. Firanescu, and R. Signorell, *Phys. Chem. Chem. Phys.*, 2009, **11**, 187–194.
21. T. C. Preston, G. Firanescu, and R. Signorell, *Phys. Chem. Chem. Phys.*, 2010, **12**, 7924–7933.
22. M. K. Kunzmann, R. Signorell, M. Taraschewski, and S. Bauerecker, *Phys. Chem. Chem. Phys.*, 2001, **3**, 3742–3749.
23. M. K. Kunzmann, S. Bauerecker, M. A. Suhm, and R. Signorell, *Spectrochim. Acta Part A*, 2003, **59**, 2855–2865.
24. A. Bonnamy, R. Georges, E. Hugo, and R. Signorell, *Phys. Chem. Chem. Phys.*, 2005, **7**, 963–969.
25. R. Signorell and M. Jetzki, *Phys. Rev. Lett.*, 2007, **98**, 013401.
26. M. Gadermann, D. Vollmar, and R. Signorell, *Phys. Chem. Chem. Phys.*, 2007, **9**, 4535–4544.
27. Ó. F. Sigurbjörnsson and R. Signorell, *Phys. Chem. Chem. Phys.*, 2008, **10**, 6211–6214.
28. C. C. Wang, P. Zielke, Ó. F. Sigurbjörnsson, C. R. Viteri, and R. Signorell, *J. Phys. Chem. A*, 2009, **113**, 11129–11137.
29. C. C. Wang, S. K. Atreya, and R. Signorell, *Icarus*, 2010, **206**, 787–790.
30. C. C. Wang, E. K. Lang, and R. Signorell, *Astrophys. J. Lett.*, 2010, **712**, L40–L43.
31. K. J. Knox, E. K. Lang, and R. Signorell, *J. Astronomical Data*, 2012, **18**, 3.

32. T. C. Preston, C. C. Wang, and R. Signorell, *J. Chem. Phys.*, 2012, **136**, 094509.
33. T. C. Preston and R. Signorell, *J. Chem. Phys.*, 2012, **136**, 094510.
34. T. C. Preston and R. Signorell, *Mol. Phys.*, 2012, **110**, 2807–2815.
35. E. K. Lang, K. J. Knox, and R. Signorell, *Planet. Space Sci.*, 2013, **75**, 56–68.
36. D. Luckhaus, G. Firanescu, E. K. Lang, G. N. Patey, and R. Signorell, *Mol. Phys.*, 2013, **111**, 2233–2242.
37. E. K. Lang, K. J. Knox, T. Momose, and R. Signorell, *J. Phys. Chem. A*, 2013, **117**, 11745–11759.
38. T. Dunder and R. E. Miller, *J. Chem. Phys.*, 1990, **93**, 3693–3703.
39. T. Dunder, M. L. Clapp, and R. E. Miller, *J. Geophys. Res.*, 1993, **98**, 1213–1221.
40. M. L. Clapp and R. E. Miller, *Icarus*, 1993, **105**, 529–536.
41. M. L. Clapp, R. E. Miller, and D. R. Worsnop, *J. Phys. Chem.*, 1995, **99**, 6317–6326.
42. L. J. Richwine, M. L. Clapp, R. E. Miller, and D. R. Worsnop, *Geophys. Res. Lett.*, 1995, **22**, 2625–2628.
43. M. L. Clapp and R. E. Miller, *Icarus*, 1996, **123**, 396–403.
44. M. L. Clapp, R. F. Niedziela, L. J. Richwine, T. Dransfield, R. E. Miller, and D. R. Worsnop, *J. Geophys. Res.*, 1997, **102**, 8899–8907.
45. R. F. Niedziela, M. L. Norman, C. L. DeForest, R. E. Miller, and D. R. Worsnop, *J. Phys. Chem. A*, 1999, **103**, 8030–8040.
46. M. L. Norman, J. Qian, R. E. Miller, and D. R. Worsnop, *J. Geophys. Res.*, 1999, **104**, 30571–30584.
47. M. L. Norman, R. E. Miller, and D. R. Worsnop, *J. Phys. Chem. A*, 2002, **106**, 6075–6083.
48. J. A. Barnes, T. E. Gough, and M. Stoer, *J. Chem. Phys.*, 1991, **95**, 4840–4844.
49. J. A. Barnes, T. E. Gough, and M. Stoer, *J. Phys. Chem.*, 1993, **97**, 5495–5498.
50. T. E. Gough and T.-Y. Wang, *Chem. Phys. Lett.*, 1993, **207**, 517–520.

51. T. E. Gough and T. Wang, *J. Chem. Phys.*, 1996, **105**, 4899–4904.
52. T. E. Gough and T. Wang, *J. Chem. Phys.*, 1995, **102**, 3932–3937.
53. G. E. Ewing and D. T. Sheng, *J. Phys. Chem.*, 1988, **92**, 4063–4066.
54. R. Disselkamp and G. E. Ewing, *J. Chem. Phys.*, 1993, **99**, 2439–2448.
55. F. Fleyfel and J. P. Devlin, *J. Phys. Chem.*, 1989, **93**, 7292–7294.
56. B. Rowland and J. P. Devlin, *J. Chem. Phys.*, 1991, **94**, 812–813.
57. N. Barton, B. Rowland, and J. P. Devlin, *J. Phys. Chem.*, 1993, **97**, 5848–5851.
58. V. Buch, L. Delzeit, C. Blackledge, and J. P. Devlin, *J. Phys. Chem.*, 1996, **100**, 3732–3744.
59. J. P. Devlin and V. Buch, *Mikrochim. Acta Suppl.*, 1997, **14**, 57–66.
60. J. P. Devlin, C. Joyce, and V. Buch, *J. Phys. Chem. A*, 2000, **104**, 1974–1977.
61. N. Uras and J. P. Devlin, *J. Phys. Chem. A*, 2000, **104**, 5770–5777.
62. N. Uras, V. Buch, and J. P. Devlin, *J. Phys. Chem. B*, 2000, **104**, 9203–9209.
63. J. P. Devlin, J. Sadlej, and V. Buch, *J. Phys. Chem. A*, 2001, **105**, 974–983.
64. N. Uras-Aytemiz, C. Joyce, and J. P. Devlin, *J. Phys. Chem. A*, 2001, **105**, 10497–10500.
65. J. P. Devlin, D. B. Gulluru, and V. Buch, *J. Phys. Chem. B*, 2005, **109**, 3392–3401.
66. J. P. Devlin, C. A. Yinnon, and V. Buch, *Phys. Chem. Chem. Phys.*, 2009, **11**, 7819–7825.
67. J. P. Devlin, in *Fundamentals and Applications in Aerosol Spectroscopy*, eds. R. Signorell and J. P. Reid, CRC Press, Boca Raton, 2011, pp. 49–78.
68. L. Delzeit, K. Powell, N. Uras, and J. P. Devlin, *J. Phys. Chem. B*, 1997, **101**, 2327–2332.
69. V. Buch, S. Bauerecker, J. P. Devlin, U. Buck, and J. K. Kazimirski, *Int. Rev. Phys. Chem.*, 2004, **23**, 375–433.
70. M. Taraschewski, H. K. Cammenga, R. Tuckermann, and S. Bauerecker, *J. Phys. Chem. A*, 2005, **109**, 3337–3343.

71. S. Bauerecker, *Phys. Rev. Lett.*, 2005, **94**, 033404.
72. E. Dartois and S. Bauerecker, *J. Chem. Phys.*, 2008, **128**, 154715.
73. S. Bauerecker and E. Dartois, *Icarus*, 2009, **199**, 564–567.
74. C. Medcraft, E. G. Robertson, C. D. Thompson, S. Bauerecker, and D. McNaughton, *Phys. Chem. Chem. Phys.*, 2009, **11**, 7848–7852.
75. E. G. Robertson, C. Medcraft, L. Puskar, R. Tuckermann, C. D. Thompson, S. Bauerecker, and D. McNaughton, *Phys. Chem. Chem. Phys.*, 2009, **11**, 7853–7860.
76. W. Hujo, M. Gaus, M. Schultze, T. Kubař, J. Grunenberg, M. Elstner, and S. Bauerecker, *J. Phys. Chem. A*, 2011, **115**, 6218–6225.
77. C. Medcraft, D. McNaughton, C. D. Thompson, D. R. T. Appadoo, S. Bauerecker, and E. G. Robertson, *Phys. Chem. Chem. Phys.*, 2013, **15**, 3630–3639.
78. R. Signorell, *J. Chem. Phys.*, 2003, **118**, 2707–2715.
79. G. Firanesu and R. Signorell, *J. Phys. Chem. B*, 2009, **113**, 6366–6377.
80. D. L. Glandorf, A. Colaprete, M. A. Tolbert, and O. B. Toon, *Icarus*, 2002, **160**, 66–72.
81. A. Colaprete and O. B. Toon, *J. Geophys. Res.*, 2003, **108**, 5025.
82. S. E. Wood, *Ph.D. Thesis, Univ. California, Los Angeles*, 1999.
83. D. L. Glandorf, D. B. Curtis, T. Colaprete, O. B. Toon, and M. A. Tolbert, in *AIP Conference Proceedings - Nucleation and Atmospheric Aerosols 2000: 15th International Conference*, eds. B. N. Hale and M. Kulmala, 2000, pp. 661–664.
84. A. Määttänen, H. Vehkamäki, A. Lauri, S. Merikallio, J. Kauhanen, H. Savijärvi, and M. Kulmala, *J. Geophys. Res.*, 2005, **110**, E02002.
85. A. Määttänen, H. Vehkamäki, A. Lauri, I. Napari, and M. Kulmala, *J. Chem. Phys.*, 2007, **127**, 134710.
86. L. A. Sromovsky, K. H. Baines, and P. M. Fry, *Icarus*, 2013, **226**, 402–418.
87. S. K. Atreya and A.-S. Wong, *Space Sci. Rev.*, 2005, **116**, 121–136.
88. A. Sánchez-Lavega, S. Pérez-Hoyos, and R. Hueso, *Am. J. Phys.*, 2004, **72**, 767–774.

89. J. H. Waite Jr., M. R. Combi, W.-H. Ip, T. E. Cravens, R. L. McNutt Jr., W. Kasprzak, R. Yelle, J. Luhmann, H. Niemann, D. Gell, B. Magee, G. Fletcher, J. Lunine, and W.-L. Tseng, *Science*, 2006, **311**, 1419–1422.
90. J. H. Waite Jr., W. S. Lewis, B. A. Magee, J. I. Lunine, W. B. McKinnon, C. R. Glein, O. Mousis, D. T. Young, T. Brockwell, J. Westlake, M.-J. Nguyen, B. D. Teolis, H. B. Niemann, R. L. McNutt Jr., M. Perry, and W.-H. Ip, *Nature*, 2009, **460**, 487–490.
91. K. Shin, R. Kumar, K. A. Udachin, S. Alavi, and J. A. Ripmeester, *Proc. Natl. Acad. Sci.*, 2012, **109**, 14785–14790.
92. H. Meresman, J. B. Wills, M. Summers, D. McGloin, and J. P. Reid, *Phys. Chem. Chem. Phys.*, 2009, **11**, 11333–11339.
93. A. E. Carruthers, A. J. Orr-Ewing, and J. P. Reid, *Proc. SPIE*, 2010, **7762**, 77620V.
94. A. E. Carruthers, J. S. Walker, A. Casey, A. J. Orr-Ewing, and J. P. Reid, *Phys. Chem. Chem. Phys.*, 2012, **14**, 6741–6748.
95. M. I. Cotterell, B. J. Mason, A. E. Carruthers, J. S. Walker, A. J. Orr-Ewing, and J. P. Reid, *Phys. Chem. Chem. Phys.*, 2014, **16**, 2118–2128.
96. J. W. Lu, A. M. J. Rickards, J. S. Walker, K. J. Knox, R. E. H. Miles, J. P. Reid, and R. Signorell, *Phys. Chem. Chem. Phys.*, 2014, **16**, 9819–9830.
97. R. Jaenicke, *Ann. N. Y. Acad. Sci.*, 1980, **338**, 317–329.
98. J. U. White, *J. Opt. Soc. Am.*, 1942, **32**, 285–288.
99. E. M. Purcell and C. R. Pennypacker, *Astrophys. J.*, 1973, **186**, 705–714.
100. J. J. Goodman, B. T. Draine, and P. J. Flatau, *Opt. Lett.*, 1991, **16**, 1198–1200.
101. B. T. Draine and P. J. Flatau, *User Guide for the Discrete Dipole Approximation Code DDSCAT 6.1*, 2004.
102. B. T. Draine, *Astrophys. J.*, 1988, **333**, 848–872.
103. B. T. Draine and J. Goodman, *Astrophys. J.*, 1993, **405**, 685–697.
104. B. T. Draine and P. J. Flatau, *J. Opt. Soc. Am. A*, 1994, **11**, 1491–1499.
105. M. J. Collinge and B. T. Draine, *J. Opt. Soc. Am. A*, 2004, **21**, 2023–2028.

106. B. T. Draine and P. J. Flatau, *J. Opt. Soc. Am. A*, 2008, **25**, 2693–2703.
107. P. Laven, *MiePlot (version 4.3)*, 2014.
108. R. C. Millard and G. Seaver, *Deep. Res.*, 1990, **37**, 1909–1926.
109. T. Owen, K. Biemann, D. R. Rushneck, J. E. Biller, D. W. Howarth, and A. L. Lafleur, *J. Geophys. Res.*, 1977, **82**, 4635–4639.
110. F. Montmessin, B. Gondet, J.-P. Bibring, Y. Langevin, P. Drossart, F. Forget, and T. Fouchet, *J. Geophys. Res.*, 2007, **112**, E11S90.
111. F. Scholten, H. Hoffmann, A. Määttänen, F. Montmessin, B. Gondet, and E. Hauber, *Planet. Space Sci.*, 2010, **58**, 1207–1214.
112. F. González-Galindo, A. Määttänen, F. Forget, and A. Spiga, *Icarus*, 2011, **216**, 10–22.
113. F. Forget and R. T. Pierrehumbert, *Science.*, 1997, **278**, 1273–1276.
114. M. A. Mischna, J. F. Kasting, A. Pavlov, and R. Freedman, *Icarus*, 2000, **145**, 546–554.
115. M. Vincendon, C. Pilorget, B. Gondet, S. Murchie, and J.-P. Bibring, *J. Geophys. Res.*, 2011, **116**, E00J02.
116. F. Montmessin, J.-L. Bertaux, E. Quémerais, O. Korablev, P. Rannou, F. Forget, S. Perrier, D. Fussen, S. Lebonnois, A. Rébérac, and E. Dismarellis, *Icarus*, 2006, **183**, 403–410.
117. R. T. Clancy and B. J. Sandor, *Geophys. Res. Lett.*, 1998, **25**, 489–492.
118. A. Määttänen, F. Montmessin, B. Gondet, F. Scholten, H. Hoffmann, F. González-Galindo, A. Spiga, F. Forget, E. Hauber, G. Neukum, J.-P. Bibring, and J.-L. Bertaux, *Icarus*, 2010, **209**, 452–469.
119. T. H. McConnochie, J. F. Bell III, D. Savransky, M. J. Wolff, A. D. Toigo, H. Wang, M. I. Richardson, and P. R. Christensen, *Icarus*, 2010, **210**, 545–565.
120. A. Colaprete, R. M. Haberle, and O. B. Toon, *J. Geophys. Res.*, 2003, **108**, 5081.
121. J. L. Foster, A. T. C. Chang, D. K. Hall, W. P. Wergin, E. F. Erbe, and J. Barton, *J. Geophys. Res.*, 1998, **103**, 25839–25850.

122. E. F. Erbe, A. Rango, J. Foster, E. G. Josberger, C. Pooley, and W. P. Wergin, *Microsc. Res. Tech.*, 2003, **62**, 19–32.
123. T. C. Preston and R. Signorell, *Proc. Natl. Acad. Sci. U. S. A.*, 2011, **108**, 5532–5536.
124. J. B. Pollack, D. Colburn, R. Kahn, J. Hunter, W. Van Camp, C. E. Carlston, and M. R. Wolf, *J. Geophys. Res.*, 1977, **82**, 4479–4496.
125. J. L. Gooding, *Icarus*, 1986, **66**, 56–74.
126. D. P. Cruikshank, A. W. Meyer, R. H. Brown, R. N. Clark, R. Jaumann, K. Stephan, C. A. Hibbitts, S. A. Sandford, R. M. E. Mastrapa, G. Filacchione, C. M. Dalle Ore, P. D. Nicholson, B. J. Buratti, T. B. McCord, R. M. Nelson, J. B. Dalton, K. H. Baines, and D. L. Matson, *Icarus*, 2010, **206**, 561–572.
127. A. Bar-Nun, G. Herman, D. Laufer, and M. L. Rappaport, *Icarus*, 1985, **63**, 317–332.
128. P. A. Gerakines, W. A. Schutte, J. M. Greenberg, and E. F. van Dishoeck, *Astron. Astrophys.*, 1995, **296**, 810–818.
129. P. U. Andersson, M. B. Någård, G. Witt, and J. B. C. Pettersson, *J. Phys. Chem. A.*, 2004, **108**, 4627–4631.
130. M. P. Collings, M. A. Anderson, R. Chen, J. W. Dever, S. Viti, D. A. Williams, and M. R. S. McCoustra, *Mon. Not. R. Astron. Soc.*, 2004, **354**, 1133–1140.
131. M. P. Bernstein, D. P. Cruikshank, and S. A. Sandford, *Icarus*, 2005, **179**, 527–534.
132. G. Kumi, S. Malyk, S. Hawkins, H. Reisler, and C. Wittig, *J. Phys. Chem. A.*, 2006, **110**, 2097–2105.
133. K. I. Öberg, H. J. Fraser, A. C. A. Boogert, S. E. Bisschop, G. W. Fuchs, E. F. van Dishoeck, and H. Linnartz, *Astron. Astrophys.*, 2007, **462**, 1187–1198.
134. O. Gálvez, I. K. Ortega, B. Maté, M. A. Moreno, B. Martín-Llorente, V. J. Herrero, R. Escribano, and P. J. Gutiérrez, *Astron. Astrophys.*, 2007, **472**, 691–698.
135. Ó. Gálvez, B. Maté, V. J. Herrero, and R. Escribano, *Icarus*, 2008, **197**, 599–605.
136. R. Hodyss, P. V. Johnson, G. E. Orzechowska, J. D. Goguen, and I. Kanik, *Icarus*, 2008, **194**, 836–842.

137. B. Maté, O. Gálvez, B. Martín-Llorente, M. A. Moreno, V. J. Herrero, R. Escribano, and E. Artacho, *J. Phys. Chem. A.*, 2008, **112**, 457–465.
138. M. G. Trainer, M. A. Tolbert, C. P. McKay, and O. B. Toon, *Icarus*, 2010, **206**, 707–715.
139. R. M. Mastrapa, S. A. Sandford, T. L. Roush, D. P. Cruikshank, and C. M. Dalle Ore, *Astrophys. J.*, 2009, **701**, 1347–1356.
140. G. A. Baratta and M. E. Palumbo, *J. Opt. Soc. Am. A.*, 1998, **15**, 3076–3085.
141. T. Henning, B. Begemann, H. Mutschke, and J. Dorschner, *Astron. Astrophys. Suppl. Ser.*, 1995, **112**, 143–149.
142. T. R. Steyer, *Ph.D. Thesis, Univ. of Arizona*, 1974.
143. P. Ordejón, E. Artacho, and J. M. Soler, *Phys. Rev. E*, 1996, **53**, R10441–R10444.
144. J. M. Soler, E. Artacho, J. D. Gale, A. García, J. Junquera, P. Ordejón, and D. Sánchez-Portal, *J. Phys. Condens. Matter*, 2002, **14**, 2745–2779.
145. K. M. Pontoppidan, A. C. A. Boogert, H. J. Fraser, E. F. van Dishoeck, G. A. Blake, F. Lahuis, K. I. Öberg, N. J. Evans II, and C. Salyk, *Astrophys. J.*, 2008, **678**, 1005–1031.
146. J. F. Bell III, W. M. Calvin, M. E. Ockert-Bell, D. Crisp, J. B. Pollack, and J. Spencer, *J. Geophys. Res.*, 1996, **101**, 9227–9237.
147. T. C. Preston and R. Signorell, *Acc. Chem. Res.*, 2012, **45**, 1501–1510.
148. L. B. d’Hendecourt and L. J. Allamandola, *Astron. Astrophys. Suppl. Ser.*, 1986, **64**, 453–467.
149. W. Hagen, A. G. G. M. Tielens, and J. M. Greenberg, *Astron. Astrophys. Suppl. Ser.*, 1983, **51**, 389–416.
150. M. H. Moore, R. F. Ferrante, R. L. Hudson, and J. N. Stone, *Icarus*, 2007, **190**, 260–273.
151. J. E. Bertie and J. P. Devlin, *J. Chem. Phys.*, 1984, **81**, 1559–1572.
152. J. E. Bertie and M. R. Shehata, *J. Chem. Phys.*, 1984, **81**, 27–30.
153. G. Sill, U. Fink, and J. R. Ferraro, *J. Chem. Phys.*, 1981, **74**, 997–1000.
154. W. Zheng, D. Jewitt, and R. I. Kaiser, *Astrophys. J. Suppl. Ser.*, 2009, **181**, 53–61.

155. R. F. Knacke, S. McCorkle, R. C. Puetter, E. F. Erickson, and W. Krättschmer, *Astrophys. J.*, 1982, **260**, 141–146.
156. R. D. Waldron and D. F. Hornig, *J. Am. Chem. Soc.*, 1953, **75**, 6079–6080.
157. T. Huston, I. C. Hisatsune, and J. Heicklen, *Can. J. Chem.*, 1983, **61**, 2077–2088.
158. J. E. Bertie and M. M. Morrison, *J. Chem. Phys.*, 1980, **73**, 4832–4837.
159. J. E. Bertie and M. M. Morrison, *J. Chem. Phys.*, 1981, **74**, 4361–4371.
160. J. E. Bertie and J. P. Devlin, *J. Chem. Phys.*, 1983, **78**, 6203–6208.
161. J. E. Bertie and M. R. Shehata, *J. Chem. Phys.*, 1985, **83**, 1449–1456.
162. C. Thornton, M. S. Khatkale, and J. P. Devlin, *J. Chem. Phys.*, 1981, **75**, 5609–5614.
163. N. Boudin, W. A. Schutte, and J. M. Greenberg, *Astron. Astrophys.*, 1998, **331**, 749–759.
164. C. Knez, M. H. Moore, R. F. Ferrante, and R. L. Hudson, *Astrophys. J.*, 2012, **748**, 95.
165. K. Consani and G. C. Pimentel, *J. Phys. Chem.*, 1987, **91**, 289–293.
166. M. Isenor, R. Escribano, T. C. Preston, and R. Signorell, *Icarus*, 2013, **223**, 591–601.
167. G. A. Yeo and T. A. Ford, *Can. J. Chem.*, 1991, **69**, 632–637.
168. S. K. Pope, M. G. Tomasko, M. S. Williams, M. L. Perry, L. R. Doose, and P. H. Smith, *Icarus*, 1992, **100**, 203–220.
169. A. Engdahl and B. Nelander, *Chem. Phys. Lett.*, 1983, **100**, 129–132.
170. J. S. Holt, D. Sadoskas, and C. J. Pursell, *J. Chem. Phys.*, 2004, **120**, 7153–7157.
171. F. P. Reding and D. F. Hornig, *J. Chem. Phys.*, 1951, **19**, 594–601.
172. J. P. Devlin, *J. Geophys. Res.*, 2001, **106**, 33333–33349.
173. W. J. Siemons and D. H. Templeton, *Acta Crystallogr.*, 1954, **7**, 194–198.
174. I. Olovsson and D. H. Templeton, *Acta Crystallogr.*, 1959, **12**, 827–832.
175. A.-P. Rollet and G. Vuillard, *C. R. Hebd. Seances Acad. Sci.*, 1956, **243**, 383–386.

176. The Cosmic Ice Laboratory - IR Spectra, <http://science.gsfc.nasa.gov/691/cosmicice/spectra.html>, (accessed June 23, 2014).
177. N. Fray and B. Schmitt, *Planet. Space Sci.*, 2009, **57**, 2053–2080.
178. D. A. Dows, *Spectrochim. Acta*, 1966, **22**, 1479–1481.
179. S. C. Silva and J. P. Devlin, *J. Phys. Chem.*, 1994, **98**, 10847–10852.
180. M. T. Kirchner, D. Bläser, and R. Boese, *Chem. Eur. J.*, 2010, **16**, 2131–2146.
181. J. E. Molloy and M. J. Padgett, *Contemp. Phys.*, 2002, **43**, 241–258.
182. D. McGloin and K. Dholakia, *Contemp. Phys.*, 2005, **46**, 15–28.
183. J. Durnin, J. J. Miceli Jr., and J. H. Eberly, *Phys. Rev. Lett.*, 1987, **58**, 1499–1501.
184. A. Stockham and J. G. Smith, *Proc. SPIE*, 2006, **6326**, 63261D.
185. J. Arlt and K. Dholakia, *Opt. Commun.*, 2000, **177**, 297–301.
186. A. E. Carruthers, S. A. Tatarkova, V. Garcés-Chávez, K. Volke-Sepulveda, S. Chavez-Cerda, and K. Dholakia, *Proc. SPIE*, 2003, **5121**, 68–76.
187. T. Čižmár, V. Garcés-Chávez, K. Dholakia, and P. Zemánek, *Proc. SPIE*, 2005, **5930**, 59300X.
188. T. Čižmár, V. Garcés-Chávez, K. Dholakia, and P. Zemánek, *Proc. SPIE*, 2004, **5514**, 643–651.
189. A. E. Carruthers, J. P. Reid, and A. J. Orr-Ewing, *Opt. Express*, 2010, **18**, 14238–14244.
190. I. Thanopoulos, D. Luckhaus, T. C. Preston, and R. Signorell, *J. Appl. Phys.*, 2014, **115**, 154304.
191. J. S. Walker, A. E. Carruthers, A. J. Orr-Ewing, and J. P. Reid, *J. Phys. Chem. Lett.*, 2013, **4**, 1748–1752.
192. B. J. Mason, J. S. Walker, J. P. Reid, and A. J. Orr-Ewing, *J. Phys. Chem. A*, 2014, **118**, 2083–2088.
193. S. A. Tatarkova, A. E. Carruthers, and K. Dholakia, *Phys. Rev. Lett.*, 2002, **89**, 283901.

194. V. Karásek, T. Čížmár, O. Brzobohatý, P. Zemánek, V. Garcés-Chávez, and K. Dholakia, *Phys. Rev. Lett.*, 2008, **101**, 143601.
195. E. J. Davis and A. K. Ray, *J. Colloid Interface Sci.*, 1980, **75**, 566–576.
196. E. J. Davis, *Langmuir*, 1985, **1**, 379–387.
197. B. Krämer, O. Hübner, H. Vortisch, L. Wöste, T. Leisner, M. Schwell, E. Rühl, and H. Baumgärtel, *J. Chem. Phys.*, 1999, **111**, 6521–6527.
198. K. Taji, M. Tachikawa, and K. Nagashima, *Appl. Phys. Lett.*, 2006, **88**, 141111.
199. P. Vainshtein and M. Shapiro, *Part. Sci. Technol.*, 2011, **29**, 450–465.
200. N. J. Mason, E. A. Drage, S. M. Webb, A. Dawes, R. McPheat, and G. Hayes, *Faraday Discuss.*, 2008, **137**, 367–376.
201. C. Mund and R. Zellner, *ChemPhysChem*, 2003, **4**, 630–638.
202. D. L. Bones, J. P. Reid, D. M. Lienhard, and U. K. Krieger, *Proc. Natl. Acad. Sci. U. S. A.*, 2012, **109**, 11613–11618.
203. H.-J. Tong, J. P. Reid, D. L. Bones, B. P. Luo, and U. K. Krieger, *Atmos. Chem. Phys.*, 2011, **11**, 4739–4754.
204. T. Koop, J. Bookhold, M. Shiraiwa, and U. Pöschl, *Phys. Chem. Chem. Phys.*, 2011, **13**, 19238–19255.
205. B. Zobrist, C. Marcolli, D. A. Pedernera, and T. Koop, *Atmos. Chem. Phys.*, 2008, **8**, 5221–5244.
206. B. Zobrist, V. Soonsin, B. P. Luo, U. K. Krieger, C. Marcolli, T. Peter, and T. Koop, *Phys. Chem. Chem. Phys.*, 2011, **13**, 3514–3526.
207. M. Shiraiwa, M. Ammann, T. Koop, and U. Pöschl, *Proc. Natl. Acad. Sci. U. S. A.*, 2011, **108**, 11003–11008.
208. A. Virtanen, J. Joutsensaari, T. Koop, J. Kannosto, P. Yli-Pirilä, J. Leskinen, J. M. Mäkelä, J. K. Holopainen, U. Pöschl, M. Kulmala, D. R. Worsnop, and A. Laaksonen, *Nature*, 2010, **467**, 824–827.

209. L. Renbaum-Wolff, J. W. Grayson, A. P. Bateman, M. Kuwata, M. Sellier, B. J. Murray, J. E. Shilling, S. T. Martin, and A. K. Bertram, *Proc. Natl. Acad. Sci. U. S. A.*, 2013, **110**, 8014–8019.
210. B. Graham, O. L. Mayol-Bracero, P. Guyon, G. C. Roberts, S. Decesari, M. C. Facchini, P. Artaxo, W. Maenhaut, P. Köll, and M. O. Andreae, *J. Geophys. Res.*, 2002, **107**, 8047.
211. A. Carvalho, C. Pio, and C. Santos, *Atmos. Environ.*, 2003, **37**, 1775–1783.
212. G. Wang, K. Kawamura, and M. Lee, *Atmos. Environ.*, 2009, **43**, 219–227.
213. K. E. Yttri, C. Dye, and G. Kiss, *Atmos. Chem. Phys.*, 2007, **7**, 4267–4279.
214. B. Graham, P. Guyon, P. E. Taylor, P. Artaxo, W. Maenhaut, M. M. Glovsky, R. C. Flagan, and M. O. Andreae, *J. Geophys. Res.*, 2003, **108**, 4766.
215. S. Decesari, S. Fuzzi, M. C. Facchini, M. Mircea, L. Emblico, F. Cavalli, W. Maenhaut, X. Chi, G. Schkolnik, A. Falkovich, Y. Rudich, M. Claeys, V. Pashynska, G. Vas, I. Kourtchev, R. Vermeylen, A. Hoffer, M. O. Andreae, E. Tagliavini, F. Moretti, and P. Artaxo, *Atmos. Chem. Phys.*, 2006, **6**, 375–402.
216. A. Aksan and M. Toner, *Langmuir*, 2004, **20**, 5521–5529.
217. W. M. Haynes, Ed., in *CRC Handbook of Chemistry and Physics, 95th Edition, (Internet Version 2015)*, CRC Press/Taylor and Francis, Boca Raton, FL.
218. X. Cao, B. C. Hancock, N. Leyva, J. Becker, W. Yu, and V. M. Masterson, *Int. J. Pharm.*, 2009, **368**, 16–23.
219. C. Peng, A. H. L. Chow, and C. K. Chan, *Aerosol Sci. Technol.*, 2001, **35**, 753–758.
220. A. Correa, J. F. Comesaña, and A. M. Sereno, *Int. J. Food Sci. Technol.*, 1994, **29**, 331–338.
221. C. R. Lerici, M. Piva, and M. Dalla Rosa, *J. Food Sci.*, 1983, **48**, 1667–1669.
222. A. Gharsallaoui, B. Rogé, J. Génotelle, and M. Mathlouthi, *Food Chem.*, 2008, **106**, 1443–1453.
223. D. M. Lienhard, D. L. Bones, A. Zuend, U. K. Krieger, J. P. Reid, and T. Peter, *J. Phys. Chem. A*, 2012, **116**, 9954–9968.

224. A. Simperler, A. Kornherr, R. Chopra, P. A. Bonnet, W. Jones, W. D. S. Motherwell, and G. Zifferer, *J. Phys. Chem. B*, 2006, **110**, 19678–19684.
225. G. Hargreaves, N.-O. A. Kwamena, Y. H. Zhang, J. R. Butler, S. Rushworth, S. L. Clegg, and J. P. Reid, *J. Phys. Chem. A*, 2010, **114**, 1806–1815.
226. S. L. Clegg, P. Brimblecombe, Z. Liang, and C. K. Chan, *Aerosol Sci. Technol.*, 1997, **27**, 345–366.
227. S. L. Clegg and A. S. Wexler, *J. Phys. Chem. A*, 2011, **115**, 3393–3460.
228. D. J. Burnett, F. Thielmann, and J. Booth, *Int. J. Pharm.*, 2004, **287**, 123–133.
229. V. Truong, B. R. Bhandari, T. Howes, and B. Adhikari, *Int. J. Food Sci. Technol.*, 2004, **39**, 569–578.
230. K. Anders, N. Roth, and A. Frohn, *J. Geophys. Res.*, 1996, **101**, 19223–19229.
231. N. Roth and A. Frohn, *Atmos. Environ.*, 1998, **32**, 3139–3143.
232. C. Mund and R. Zellner, *ChemPhysChem*, 2003, **4**, 638–645.
233. H. Suzuki, Y. Matsuzaki, A. Muraoka, and M. Tachikawa, *J. Chem. Phys.*, 2012, **136**, 234508.
234. S. Ishizaka, T. Wada, and N. Kitamura, *Chem. Phys. Lett.*, 2011, **506**, 117–121.
235. K. Diehl, M. Ettner-Mahl, A. Hannemann, and S. K. Mitra, *Atmos. Res.*, 2009, **94**, 356–361.
236. M. Ettner, S. K. Mitra, and S. Borrmann, *Atmos. Chem. Phys.*, 2004, **4**, 1925–1932.
237. K. L. Carleton, D. M. Sonnenfroh, W. T. Rawlins, B. E. Wyslouzil, and S. Arnold, *J. Geophys. Res.*, 1997, **102**, 6025–6033.
238. G. S. Parks and G. E. Moore, *J. Chem. Phys.*, 1949, **17**, 1151–1153.
239. C. Wolfarth, in *Springer Materials - The Landolt-Börnstein Database*, ed. M. D. Lechner, Springer-Verlag Berlin, 2008.
240. F. A. Jenkins and H. E. White, *Fundamentals of Optics*, McGraw-Hill, New York, 3rd edn., 1957.

241. I. Weidinger, J. Klein, P. Stöckel, H. Baumgärtel, and T. Leisner, *J. Phys. Chem. B*, 2003, **107**, 3636–3643.
242. P. Stöckel, I. M. Weidinger, H. Baumgärtel, and T. Leisner, *J. Phys. Chem. A*, 2005, **109**, 2540–2546.
243. D. Duft and T. Leisner, *Atmos. Chem. Phys.*, 2004, **4**, 1997–2000.
244. P. Stöckel, H. Vortisch, T. Leisner, and H. Baumgärtel, *J. Mol. Liq.*, 2002, **96-97**, 153–175.
245. C. Mund and R. Zellner, *J. Mol. Struct.*, 2003, **661-662**, 491–500.
246. A. Müller and K. Lonsdale, *Acta Crystallogr.*, 1948, **1**, 129–131.
247. E. B. Sirota and A. B. Herhold, *Science*, 1999, **283**, 529–532.
248. X.-Y. Liu and P. Bennema, *J. Cryst. Growth*, 1994, **135**, 209–223.
249. S. C. Nyberg, F. M. Pickard, and N. Norman, *Acta Crystallogr.*, 1976, **B32**, 2289–2293.
250. N. J. Bacon and B. D. Swanson, *J. Atmos. Sci.*, 2000, **57**, 2094–2104.
251. H. Kanno, R. J. Speedy, and C. A. Angell, *Science*, 1975, **189**, 880–881.
252. O. Mishima and H. E. Stanley, *Nature*, 1998, **396**, 329–335.
253. A. A. Zardini, U. K. Krieger, and C. Marcolli, *Opt. Express*, 2006, **14**, 6951–6962.
254. I. N. Tang and H. R. Munkelwitz, *J. Colloid Interface Sci.*, 1991, **141**, 109–118.
255. C. Cai, D. J. Stewart, T. C. Preston, J. S. Walker, Y.-H. Zhang, and J. P. Reid, *Phys. Chem. Chem. Phys.*, 2014, **16**, 3162–3172.
256. E. J. Davis and A. K. Ray, *J. Aerosol Sci.*, 1978, **9**, 411–422.
257. J. Gieseler, B. Deutsch, R. Quidant, and L. Novotny, *Phys. Rev. Lett.*, 2012, **109**, 103603.